MECHANISMS OF ORGANIC-INORGANIC INTERACTIONS IN SOILS AND AQUEOUS ENVIRONMENTS ELUCIDATED USING CALORIMETRIC TECHNIQUES

A Dissertation

by

OMAR R. HARVEY

Submitted to the Office of Graduate Studies of
Texas A&M University
in partial fulfillment of the requirements for the degree of

DOCTOR OF PHILOSOPHY

May 2010

Major Subject: Water Management and Hydrological Science

MECHANISMS OF ORGANIC-INORGANIC INTERACTIONS IN SOILS AND AQUEOUS ENVIRONMENTS ELUCIDATED USING CALORIMETRIC TECHNIQUES

A Dissertation

by

OMAR R. HARVEY

Submitted to the Office of Graduate Studies of
Texas A&M University
in partial fulfillment of the requirements for the degree of

DOCTOR OF PHILOSOPHY

Approved by:

Chair of Committee,	Bruce E. Herbert
Committee Members,	Bill Batchelor
	Youjun Deng
	Ronald Kaiser
	Patrick Louchouarn
Intercollegiate Faculty Chair,	Ronald Kaiser

May 2010

Major Subject: Water Management and Hydrological Science

ABSTRACT

Mechanisms of Organic-Inorganic Interactions in Soils and Aqueous Environments Elucidated Using Calorimetric Techniques.

(May 2010)

Omar R. Harvey, B.S. University of the West Indies;

M.S., University of Florida

Chair of Advisory Committee: Dr. Bruce E. Herbert

Organic matter is ubiquitous in the environment and exists in many different forms. Reactions involving organic matter are diverse and many have significant economic and environmental implications. In this research, calorimetric techniques were used to study organic- inorganic reactions in two different systems. The primary objectives were to elucidate potential mechanism(s) by which: (i) natural organic matter (NOM) influences strength development in lime-stabilized soils, and; (ii) plant-derived biochars reacts with cations in aqueous environments.

Natural organic matter influenced strength development in lime-stabilized soils through the direct inhibition of the formation of pozzolanic reaction products. The degree of inhibition was dependent mainly on the type of pozzolanic reaction product, and the amount and source of organic matter. The formation of the pozzolanic reaction product, calcium silicate hydrate II (CSH2) was less affected by NOM, than was the formation of CSH1. For a given pozzolanic product, the inhibition increased with NOM

content. The effect of organic matter source followed the order fulvic acid> humic acid> lignite. Formation of CSH pozzolanic reaction products decreased by 50-100%, 20-80% and 20-40% in the presence of ≥2% fulvic acid, humic acid and lignite, respectively.

Cation interactions with plant-derived biochars were complex and depended both on the nature of the cation and biochar surface properties. Reactions involving the alkali cation, K^+; occurred via electrostatic ion exchange, on deprotonated functional groups located on the biochar surface and; were exothermic with molar heats of reaction (ΔH_{ads}) between -3 and -8 kJ mol^{-1}. In contrast, reactions involving the transition metal cation, Cd^{2+} were endothermic with ΔH_{ads} between +10 and +30 kJ mol^{-1}. Reaction mechanism(s) for Cd^{2+} varied from ion exchange/surface complexation in biochars formed at <350 ^oC, to an ion exchange/surface complexation/diffusion-controlled mechanism in biochars formed at ≥350 ^oC. For a given cation, differences in sorption characteristics were attributable to temperature-dependent or plant species dependent variations in the properties of the biochars.

DEDICATION

To my family

ACKNOWLEDGEMENTS

I would like to thank my advisor, Dr. Herbert, and my committee members, Drs. Bill Batchelor, Ronald Kaiser, Patrick Louchouarn, and Youjun Deng, for their assistance and support throughout the course of this research.

Thanks also go to Dr. Dean Rhue at the University of Florida for his assistance and support in my flow adsorption micro-calorimetry experiments. I would also like to thank my friends and colleagues, as well as the Water Program faculty and staff, for making my time at Texas A&M University a great experience. I am also grateful to Dr. Pat Harris, and the Texas Transportation Institute and Texas Department of Transportation for providing partial funding for my research.

Most importantly, thanks to my family for their encouragement and support, and to my (may I say) lovely, lovely, (and again) lovely wife (Keisha Marie Rose-Harvey) for her patience, and for loving me through this research, even when I was unloveable.

TABLE OF CONTENTS

Page

ABSTRACT……. iii

DEDICATION v

ACKNOWLEDGEMENTS vi

TABLE OF CONTENTS vii

LIST OF FIGURES x

LIST OF TABLES xiii

CHAPTER

I INTRODUCTION: ORGANIC MATTER INFLUENCES THE DYNAMICS AND FUNCTION OF NATURAL SYSTEMS 1

1.1. Organic matter in the environment 1
1.2. Organic matter in the environment: The case of soil stabilization 5
1.3. Organic matter in the environment: The case of black carbon and plant-derived biochars 9
1.3.1. Occurrence and significance 9
1.3.2. Structure and properties 9
1.3.3. Sorption characteristics 14

II SPECTROPHOTOMETRIC METHOD FOR ESTIMATING SOIL ORGANIC CARBON 18

2.1. Introduction 18
2.2. Materials and methods 21
2.2.1. Soils and humic material 21
2.2.2. Method development 22
2.2.3. Method evaluation 24

CHAPTER Page

2.3. Results and discussion....25
2.3.1. Soil organic carbon extraction and analysis....25
2.3.2. Method performance....34
2.4. Summary and conclusions....38

III NATURAL ORGANIC MATTER AND THE FORMATION OF CALCIUM SILICATE HYDRATE IN LIME-STABILIZED SMECTITES: A THERMAL ANALYSIS STUDY....40

3.1. Introduction....40
3.2. Materials and methods....42
3.2.1. Soils, lime and natural organic matter....42
3.2.2. Paste experiments....43
3.2.3. Core experiments....44
3.3. Results and discussion....45
3.3.1. Lime-soil reactions in organic matter-free conditions....45
3.3.2. Lime-soil reactions in the presence of natural organic matter....50
3.3.3. Effect of natural organic matter source on calcium silicate hydrate formation....56
3.4. Summary and conclusions....59

IV TEMPERATURE-DEPENDENT TRANSFORMATIONS IN PLANT-DERIVED BIOCHARS: IMPLICATIONS FOR CATION EXCHANGE CHARACTERISTICS AND CADMIUM SORPTION AS DETERMINED BY FLOW ADSORPTION CALORIMETRY. 61

4.1. Introduction....61
4.2. Material and methods....64
4.2.1. Plant-derived biochars and biochar preparation....64
4.2.2. Chemical composition of biochars....65
4.2.3. Flow adsorption micro-calorimetry experiments....66
4.2.3.1. The flow adsorption micro-calorimeter....66
4.2.3.2. Cation exchange and cadmium sorption characteristics on plant-derived biochars....67
4.3. Results and discussion....71
4.3.1. Temperature-dependent transformations in plant-derived biochars....71
4.3.1.1. Transformations in biochars inferred from elemental analysis....71

CHAPTER Page

4.3.1.2. Transformations inferred from infrared spectroscopy 76
4.3.2. Thermal transformations influences surface charge characteristics of plant-derived biochars 86
4.3.3. K^+/Na^+ exchange on plant derived biochars as determined by flow adsorption micro-calorimetry. 98
4.3.4. Cadmium (Cd^{2+}) sorption characteristics on plant derived biochars as determined by flow adsorption micro-calorimetry. 104
4.4. Summary and conclusions....112

V SUMMARY 115

REFERENCES....117

APPENDIX 1 135

APPENDIX 2 136

APPENDIX 3 137

APPENDIX 4 140

APPENDIX 5 141

VITA…….. 147

LIST OF FIGURES

Page

Fig. 1. Major land resource areas from which soil samples were obtained. 23

Fig. 2. Particle size distribution of soils used in UV-Vis method calibration and validation, *n = 146*. 28

Fig. 3. UV-Vis spectra of soil extracts and reference humic acid. 29

Fig. 4. Correlation between extract absorbance at 300 nm (A_{300nm}) and dry combustion determined soil organic carbon (*SOC*) for selected calcareous (*n = 13*) and non-calcareous (*n = 14*) soils using 0.25 mol L^{-1} NaOH solution as an extractant. 31

Fig. 5. Relationship between soil extract absorbance at 300 nm (A_{300nm}) and soil organic carbon (*SOC*) for calibration samples (*n = 73*) using the proposed method. 35

Fig. 6. Comparison of SOC for validation samples (*n = 73*) as measured by dry combustion and determined sphectrophotometrically using the proposed method. 36

Fig. 7. (A and B) Differential scanning calorimertry and (C) derivative thermogravimetry thermograms of (i) Panther Creek montmorillonite, (ii) Gonzalez bentonite, and (iii) hydrated lime starting materials. 46

Fig. 8. (A, B, D and E) Differential scanning calorimertry and (C and F) derivative thermogravimetry thermograms of 10 day incubated (A-C) Panther Creek montmorillonite and (D-F) Gonzales bentonite pastes containing different amounts of hydrated lime. 47

Fig. 9. X-ray diffractograms of 10 day incubated 1:1 soil: water (A) Gonzales bentonite, and (B) Panther Creek montmorillonite pastes containing 0-20% hydrated lime. 50

Fig. 10. Thermograms of (A-C) Gonzalez bentonite and (D-F) Panther Creek montmorillonite core samples containing six percent hydrated lime plus (i) 0, (ii) 0.5, (iii) 2 or (iv) 5% commercial humic acid. 51

Fig. 11. Unconfined compressive of lime-stabilized cores as a function of humic acid added. Samples were incubated at 100% humidity and 23 ^{o}C for 3 days, 7 days or 28 days. 52

Page

Fig. 12. Relationship between unconfined compressive strength of lime stabilized cores and integral heat of CSH re-crystallization. 56

Fig. 13. Intensity of DSC peaks attributable to CSH formation in GB (8% lime) and PCM (12% lime) pastes containing (i) 0, (ii) 0.5, (iii) 2 or (iv) 5% natural organic matter as commercial humic acid (cHA), soil fulvic acid (sFA), soil humic acid (sHA) and lignite (Lig). 58

Fig. 14. Change in calcium silicate hydrate formation with natural organic matter content in GB and PCM pastes. 59

Fig. 15. Schematic of dual-mode variable-gain flow adsorption micro-calorimeter. 68

Fig. 16. H/C (open symbols) and O/C (closed symbols) ratio for loblolly pine (PI), honey mesquite (HM), and cord grass (CG) biochars. 74

Fig. 17. Weight loss during formation of loblolly pine (PI), honey mesquite (HM) and cord grass (CG) biochars. 76

Fig. 18. Infrared spectroscopy analysis in the OH-stretch range for plant-derived formed at temperatures between 200 and 650 ^{o}C 79

Fig. 19. Infrared spectroscopy analysis in the CH-stretch range for plant-derived formed at temperatures between 200 and 650 ^{o}C 82

Fig. 20. Infrared spectroscopy analysis in the finger-print region for plant-derived formed at temperatures between 200 and 650 ^{o}C 84

Fig. 21. Dissociation characteristics of acidic functional groups on the surface of loblolly pine, honey mesquite and cord grass plant-derived biochars. 96

Fig. 22. Typical heat signals for ion exchange reaction between K^+ and Na^+ on plant-derived biochars. 99

Fig.23. Variation in (A) energy evolved, (B) K^+ adsorbed and (C) their relationship as a result of K^+/Na^+ exchange on loblolly pine (PI), honey mesquite (HM) and cord grass (CG) biochars at different solution pH. 103

Fig. 24. Calorimetric heat signals for Cd^{2+} sorption onto selected Na^+-saturated loblolly pine (PI), honey mesquite (HM) and cord grass (CG) biochars. 106

Page

Fig. 25. Relationship between the heat of adsorption (E_{Total}) and amount of Cd^{2+} adsorbed on plant-derived biochars. 108

Fig. 26. Variation in Cd^{2+} saturation of cation exchange sites with surface charge density (σ^-) on plant-derived biochars.....112

LIST OF TABLES

Page

Table 1. Taxonomic classification of soil used from each major land resource area, MLRA. 27

Table 2. Summary of selected chemical properties of soil samples used, *n = 146.* 28

Table 3. Analysis of covariance of the effect of soil organic C (*SOC*), major land resource area (MLRA), soil texture, calcareous or non-calcareous on soil extract absorbance at 300 nm. 33

Table 4. Variation in method calibration and validation regression parameters when data (*n = 146*) was split randomly into calibration and validation sets of different sizes. 38

Table 5. Biomacromolecule and elemental composition of plant-derived biochars. 72

Table 6. Dominant mechanisms active in plant-derived biochars formed at temperatures up to 650 ^{o}C. Mechanisms were inferred from elemental and infrared spectroscopy data. 86

Table 7. Surface properties of plant-derived biochars used in flow adsorption micro-calorimetry experiments. 87

Table 8. Quantity of Cd^{2+} and K^{+} adsorbed and their energetics of sorption onto loblolly pine (PI), honey mesquite (HM) and cord grass (CG) biochars at pH5 111

CHAPTER I

INTRODUCTION: ORGANIC MATTER INFLUENCES THE DYNAMICS AND FUNCTION OF NATURAL SYSTEMS

1.1. Organic matter in the environment

Soils and aquatic systems are among the most perturbed of natural systems [1] . For centuries, rivers and wetlands have been modified for water supply, recreational, agricultural and transportation purposes [1, 2]. Similarly, soils have been modified for a wide variety of agricultural and engineering purposes including; soil fertility and drainage [3, 4], road and building construction [5, 6], land conservation [7-9] and hazardous waste containment [10, 11]. Modification of natural systems can have significant effects on system dynamics and functions. For example, in addition to changing the hydrology and physical characteristics of the system, damming of rivers to form lakes results in modifications to the biogeochemical structure of that system [2]. Such modifications include; interruption of the flow of organic carbon, changes in the nutrient balance, and alterations of oxygen and thermal conditions and can lead to depletion in both water quality [12-14] and ecosystem diversity [15-17].

Many other examples of changes in the dynamics and function of soil and aquatic systems due to physical or chemical modification of system property(s) can be described. Paramount among them, are system modifications involving organic matter. Organic matter is any organic material derived from plant, animal or microbial biomass [18, 19]. Organic matter is ubiquitous, and physically and chemically diverse.

This dissertation follows the style of the Journal of Colloid and Interface Science.

Classification schemes for organic matter vary depending on factors such as: occurrence (eg. atmospheric, terrestrial or aquatic); source (eg. geologic or anthropogenic); and physical characteristics (eg. particulate or dissolved) [19].
In this introduction classification of organic matter based on occurrence will be used. For each organic matter type the nature, potential effects on system dynamics, and function will be discussed.

Atmospheric organic matter exists as primary and secondary aerosols [20]. Primary organic aerosols (POAs) are emitted directly in the atmosphere primarily from fossil fuel combustion and biomass burning, but may come from other sources such as: bacteria, viruses and spores; roads, tire and brake abrasions; and fine soil particles [20]. Secondary organic aerosols (SOAs) are formed through condensation of VOCs in the atmosphere [20]. Estimates of atmospheric organic matter production are very variable and range between 2- 270 Tg y^{-1} [21-25]. Chemically, atmospheric organic matter is comprised of lipids, PAHs, soot, humic and fulvic acids [26]. The effects of atmospheric organic matter on visibility and health effects have been widely discussed [26] . Their effect on cloud nucleation has also been studied [27-29]. More recently, there has been increase interest in the effect of atmospheric organic matter on climate change. Since, organic aerosols have the ability to scatter or absorbed light they can modify the radiative balance of the atmosphere. The effect of organic aerosols on climate is twofold. On one hand, organic aerosols such as soot-black carbon adsorb solar radiation resulting in a warming effect. However, other organic aerosols have a cooling effect [30]. Ramananthan and Carmichael [31] suggested that emissions of black carbon are the

second strongest contributor to current global warming, after carbon dioxide emissions; and in Himalayas may be just as important as carbon dioxide in the melting of snowpacks and glaciers.

It has been estimated that about two-thirds (1500 Gt) of the global terrestrial carbon exists as soil organic matter [32]. Primary inputs of organic matter to soils are dead plant biomass and root deposits. Although the annual inputs of organic matter to soils are on the order of 75 Gt y^{-1}, the net balance is around zero because an equivalent amount is lost as CO_2 [33]. Chemically, soil organic matter is comprised of a complex mixture of polysaccharides, lipids, proteins, microbial biomass and humic matter at varying stages of decomposition [18]. In fire impacted areas, black carbon is a major constituent of soil organic matter and can account for up to 80% of soil organic carbon [34, 35]. Components of soil organic matter can be divided into an active "labile" pool and a stable pool [18]. The active pool consists of all non-humic components (except black carbon) and is susceptible to decomposition. Mean residence time of the active pool is between 5 and100 years compared to >1000 years for the stable pool. The stable pool consists of humic matter and black carbon.

Humic matter is a complex mixture of fulvic acids (FA), humic acids (HA) and humin [18, 19]. Fulvic acids are soluble under acidic, neutral or basic conditions; humic acids under alkali conditions only; while humin is insoluble. Humin is not widely studied because of its chemical inertness. In contrast, fulvic and humic acids are very chemically active differing mainly in the proportion of carbon and oxygen functional groups. In general, HA have a higher aromaticity, lower oxygen content and lower total

acidity than FA [18, 19]. The FA/HA ratio in soils is dependent on soil type and source. Tan [19] found that mollisols are dominated by humic acids (low FA/HA). However, another soil with similar organic content, but located in the humid tropics or arctic regions, was dominated by fulvic acid with FA/HA ratio as high as 4. Humic matter is known to modify the physical and chemical properties of soils. The typical dark color of many soils is due to humic matter. In addition to improving the water holding, buffering and cation exchange capacities, humic matter also enhances soil aggregation, metal chelation and control the leaching of nutrients and contaminants in soils [18]. Stevenson [18] suggested that humic matter can hold up to 20 times its body weight in water and increase cation exchange capacity of a soil by as much as 70%. Such modifications have significant implications for the fate and transport of nutrients and contaminants in soils. Black carbon, as a part of soil organic matter would affect the same properties of a soil as humic matter, but to lesser extent.

Aquatic organic matter refers to that found in streams, lakes, oceans and their sediments [19]. Aquatic organic matter has the same constituents as soil organic matter but is distributed in an aqueous environment and is collectively referred to as dissolved organic matter (DOM). Dissolved organic matter maybe *allocthonous* (leached from soils or deposited from the atmosphere and transported to rivers, lakes or oceans) or *autochthonous* (derived from indigenous aquatic organisms). Both allocthonous and autochthonous DOM has a hydrophilic fraction (dissolved and dominated by fulvic acids) and hydrophobic fraction (suspended, dominated by humic acids). In either case, DOM affects water quality and the biogeochemical cycles in water bodies. For example,

the dark brown colored water seen in many rivers is due to DOM. In cases where the water is used for potable water, pre-treatment to remove DOM is important since reaction with chlorine (from water treatment) produces harmful disinfectant products such as trihalomethanes and chloramines [36, 37]. Dissolved organic matter is also a major factor in the development of anoxic zones in lakes which can have significant implications for nutrient and ecosystem dynamics [2, 38].

It is clear that organic matter influences the dynamics and function of a number of systems. In this research organic matter interactions in two systems were studied. The focus of the research was on understanding: (i) Reactions of soil organic matter in lime-treated soils and implications for long term strength development; (ii) Thermal transformations in plant-derived biochars and implications for the geochemical cycling of metals in soils and sediments.

1.2. Organic matter in the environment: The case of soil stabilization

In the US, the addition of lime as a stabilizing agent in modern construction can be traced back to the early 1900's, when hydrated lime was used to stabilize short stretches of highway [39]. Since then the use of lime as a stabilizer in construction has expanded to include railroads and airport construction, stabilization of slopes, backfill for bridge abutments and retaining walls, canal lining and construction on marine deposits [39, 40].

Reactions of lime with soil can be classified as: (i) soil modification, and (ii) soil stabilization reactions [41]. Soil modification reactions are transient processes associated with changes in clay hydration and cation exchange characteristics as a result of lime

additions to a soil. When lime is added to soils cation exchange occurs between the dissolved Ca^{2+} from the lime, and cations on the negatively charged surfaces of soil clays. For expansive soils, cation exchange reactions involving Ca^{2+} results in the shrinking of the electrical double layer (hydration layer around clay particles) leading subsequently to increase flocculation. The net effect is a change in soil texture resulting in reduced plasticity and increased workability [39, 41]. Since cation exchange is a reversible process the permanency of soil modification reactions with lime are questionable [39].

In contrast to soil modification, soil stabilization is permanent and involves the formation of new phases. The mechanism of stabilizer-soil reaction during cement- or lime-stabilization have been well understood for almost 50 years [42]. Eades and Grim [42] first suggested that the formation of new pozzolanic reaction products, responsible for strength development in lime-stabilized soils, occurs via a multi-step process. In the first step, cation exchange sites on the soil are saturated by Ca^{2+}. The amount of lime required to saturate the cation exchange sites will depend on the cation exchange capacity of the soil, which in turn is often a function of clay content. A lime application rate of 1% by weight for each 10% of clay in the soil is considered to be a good first approximation [43]. Since clay content rarely exceeds 80% in soils, an upper limit of 8% lime is common [39]. The second step in lime stabilization is the dissolution of silicon and aluminum from alumino-silicate and silicate minerals such as clays, quarts and microcrystalline opal. For maximum dissolution of these minerals a pH of around 12.4 is required. Such pH is usually achieved during hydration of lime. The final step in

stabilization, is the precipitation/cementation of pozzolanic (cementitious) reaction products. The most common classes of pozzolanic reaction products formed in lime stabilized soils are calcium aluminate hydrates (CAHs) and calcium silicate hydrates (CSH). Pozzolanic reaction products act to cement soil particles resulting in increase strength development and reduced shrink-swell characteristics. Pozzolanic reactions can continue for years. The degree of stabilization will depend on quantity and type of pozzolanic reaction product, which in turn is dependent on the clay content and mineralogy, lime content, and curing conditions such as time and temperature. Other factors such has organic matter is also important and can have significant effects on soil stabilization.

Work by Clare and Sherwood [44, 45] suggests that at least since the early 1950's some negative impact of organic matter on the stabilization of soils were apparent. They found that in the presence of some organic compounds, strength development in cement-stabilized sand mixtures were dractically reduced. Clare and Sherwood [44] classified different organic compounds as "active" or "inactive" depending on the ability of the compound to retard strength development in cement-stabilized sands. Compounds containing hydroxyl and carboxylic groups were found to be particularly "active" in retarding strength development. Based on this finding Clare and Sherwood [45] concluded that retardation of strength development was due to adsorption of Ca^{2+} ions from cement to hydroxyls and carboxylic groups. As additional evidence they pointed to fact that no adverse effects of organic matter on strength development wa observed in a soil developed on a calcareous rock.

More recently, failure in roadways and lower strength gains in stabilized soils have also been attributed to the presence of organic matter [44-48]. Despite the reported negative impacts of organic matter on soil stabilization, no clear mechanism(s) or data supporting a proposed mechanism have been presented. For example, Hampton and Edil [47] based on work done with cement-stabilized soils, suggested that organic matter inhibited cement stabilization of soils via complexation of Ca^{2+}. However, no data was presented to support such mechanisms and they later concluded that research is needed on the fundamental chemical reactions contributing to changes in the geotechnical properties of stabilized organic soils. A similar explanation to that of Hampton and Edil [47] was used by Chen et al. [46] to explain failures on several road constructions in Texas. The addition of extra stabilizer, to soils having >1% organic carbon was suggested as a possible solution. While this may seem plausible, no evidence has been provided to suggest that inhibition of pozzolanic activity by organic matter was due to cation complexation.

Given the complexity of natural organic matter and soils in general, a number of other mechanisms are possible. From the mechanism of lime stabilization described by Eades and Grim [42], the retardation effects of NOM on the stabilization could potentially occur at the ion exchange step, the dissolution step or the precipitation step. Based on the nature of organic matter potential mechanisms could include; (i) the buffering of the soil pH (such that dissolution of soil minerals needed to form pozzolanic reaction product is inhibited), (ii) poisoning of nucleation site (thereby preventing precipitation of new reaction products), and (iii) physical coating of soil particles (thereby preventing cementation of soil particle).

1.3. Organic matter in the environment: The case of black carbon and plant-derived biochars

1.3.1. Occurrence and significance

Biochars are carbon-rich solid residues formed from incomplete biomass combustion; and is commonly classified among a continuum of pyrogenic organic materials collectively referred to as "black carbon". Black carbon is ubiquitous in the environment and has important geochemical roles in global carbon cycling as well as many biogeochemical and environmental processes [49-55]. Estimates of global annual production for black carbon (BC) are on the order of 50- 270 Tg y^{-1}[56] and is commonly found in soils, sediments and the atmosphere, where it may constitute as much as 80% of the organic carbon in these systems [35, 57-60]. Many studies [60-65] point to the recalcitrant nature of BC (mean residence time > 1000 y [60, 66]) as evidence for it being a potentially significant part of the slow-cycling carbon pool in soils and sediments. Black carbon is an effective sorbent for organic compounds, and can influence the environmental fate and transport of many organic contaminants [51-55, 67-69]. It has also been shown that BC can influence the nutrient and microbial dynamics in soils [50, 65, 70-75].

1.3.2. Structure and properties

Black carbon is commonly described using the combustion continuum model [76]. In this model, BC is viewed as a continuum of combustion products, ranging from slightly charred, degradable biomass to highly condensed, refractory soot [77]. The general consensus among researchers is that the BC continuum comprises of two major

categories, char/charcoal and soot/graphite [49]. Biochars belong to the char/charcoal-BC category of continuum and can be produced from a number of different biomass feedstocks [50, 73, 74, 78-83].

Components of the BC continuum all have high carbon content, and are dominated by aromatic structures. Differentiation of components is largely operational, based on factors such as temperature of formation, particle size, residual plant structure and reactivity to chemical oxidation [77, 84]. For example, compared to soot/graphitic-BC, char/charcoal-BC are formed at lower temperatures, have larger particle size, retains enough physical and chemical properties to identify its biomass source, and is more susceptible to oxidation [77].

Early models of the chemical structure of BC suggested that components comprised of highly refractory cross-linked graphite-like sheets, which increase in size as the extent of thermal alteration increases [62, 66]. Recent studies however suggest that, for plant-derived biochars formed at temperatures typical of natural vegetation fires (<450 ^{o}C; [85, 86]), models claiming a graphite-like material - composed mainly of highly condensed polyaromatic clusters - may be oversimplified [87-89]. Knicker et al. [87] pointed to several facts that contradicts the existence of large polyaromatic networks in plant-derived biochars, likely to be formed at temperatures comparable to natural fires; (i) H/C atomic ratios for plant-derived biochar is typically >0.4, suggesting that on average every second to third carbon is connected to a proton; (ii) C/O atomic ratios in plant-derived biochar averages around 3, indicating the presence of significant amounts of oxygen [90-92]; and (iii) plant-derived biochars obtained from different plant

sources exhibit highly variable C/N atomic ratios (630 – 7) indicating variable amounts of N incorporated into the structure of the char. Based on these findings Knicker [87] suggested that in contrast to soot-BC, the aromatic skeleton of char-BC (such plant-derived biochars) had very few graphitic domains and proposed that rather than comprising of highly condensed aromatic structures, plant-derived biochar was a heterogeneous mixture of thermally altered biomacromolecules with N, O and likely S substitution as common features. Using solid-state 13C and 1H NMR spectroscopy, Knicker et al. [88] estimated that on average, the size of aromatic clusters in these biochars was less than 6.

The degree to which the original plant material is altered and the properties of the biochar formed during pyrolysis is dependent on combustion conditions (eg. temperature, combustion duration and oxygen supply) and the chemistry of the original plant tissues. As combustion temperature increases transformation of plant tissues occur via different mechanisms, thereby resulting in biochars with different properties. Kuo et al. [49] suggested that at pyrolysis temperatures $\leq$250 ^{o}C, the dominant mechanism occurring during char formation is dehydration, while at temperatures $\geq$300 ^{o}C aromatization is the dominant mechanism; with highly condensed aromatic materials forming at temperatures > 650 ^{o}C. As is commonly evidenced by a decrease in O/C and H/C ratios, biochars shows increasing hydrophobicity with increasing combustion temperature, as a result loss of polar oxygenated and protonated functional groups accompanied by a concomitant increase in carbonization. For biochars derived from nitrogen-containing plant material, N content and subsequently N/C ratio has been

shown to increase with increasing temperature [49, 81, 88, 93]. The specific surface area and porosity of plant-derived biochars have also been shown to increase with increasing combustion temperature and have been attributed to increases in microporosity and pore connectivity [93, 94]. Combustion duration appears to have a similar effect on biochar properties as combustion temperature. Sun and Zhou [95] found that for biochars formed by heating pine wood at 400 ^{o}C for different durations; aromaticity, specific surface area and nitrogen content increased with combustion duration. On the other hand hydrogen and oxygen content (and consequently H/C and O/C ratios) decrease with increasing combustion duration, consistent with an increase in the hydrophobicity of the biochar.

Oxygenated functionalities such as –OH, -COOH, -O-, =O, -CHO are common features of biochars. In addition to being affected by combustion temperature and starting material, the distribution of oxygenated functionality in biochars is also affected by oxygen supply. Zhu et al. [96] using FTIR spectroscopy, found that while peaks attributable to –OH, C=O and C-O were clearly observable in biochars produce in air, they were of much lower intensity in biochars heated in nitrogen and were absent in chars heated in hydrogen. These results indicated that the number of oxygenated functionalities likely to be present on the surfaces of the biochars decrease with lower oxygen supply, consistent with what have been reported for other naturally occurring BC [97] and activated carbon [98].

Research on biochars produced from different plant species and biomacromolecules show that starting material chemistry can have significant influence on the physical and chemical properties of plant-derived biochars. Wang and Xing [93]

found that biochars derived from chitin contained up to 15% nitrogen, while those derived from cellulose contained no nitrogen. Additionally they reported that chitin-derived char generally had more polar functionality, larger surface areas, and smaller average pore sizes than cellulose-derived biochars. Knicker et al. [88] also found significant variability in lignin-, cellulose-, casein-, grass- and beechwood-derived chars produced under the same combustion conditions. In addition to observing different degrees of alteration in starting materials, Knicker et al. [88] found that the possible charring products or units that could contribute to the structure of the biochars differed with starting material. For example, lignin-derived chars reveal a mostly aromatic structure with anthracene and benzanthracene as possible subunits, while cellulose-derived chars showed evidence for an abundance of O-containing structures (34% of the original oxygen preserved) with furans, benzofurans and pyranones as possible contributing units.

Kuo et al. [49], working with biochars derived from 3 different plant species, found that for a given combustion temperature between 200-300 ^{o}C the production of levoglucosan (a thermal degradation product of cellulose) in the biochars was directly related to the cellulose content of the starting materials. In another study Kuo et al. [99] also found that in addition to the effect of combustion temperature, the amount of cinnamyl-, syringyl- and vanillyl- lignin oxidation products in the plant derived biochars was a function of plant taxonomy. For example, biochars derived from angiosperms had higher syringly: vanillyl ratio compared to those derived from gymnosperms. Similarly,

biochars derived from non-woody tissue such as grass was found to have higher cinnamyl: vanillyl ratios than biochars derived from woody plant tissues.

1.3.3. Sorption characteristics

Studies evaluating sorption and sorption mechanisms on BC suggest that plant-derived biochars are capable of adsorbing both inorganic and organic contaminants by different mechanisms. Amuda et al. [100] reported removal efficiency of up to 90% of Zn^{2+} from a synthetic wastewater, by a modified activated coconut char produced at 600^{o}C. They concluded that Zn^{2+} sorption to the char occurred largely via ion exchange on deprotonated carboxylic acid sites; and was affected by solution pH, absorbent concentration, agitation time and particle size of the char. Wang et al. [101] also reported efficient removal of several heavy metals from low pH (<3) solutions by activated bamboo chars. They found that sorption efficiencies were dependent on both the heavy metal and the properties of the chars - as determined by manufacturing conditions. For example, sorption efficiencies of 88-100% were observed for Pb^{2+}, Cu^{2+} or Cr^{3+} compared to 20-80% for Cd^{2+} or Ni^{2+} and <20% for As^{5+}. Additionally, they reported that chars activated using steam were more efficient at adsorbing heavy metals from solution than those activated using carbon dioxide.

In addition to ion exchange, Chen et al. [102] suggested that sorption of Ag^{+} and Cu^{2+} on maple wood biochars occurred via alternative mechanisms. As evidence they pointed to the fact that, in their study; (i) stoichiometrically, the decrease in pH (indicative of proton exchange) with Ag^{+} and Cu^{2+} sorption was inconsistent with pure ion exchange; and (ii) pH decrease with sorption was not significantly different on an

oxygenated biochar sample compared to a hydrogenated sample. They also suggested the involvement of other functional groups (eg. -OH, -O-, =O, -CHO) that would not be deprotonated at the experimental pH (<6). Work by Cao et al. [79] also suggests the involvement of multiple mechanisms during heavy metal sorption on BC. They found that Pb^{2+} sorption on dairy manure biochars, followed a double Langmuir-Langmuir model compared to a single Langmuir model on the uncharred manure and an activated charcoal. Based on Pb speciation, XRD and FTIR data Cao et al. [79] concluded that 84-87% of Pb^{2+} sorption on the biochars was due to precipitation and 13-16% due to surface sorption. However, rather than ion exchange they attributed surface sorption to π-cation coordination bonding. This was also in contrast to Liu and Zhang [83] who, based on estimates of Gibb's free energy, attributed sorption of Pb^{2+} on rice husk and pinewood biochars solely to physical adsorption.

As with heavy metal sorption, studies investigating the sorption of different organic compounds on plant-derived char point to the involvement of several different mechanisms, depending on the properties of the organic compound and the char. Chun et al. [94] found that sorption of nitrobenzene and benzene by chars produced at temperatures >400 ^{o}C occurred almost exclusively by surface adsorption on carbonized surfaces, whereas sorption by lower temperature chars occurred via surface adsorption and partition into the residual organic-matter phase. Additionally, they concluded that the presence of polar functional groups on the chars resulted in a higher affinity for the polar solute (nitrobenzene) than the non-polar solute (benzene), with specific interaction playing a significant role in nitrobenzene sorption. Similar results were also reported by

Chen et al. [81] for sorption of naphthalene, nitrobenzene and dinitrobenzene on pine needle char produced at combustion temperatures between 100 and 700^{o}C. They suggested that for capacities comparable to monolayer coverage, sorption transitioned through a polarity selective process (200-400^{o}C) to a porosity selective process (500-600^{o}C) and then to a non-selective process at higher temperatures.

Contrary to the findings by Chun et al. [94], in looking at sorption of a series of polar and non-polar organic compounds on aerobic and hydrogenated wood chars, Zhu et al. [96] concluded that polar interactions with surface oxygen groups were not a significant driving force for adsorption. As evidence they argue that rather than decreasing with decreasing oxygen content (increase hydrogenation) sorption of the both polar and non-polar organic compounds in their study increased, which is inconsistent with expectation for dipole-dipole interactions or hydrogen bonding. Instead they suggested that sorption most likely occurred via π-π electron-donor-acceptor interactions of the polar compounds with the basal planes of the graphene sheets in the char. Similar interactions have been used in explaining sorption mechanisms of nitroaromatic compounds on chars and graphite [103, 104] and is thought to occur between electron-rich (donor) areas in the aromatic structure of char and electron-poor (acceptor) areas on the nitroaromatic compound.

Another mechanism that has been used to explain sorption of organic compounds on plant-derived char is the pore-filling process. In this process, sorption is believed to occur in the micropores of the chars and is govern by accessible micropore volume [81, 93, 105]. For pore filling mechanisms steric effects on sorption are critical. Steric effects

may arise due to polarity, planarity or molecular size of the organic sorbate or as a result of a polarity and pore size distribution of the char. For example, some researchers hypothesize that O functional groups on chars can preferentially adsorb water molecules forming clusters that competitively block sorption of organic solutes or prevent their penetration into the micropores[106, 107]. Cornelissen [51] found that for organic compounds with similar K_{ow}, sorption to BC was 50-200 times higher for planar molecules (eg. anthracene and phenanthrene) than their non-planar counterpart (eg. 2,2'-polychlorinated biphenyl). They attributed the differences in sorption between planar and non-planar compounds to steric hindrances as a result of the inability of the non-planar molecule to fit into the nanopores of the char. Zhu and Pignatello [104] also observed that, due to their size, tetra-substituted (eg. 2,4,6- trinitrotoluene) or tri-substituted benzenes (eg. 1,3,5-trichlorobenzene) were more sterically restricted from entering pores that are accessible to smaller substituted benzenes during sorption to BC.

CHAPTER II

SPECTROPHOTOMETRIC METHOD FOR ESTIMATING SOIL ORGANIC CARBON*

2.1. Introduction

Physical, chemical and biological processes occurring in soils are greatly influenced by soil organic carbon (SOC) content. Of such, estimates of SOC are often required for a wide variety of agricultural, environmental and engineering applications. Both quantitative and semi-quantitative methods are available for SOC determination [108]. Although quantitative methods for SOC are more accurate than semi-quantitative methods they are also typically more expensive and time consuming [109]; making them impractical for applications requiring rapid analysis of a large number of samples. For such applications and applications where spatial variability in SOC is more critical than measurement accuracy, semi-quantitative methods provide an attractive alternative to quantitative methods. In addition to being faster and cheaper, semi-quantitative methods for SOC determination often have the added advantage of being easily amendable for in-field use.

A number of semi-quantitative methods are available for laboratory and in-field estimation of SOC. These include soil color measurements [110], loss on ignition [111], remote sensing [112], and non-destructive or destructive spectroscopic techniques [113, 114]. Selecting an appropriate semi-quantitative SOC method can be challenging since

---

* Reprinted with permission from: O.R. Harvey, B.E. Herbert, J.P. Harris, E.A. Stiffler, J.-A. Crenwelge, Soil Sci. Soc. Am. J. 73 (2009) 822. Copyright 2009 by Soil Science Society of America.

methods have different advantages and disadvantages. Semi-quantitative methods vary in measurement accuracy, degree of site specificity, applicability for large-scale use and environmental friendliness.

For example, reported correlations between SOC and soil color for studies using quantitative soil color measurements to estimate SOC vary from 0.01 to 0.94 [110, 115-118] indicating that the accuracy of soil color as a proxy for SOC varies spatially and is largely site dependent. Variability in results from soil color- SOC studies have also been observed at different spatial scales, leading some researchers to conclude that soil color-SOC relationships were more suited for small scale rather than large scale applications [110, 117].

Studies evaluating loss on ignition (LOI) for estimating SOC also suggest strong soil property, landscape and land use influence on method performance [109, 111]. For example, LOI is often only considered to be suitable for use with coarse-textured or non-calcareous soil. In addition to oxidation of SOC, loss in structural water from clays and other inorganic constituents as well as decomposition of carbonates and hydrated salts also contribute to weight loss observed during LOI [119]. Loss on ignition is therefore likely to result in an overestimation of SOC. Abella and Zimmer [109] also found that the relationship between LOI and SOC varied across ten ecosystem types. Addition of soil texture, pH or $CaCO_3$ did not significantly improve the relationship, suggesting that factors such as land use and management were major factors influencing their results.

Wet oxidation methods for SOC determination, such as the widely used Walkley-Black method [120] are generally suitable for analysis of a small number of samples. For

large number of samples the method becomes cumbersome and time consuming [121]. Of even greater concern is the fact that wet oxidation methods use and generate hazardous materials such as Cr^{6+} and concentrated acid. Non-oxidative colorimetric methods such as the basic-EDTA method are typically more environmentally friendly, but are also prone to soil property effects [113]. For example, heating (85 ^{0}C) and incubation times of up to 4 h are required for efficient extraction of SOC from high clay content and high organic matter containing soils. Additionally Fe^{3+}, a major constituent of most soils, is a serious interferent since it forms a colored complex with EDTA. Soil extract color formed due Fe^{3+}-EDTA complexation could potentially be easily misinterpreted as color formed due to SOC, thereby resulting in overestimation of SOC.

Developing semi-quantitative methods for SOC estimation that are independent of soil properties, soil origin or land use are important for several reasons. In addition to providing a general method for SOC estimation, such methods would allow for: (i) better standardization of semi-quantitative SOC methods, (ii) better estimation and modeling of the spatiotemporal variability in SOC across small as well as large geographic areas, (ii) cross study comparisons, and (iii) the development of more consistent databases of SOC pools under different land use and management practices [122].

The purpose of this investigation was to develop and evaluate an alternative semi-quantitative method for estimating SOC that, in addition to being quick, easily executable, and easily amendable to field use, was less affected by soil properties and showed the potential for use across large geographic areas comprising of soils from different parent material, and or land use. Procedures for a new UV-Visible

spectrophotometric method for indirectly estimating SOC are presented. In developing the method we assumed that the ratio of base extractable UV active components in a soil: total SOC was relatively constant and therefore, for efficient extractions, soil extract absorbance could be used as a proxy for total SOC. Additionally we hypothesized that, for extractions of similar efficiency, absorbance of the UV active components in soil extracts adhere to Beer's Law; $A = \varepsilon lc$ where, A is absorbance, ε is the proportionality term or absorptivity of the analyte, l is the pathlength through the sample, and c is the concentration of the analyte; and a single absorptivity can be found for all soils, irrespective of other soil properties. We evaluated the feasibility of using the proposed method for large-scale SOC determination.

2.2. Materials and methods

2.2.1. Soils and humic material

A total of 146 (82 calcareous, 62 non-calcareous) soil samples from 11 major land resource areas (MLRA) across Texas were used (Fig. 1). Soils as well as data on their classification and physicochemical properties were obtained from Texas A & M University Soil Characterization Laboratory. Data on physicochemical soil properties included: soil pH (1:1 water extracts); sand, silt and clay content [123]; Calcite and dolomite content [123, 124]; Cation exchange capacity [125]; Base saturation [126]; and total SOC [127]. Samples were previously air-dried and ground to <2 mm when received and were used without further processing.

For verification purposes, total SOC in triplicate samples of 25 randomly selected soils were determined by difference between total carbon content (determined

by elemental analysis) and total inorganic carbon content [124]. Total carbon content for verification samples were measured by elemental analysis using a Vario EL *III* CNS elemental analyzer (Elementar Americas, Inc., Mt. Laurel, NJ, USA). Values were then compared to those obtained from the Soil Characterization Laboratory database, which uses dry combustion for SOC determination [127]. Regression analysis indicated that soil organic carbon determined for verification samples were not significantly different ($\alpha = 0.05$) from that determined by the Soil Characterization Lab, hence SOC contents from the database were used in all analyses. Sampling and analytical techniques used by the Texas A & M Soil Characterization Laboratory are outlined on their website (http://soildata.tamu.edu/methods.pdf).

A commercial humic acid (Sigma-Aldrich, Switzerland) was used as reference material for spectral comparison of soil extracts to humic or aromatic components. With the exception of sieving through a 63 micron sieve, to remove large particulate matter, the reference material was used without any further pretreatment.

2.2.2. Method development

Initial experiments were geared towards identifying a suitable extractant, soil: solution extraction ratio and appropriate UV wavelength for SOC quantification. These experiments were done using triplicate samples of 27 soil samples representing a range of inorganic characteristics (13 calcareous, 14 non-calcareous) and SOC contents (0 to 25 g kg^{-1}). The influence of soil: extractant ratios (1: 20, 1: 60, 1: 150, 1: 200, 1: 250, and 1: 450) and three soil extractants on the extraction of organic carbon were evaluated. The extractants tested were 0.25 mol L^{-1} NaOH (NaOH), 0.25 mol L^{-1} NaOH + 0.05 mol

L^{-1} EDTA (NaOH-EDTA; [113]), and 1 mol L^{-1} HCl followed by 0.25 mol L^{-1} NaOH + 0.1 mol L^{-1} $Na_4P_2O_7.10H_20$ (HCl + NaOH-pyroP; after Schnitzer, 1982). UV-Vis spectra (190-800nm) for soil extracts from 12 evaluation samples were compared to each other and to the spectra of the reference humic material. All chemicals used were reagent grade and extractants were made in nanopure water (Diamond UV ultra-pure water system, Branstead International, Iowa, USA). UV-Vis Spectra and UV absorbance data were collected on a Hitachi dual beam spectrophotometer (U-3010) with a pathlength of 1 cm. The appropriate wavelength for SOC quantification was taken to be the wavelength around the absorbance maxima that resulted in the best correlation between absorbance and the known SOC for the evaluation samples.

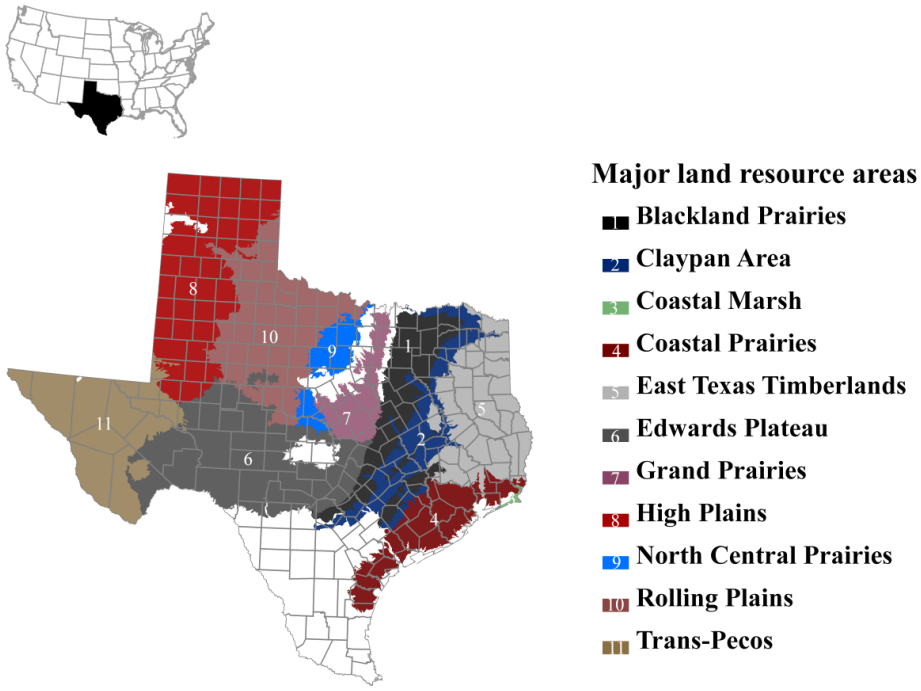

Fig. 1. Major land resource areas from which soil samples were obtained.

2.2.3. Method evaluation

Prior to evaluating the method's performance, an analysis of covariance was conducted to assess potential contributions of sample origin and soil properties to A_{300nm}, The analysis was conducted using all 146 soil samples with MLRA representing sample origin. The soil properties evaluated were SOC, soil texture, and whether the soil was calcareous or non-calcareous. These soil properties were selected because they were known to influence organic carbon extractability. The analysis of covariance was executed in SPSS (version 14.0) considering both single and interactive effects of factors.

For method evaluation, absorbance at the selected wavelength for analysis and dry combustion determined SOC (SOC_{DC}) data for 73 (50% of the 146 soil samples) randomly selected samples were used as calibration samples to estimate the absorptivity (ε) in Beer's Law. The calculated ε, was then used to determine SOC in the remaining 73 evaluation samples based on their absorbance at the selected wavelength. Method performance was evaluated by comparing the parameters (r^2, slope and intercept) of the dry combustion determined SOC vs. spectrophotometric estimated SOC regression line to those of the ideal 1:1 line with an intercept and slope of 0 and 1, respectively. Additionally, standard chemometric statistics such as standard error of prediction (SE_p) and relative prediction deviation (*RPD)* associated with the spectrophotometrically determined SOC were calculated according to Islam et al. [128]. Standard error of prediction for the evaluation samples was calculated as: $SE_p = [\sum(|SOC_{spect} - SOC_{DC}|) / n - 1]^{1/2}$ where, SOC_{spect} is the soil organic carbon determined by the proposed method,

SOC_{DC} is the dry combustion determined soil organic carbon, and n is the of samples in the validation data set. Relative prediction deviation for the evaluation samples was calculated as: $RPD = SD_{DC}/ SE_p$ where, SD_{DC} is the standard deviation of SOC determined by dry combustion and SE_p is from the previous equation.

Since the number of samples required for establishing a robust calibration will influence overall analysis time and cost we were also interested in evaluating the effect of calibration sample size on the performance of the proposed method. In doing so we adopted a more stochastic approach in evaluating method performance. Rather than a single randomization (as described above), multiple randomizations consisting of different ratios of calibration: validation samples were considered. Calibration: validation splits considered were 1: 9, 1: 3, 1: 2, 1: 1, 2: 1, 3: 1 and 9: 1. A total of 63 independent randomizations were performed for each calibration: validation split resulting in the generation of 63 unique calibration and validation set for each split. Method performance was subsequently evaluated by comparing the distributions of calibration and validation regression parameters, and chemometric statistics [128].

2.3. Results and discussion

2.3.1. Soil organic carbon extraction and analysis

In addition to being from several distinctly different land resource areas (Fig. 1), the soils used covered a wide range of moisture and temperature regimes as well as taxonomic families (Table 1), textural classes (Fig. 2) and chemical properties (Table 2). Such diversity is critical to method development since both the physical and chemical properties of soils are likely to influence organic C extractability and subsequently UV

absorbance-concentration relationships [18]. Although commercial and soil humic material are considered to be significantly different [129] we found that the UV-Vis spectra for soil extracts and reference humic acid in our study were qualitatively similar (Fig. 3). This was consistent with recent work by Sierra et al. [130] which showed that irrespective of source, all organic matter exhibited common fluorescence behavior in the UV region which were attributable to humic components. Additionally it is fairly well agreed upon that the absorption maxima (occurring around 260–300nm) observed in either material is attributable to the presence of aromatic components [131, 132]. Although the final pH of the HCl + NaOH-pyroP extracts (11.6±0.3) were lower than NaOH (12.7±0.02) and NaOH-EDTA (12.6±0.01) extracts, we obtained a fairly narrow range of absorption maxima (280– 300 nm) irrespective of extractant used or soil tested. This suggested no apparent effect of extractant on extracted UV-Vis active SOC fraction and was consistent with all extractants targeting the aromatic SOC fractions [131, 132]. Absorbance at 300 nm (A_{300nm}) was chosen for all analyses; however other wavelengths within the 280-320 nm range are likely to produce similar results.

Table 1
Taxonomic classification of soil used from each major land resource area, MLRA.

MLRA[a]	Soil Taxanomy[b]	Soil Series
1	Udorthentic Haplustolls; Udic Haplusterts	Austin; Heiden, Dimebox, Branyon, Houston Black
2	Aquic Arenic Paleustalfs; Chromic Vertic Albaqualfs;	Robco; Bonneville Tabor, Lufkin, Mabank;
	Oxyaquic Vertic Paleustalfs; Typic Albaqualfs	Zulch
	Vertic Paleudalfs; Udic Haplusterts	Annona; Burleson
	Aquic Paleudalfs; Udic Paleustalfs	Falba; Shiro
3	Typic Psammaqunts	Mustang
4	Aquic Glossudalfs; Oxyaquic Glossudalfs	Snake Creek; Orcadia
	Plinthic Paleudalfs	Hockley
5	Albaquultic Hapludalfs; Chromic Drystruderts	Spurger; Raylake
	Fluvaquentic Dystrudepts; Glossic Paleudalfs	Mooreville; Gallime
	Natric Vermaqualfs; Typic Glossaqualfs	Nona; Evadale
	Vermic Natraqualfs; Aquic Paleudalfs	Vidor; Fetzer
6	Lithic Haplustolls; Lithic Petrocalcic Calciustolls	Eckrant; Noelke
	Petrocalcic Calciustolls; Typic Argiustolls	Cho, Ozona; Rumple
	Typic Paleustalfs; Udertic Haplustolls	Pedernales; Krum
	Udic Calciustolls	Venus
7	Udic Calciustolls; Typic Haplustepts	Denton, Lewisville, Topsey; Brackett
8	Aeric Endoaqalfs; Aeric Halaquepts	Lamesa; Lenorah
	Torrifluventic Haplustepts; Typic Halaqeupts	Hindman; Cedarlake
	Typic Haplustalfs	Seagraves
9	Pachic Argiustolls; Udic Paleustalfs	Abilene; Bastrop
10	Typic Haplustepts; Calcic Haplustepts	Vernon; Shep
11	Fluventic Haplocambids; Sodic Ustic Haplocambids	Tornillo; Martillo, Straddlebug
	Ustic Haplocalcids; Ustic Torrifluvents	Chilicotal, Reagan, Potrillo, Pandale; Nillo

[a]Numbers correspond to legend shown in Fig. 1
[b]Subgroup level classification.

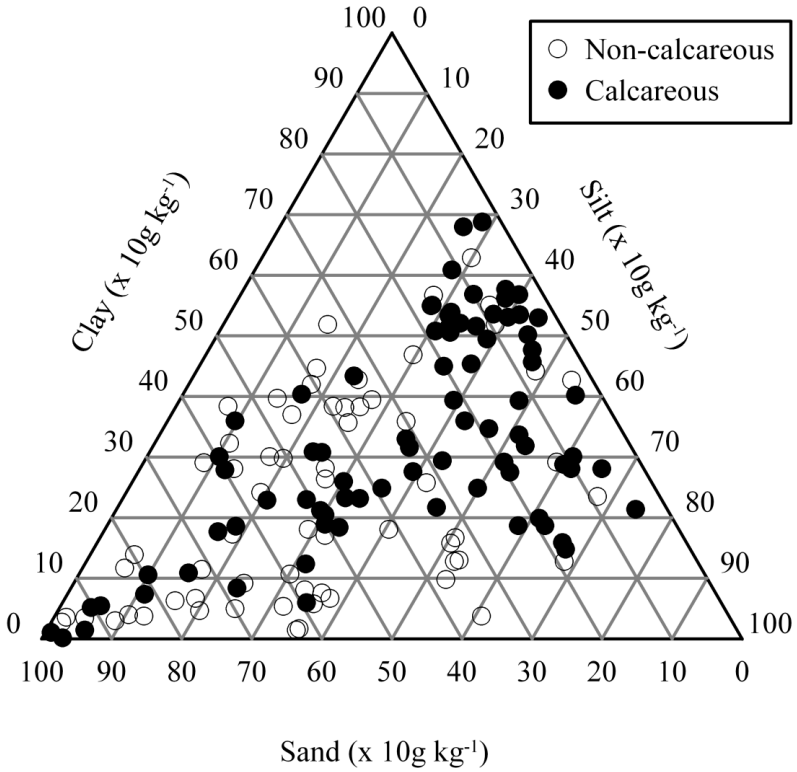

Fig. 2. Particle size distribution of soils used in UV-Vis method calibration and validation, *n = 146*.

Table 2
Summary of selected chemical properties of soil samples used, *n = 146.*

	pH[a]	CEC[b]	SOC[c]	$CaCO_3$[d]	$CaMg(CO_3)_2$[e]
		$cmol\_kg^{-1}$	----------$g\ kg^{-1}$----------		
Min	3.6	1.4	0.0	1.0	0.1
Max	9.0	61.6	46.0	797	152
Median	7.6	17.0	4.6	130	12.5
Mean (sd)	6.8(1.5)	21.0(15.6)	8.0(9.0)	217(228)	15.3(18.6)

[a] determined in 1: 1 soil: water mixtures
[b] cation exchange capacity
[c] dry combustion soil organic carbon;
[d] for calcareous samples only, *n= 82*.

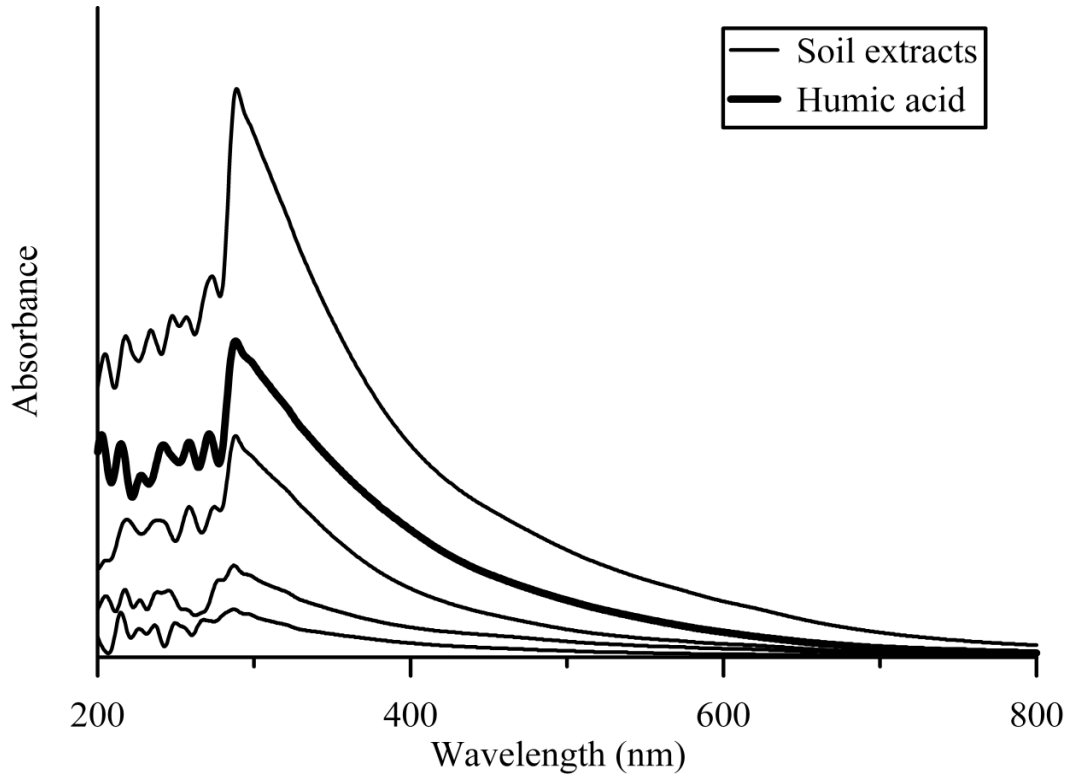

Fig. 3. UV-Vis spectra of soil extracts and reference humic acid. Spectra were obtained using 1 mol L^{-1} HCl followed by 0.25 mol L^{-1} NaOH + 0.1 mol L^{-1} $Na_4P_2O_7.10H_20$ as an extractant at a soil: extractant ratio of 1: 250 nm.

In evaluating the effect of soil: extractant ratio on the relationship between A_{300nm} and SOC we found that for a given extractant and soil, a soil: extractant ratio of 1: 250 produced the best linearity and correlation over the evaluation range (0- 25 g kg^{-1}). Higher soil: extractant ratios (1: 20, 1: 60, 1: 150 and 1: 200) became non-linear around 10- 15 g kg^{-1} SOC, while the lower soil: extractant ratio (1: 450) resulted in poor resolution at SOC below around 0.5% SOC. A soil: extractant ratio of 1: 250 was therefore selected for all subsequent extractions. Further discussions comparing extractant efficiency are therefore based on a 1: 250 soil: extractant ratio.

Results from initial experiments showed that while NaOH provided quantitative extractions for SOC determination in non-calcareous soils, for calcareous soils NaOH alone was not an efficient extractant (Fig. 4). This observation was consistent with observations made by Bowman et al. [113] for KOH only extracts. Stevenson [18] suggested that both clay and $CaCO_3$ in soils can physically protect organic matter from extraction. While physical protection of SOC from extraction was likely in our study, we believe that the dominant exchangeable cation(s) present in the system may also influence organic carbon extractability. In comparing the solubility of a reference humic material in NaOH (0.05 mol L^{-1}) and saturated $Ca(OH)_2$ (~0.025 mol L^{-1} or 0.05 mol L^{-1} OH^-) we found that the absorbance of the NaOH extract was at least an order of magnitude higher than that of the $Ca(OH)_2$ extract. Since equivalent OH^- concentration and the pH of both solutions were similar (pH > 12), we believe that the primary reason for the difference in absorbance observed was due to differences in interaction of Ca^{2+} and Na^+ with the humic acid. It is plausible that Ca^{2+} forms an organo-Ca complex with the humic acid that is more condensed and less prone to dissolution, than an organo-Na complex which is likely to be more dispersed. Other studies have also reported differences in organic matter behavior in the presence of monovalent versus polyvalent cations. Majcik and Tombacz [133] found that shear tolerance of humic acid-montmorillonite suspensions were enhanced with increased Ca^{2+} loading, due to increase flocculation. Stevenson (1994) also suggested that in many soils polyvalent cations may maintain soil organic matter in a flocculated and insoluble condition.

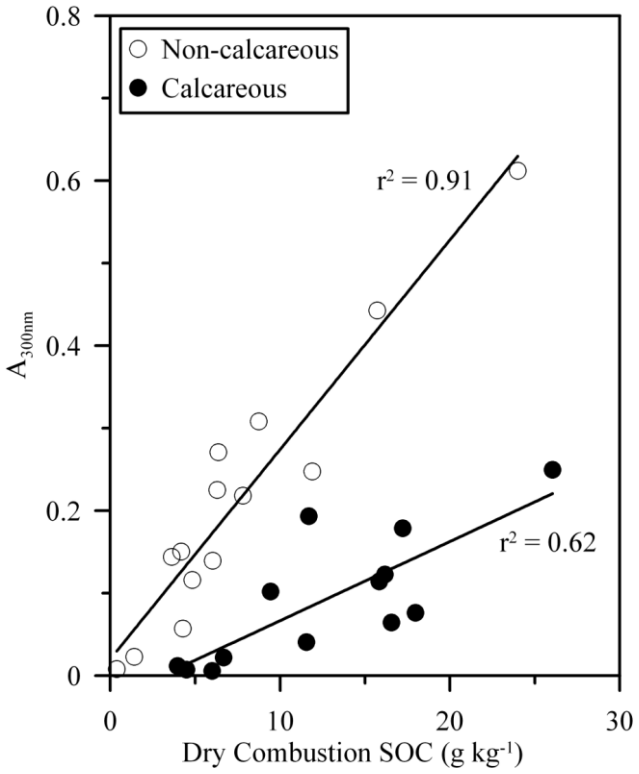

Fig. 4. Correlation between extract absorbance at 300 nm (A_{300nm}) and dry combustion determined soil organic carbon (SOC) for selected calcareous (*n = 13*) and non-calcareous (*n = 14*) soils using 0.25 mol L^{-1} NaOH solution as an extractant. Soil: extractant ratio = 1: 250.

Bowman et al. [113] found that a mixture of KOH and EDTA was more efficient at extraction of SOC from calcareous soils than $NaHCO_3$ or KOH only. Results from our initial experiments were consistent with this finding. Evaluations using the NaOH-EDTA extractant mixture and the 13 calcareous soils (shown in Fig. 4) showed an increase in both A_{300nm} and its correlation with SOC (r^2= 0.82) compared to NaOH. Despite this apparent improvement in correlation for calcareous soils, we found that when the non-calcareous evaluation samples (*n = 14*) were included in the regression, the A_{300nm}-SOC relationship for the NaOH-EDTA extracts was only linear up to 10 g kg^{-}

[1] SOC with an intercept that was 2.5 times that of the A_{300nm}-SOC relationship of HCl + NaOH-pyroP extracts. These observations suggested that the NaOH-EDTA extractant was inefficient in soils with high SOC, and was likely to overestimate SOC, particularly for lower SOC containing soils. Non-linearity at higher SOC is possibly the reason why Bowman et al. [113] recommended that, when using KOH-EDTA as an extractant for high organic matter high clay content soils, heating at 85° C for 2 h was needed for efficient SOC extraction. Bowman et al. [113] also noted that the formation of colored EDTA-Fe^{3+}complexes, were likely to be a major interferent in estimating SOC using the KOH-EDTA extractant. Both temperature and interferent effects were likely to have affected our results for the NaOH-EDTA extracts since all our experiments were conducted at room temperature and Fe^{3+} is a common constituent of oxidized soils. In fact it is possible that the higher intercept observed in the NaOH-EDTA extracts compared to HCl + NaOH-pyroP (which forms colorless complexes) extracts, was due to the presence of colored EDTA-Fe^{3+} complexes resulting in false positive detection or overestimation of SOC in NaOH-EDTA extracts.

The best extraction results were obtained using the HCl + NaOH-pyroP extractant at a soil: extractant ratio of 1: 250. In addition to having intercepts close to zero, A_{300nm}-SOC relationships were linear over the full SOC evaluation range (0-25 g kg^{-1} SOC) with statistically similar slopes and intercepts ($\alpha = 0.05$) for both non-calcareous ($r^2 = 0.89$) and calcareous soils ($r^2 = 0.91$). Therefore, a common equation could be used to describe the A_{300nm}-SOC relationship for both soil types suggesting that the HCl + NaOH-pyroP extractant was equally efficient at extracting UV active SOC

from both classes of soils. This was consistent with analysis of covariance results, using all 146 soil samples, which showed no significant influence on A_{300nm} –SOC relationship whether soils were calcareous or not (Table 3). Table 3 also showed no significant influence of MLRA or soil textural class on A_{300nm}, thereby suggesting that neither SOC source nor clay content had any significant impact on extraction efficiency of UV active SOC when HCl + NaOH-pyroP was used as the extractant. That MLRA did not significantly influence A_{300nm}-SOC relationship could be attributed to the fact that irrespective of source, extracted SOC fractions exhibited similar absorption behavior around 300 nm [130].

Table 3
Analysis of covariance of the effect of soil organic C (*SOC*), major land resource area (MLRA), soil texture, calcareous or non-calcareous on soil extract absorbance at 300 nm. Extraction were carried out using 1 mol L^{-1} HCl followed by 0.25 mol L^{-1} NaOH + 0.1 mol L^{-1} $Na_4P_2O_7.10H_20$ as soil extractant at a soil: extractant ratio of 1: 250, *n = 146*.

Source of variation	*df*	*SS*	*MS*	*F-value*	*P > F*
SOC[a]	1	0.527	0.527	25.326	<0.001
MLRA[b]	10	0.115	0.012	0.553	0.848
Calcareous[c]	1	0.016	0.016	0.787	0.377
Texture	13	0.143	0.011	0.529	0.901
MLRA * SOC	10	0.171	0.017	0.822	0.608
Calcareous * SOC	1	0.000	0.000	0.007	0.935
Texture * SOC	13	0.302	0.023	1.116	0.356
Error	96	1.997	0.021		
Total	145	30.032			

[a]Soil organic carbon determined by dry combustion
[b]Major land resource area
[c]Whether soil were calcareous or not (i.e. Y/N)

Although the ability of the pyrophosphate anion to form insoluble or colorless soluble complexes with metals [134] was important in enhancing SOC extractability and removing interference effects, we believe that the initial addition of excess HCl was also advantageous. Besides being important for carbonate dissolution, the added HCl likely played an important role in disrupting soil aggregation and clay-organic interactions thereby resulting in increased dissolution of organic carbon [18].

Based on all the initial experimental data the following procedure for rapid determination of SOC in soils is proposed:

(i) Weigh 0.1g of air-dried soil into a 50 ml polypropylene centrifuge tube and 5 ml of 1 mol L^{-1} HCl;

(ii) Shake by hand for 15-20 seconds at 1 minute intervals for 5 minutes;

(iii) Add 20 ml of NaOH-pyroP extractant solution and shake by hand for 15-20 seconds at 1 minute intervals for an additional 5 minutes;

(iv) Filter approximately 10 ml of extract through 0.45 μm polycarbonate syringe filters;

(v) Measure absorbance of the filtrate, relative to a reagent blank, at 300 nm.

(vi) Use a calibration curve (developed using Beer's Law and soils of known SOC content) to determine SOC content of sample based on its measured absorbance.

2.3.2. Method performance

The correlation between A_{300nm} (obtained using the proposed method) and SOC for the calibration samples ($n = 73$) is shown in Fig. 5. In contrast to what was observed

for NaOH only extracts (Fig. 4). Fig. 5 indicate that for soil extracts obtained using the proposed method, a common regression line could be used to describe the relationship between A_{300nm} and SOC in both calcareous and non-calcareous soils; thereby eliminating the need for developing separate calibrations for calcareous and non-calcareous samples. Figure 5 highlighted two important features of the proposed method: (i) The A_{300nm}-SOC relationship of the HCl + NaOH-pyroP extracts followed Beer's law; and (ii) The relationship was linear beyond the maximum SOC of the evaluation samples (25 g kg^{-1} SOC).

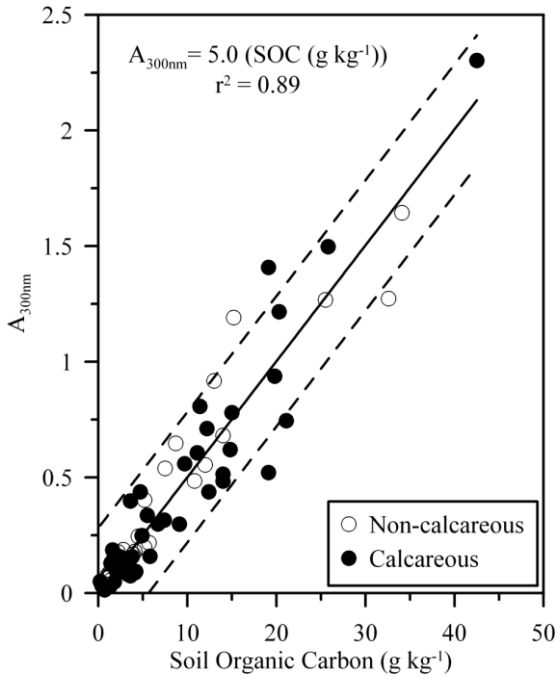

Fig. 5. Relationship between soil extract absorbance at 300 nm (A_{300nm}) and soil organic carbon (SOC) for calibration samples ($n = 73$) using the proposed method.

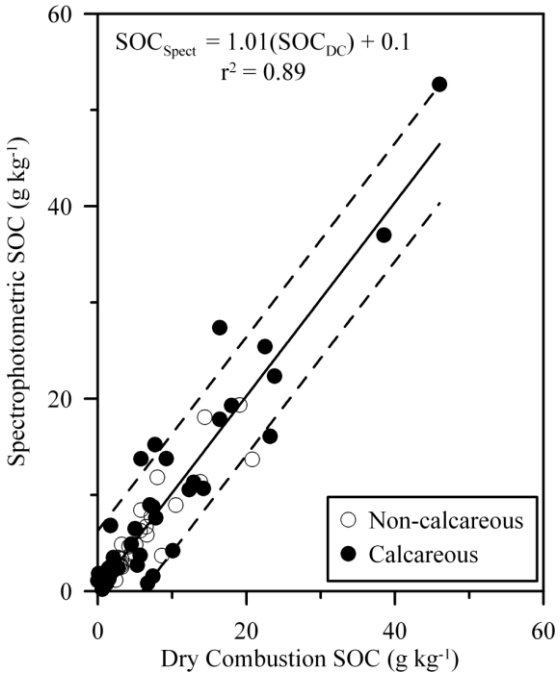

Fig. 6. Comparison of SOC for validation samples (n = 73) as measured by dry combustion and determined sphectrophotometrically using the proposed method. Envelope (----) represent 95% confidence interval.

Based on the regression equation in Fig. 5, Beer's law for calibration samples could be written as; $A_{300nm} = 5.0 \times SOC$ where, $\varepsilon l = 5.0$ and *SOC* is the known SOC content for each of the 73 calibration samples. Since pathlength, *l* is 1 cm and SOC_{DC} is measured in grams per kilogram (g kg^{-1}), then it follows that the average absorptivity of the UV active SOC in the soil extracts of the calibration samples at 300 nm was 5.0 kg g^{-1} cm^{-1}. The calibration equation can therefore be rearranged to give; $SOC = 20 \times A_{300nm}$. The rewritten calibration equation is more intuitive for using A_{300nm} to estimate SOC. When this equation was used to estimate SOC in the 73 validation samples (not used in the calibration), estimated SOC were in close agreement with dry combustion determined SOC (Fig. 6). No significant difference ($\alpha = 0.05$) was found between the

regression line in Fig. 6 and the ideal 1:1 line. The standard error and relative prediction deviation associated with spectrophotometric SOC (compared to dry combustion SOC) were 2.9 kg g^{-1} SOC and 3.2, respectively; indicating that in addition to being of fairly accurate, the proposed method was also robust with standard deviation of dry combustion measured SOC being more than 3 times the SE_p [128].

Further evidence of method stability was observed by comparing the effect of calibration sample size on calibration and validation regression parameters. For calibration sample size ranging from 10% (1: 9 calibration: validation split) to 90% (9: 1 calibration: validation split) of the 146 samples used in the study, ε and r^2 for calibration equations were similar (Table 4). Table 4 also showed that irrespective of calibration sample size, accuracy of the proposed method in determining SOC was similar, indicating that by using a single calibration equation developed using quantitatively determined SOC and soil extract absorbance from as few as 15 samples (~ 10% of the 146 samples used in study), SOC in a large number of soils could be determined. As with any other analytical techniques, it is recommended that SOC in the calibration and prediction datasets cover a similar range. Results shown in Table 4 indicate that the use of equation 5, with soil extracts obtained using the proposed method, was suitable for estimating SOC in the soils used in this study. Since the method was not evaluated with samples containing >50 g kg^{-1} SOC contents we would recommend developing a separate calibration for soils with higher SOC.

Table 4
Variation in method calibration and validation regression parameters when data (*n = 146*) was split randomly into calibration and validation sets of different sizes. Values are the mean (standard deviation) based on 63 independent randomizations for each calibration: validation (C: V) split.

	-------Calibration[a]----		----------Validation[b] ----------				
C: V	ε[c]	r^2	Slope	Intercept	r^2	SE_p[d]	RPD[d]
1:9	5.2(0.5)	0.87(0.09)	0.97(0.10)	0.2(0.2)	0.89(0.01)	2.9(0.3)	3.0(0.3)
1:3	5.1(0.3)	0.88(0.06)	0.99(0.07)	0.2(0.2)	0.89(0.02)	2.9(0.2)	2.9(0.3)
1:2	5.2(0.2)	0.89(0.04)	0.96(0.07)	0.2(0.1)	0.89(0.02)	2.9(0.3)	3.0(0.3)
1: 1	5.1(0.2)	0.89(0.03)	0.98(0.07)	0.2(0.3)	0.89(0.03)	3.0(0.3)	2.9(0.4)
2: 1	5.1(0.1)	0.89(0.02)	0.97(0.09)	0.3(0.3)	0.89(0.04)	2.9(0.4)	3.0(0.6)
3:1	5.1(0.1)	0.89(0.02)	0.97(0.09)	0.3(0.4)	0.87(0.06)	3.0(0.4)	2.9(0.6)
9:1	5.1(0.1)	0.89(0.01)	0.96(0.16)	0.3(0.9)	0.87(0.12)	2.6(0.8)	3.4(1.4)

[a] Regression of soil extract absorbance at 300 nm against dry combustion SOC
[b] Comparison of dry combustion determined SOC to that determined spectrophotometrically for samples not included in calibration.
[c] Absorptivity (kg g^{-1} cm^{-1})
[d]Chemometric parameters: SE_p, standard error; *RPD*, relative prediction deviation.

2.4. Summary and conclusions

The ease of execution, rapid analysis and fairly good accuracy of the proposed method makes it an attractive alternative for both field and laboratory use. Although not accurate enough to be considered quantitative, the proposed method would be suitable for quick analysis of a large number of samples where accuracy to within ±10% was not required. With good quality field spectrophotometers now readily available, the proposed method could be easily adopted for field use. Modification for field use could include substituting weighing of soil samples with using a scoop, and making corrections for soil moisture and temperature effects, if necessary. Additionally since

this study was conducted on air-dried soils and under room temperature conditions (~24^{o}C) the method may need to be modified for wet soils or extreme temperature conditions.

The ratio of soluble aromatic: total SOC present in the soil are likely to be the major limitation to applicability of the proposed method. The method assumes that this ratio is more or less constant across a large spatial extent and therefore can be used as a proxy for total SOC. While this may be true for most soils, since non-aromatics are usually rapidly biodegraded (Schnitzer, 1982), for soils comprising a significant non-aromatic or insoluble aromatic fraction the method will likely underestimate SOC.

CHAPTER III

NATURAL ORGANIC MATTER AND THE FORMATION OF CALCIUM SILICATE HYDRATE IN LIME-STABILIZED SMECTITES: A THERMAL ANALYSIS STUDY

3.1. Introduction

Long-term strength in lime- or cement-stabilized soils is attributed to the formation of pozzolanic reaction products. One major class of pozzolanic product formed in stabilized soils is the calcium silicate hydrates (CSH) which are typically designated as CSH gel, CSH1 or CSH2. CSH gel is amorphous, while CSH1 and CSH2 are poorly crystalline with Ca: Si ratio close to 1 and 2, respectively [135]. Formation of CSH compounds in lime-soil systems occur via a dissolution-precipitation mechanism [42]. In the dissolution phase the high (>12) pH environment, created by the addition of the lime to the soil, results in incongruent dissolution of silica from silicate bearing soil minerals (eg. clays and quartz) and congruent dissolution of more soluble Si-bearing minerals such microcrystalline opal. In the precipitation phase the dissolved silica reacts with free calcium (from soil solution or dissolved lime) to form the CSH precipitate, which increases soil strength though cementation of soil particles.

Perturbation in either the dissolution or precipitation phase of CSH formation is likely to have significant impacts on the stabilization of soils with lime or cement. Although many studies have been conducted to elucidate the effects of lime/cement addition on soil properties, very little direct information is available on how naturally occurring soil characteristics influences the formation/activity of pozzolanic reaction

products such as CSH. For example, addition of cement to soils containing organic matter is known to result in much lower relative strength gains than a soil with little or no organic matter [44, 47, 136, 137]. It is unclear however, whether the negative impact of organic matter on cement stabilization is due to inhibition of pozzolanic reaction product formation or inhibition of its cementation activity. Hampton and Edil [47] highlighted the need for more research on understanding the fundamental mechanisms contributing to changes in the geotechnical properties of stabilized organic soils. Understanding the mode of action of potential soil characteristics on pozzolanic product formation/activity in lime-soil systems is important for effective lime stabilization project design and mitigation efforts in both engineering and environmental applications (e.g. highway construction and waste solidification).

Investigation of the effects of natural organic matter on CSH formation in stabilized soils is operationally limited by the common techniques used to quantify and characterize the CSH phases. The poorly crystalline nature of CSH phases make them difficult to study by crystallographic techniques such as X-ray diffraction. Characterizing CSH formation using XRD require hydrothermal incubation conditions and/or sample incubation periods on the order of several months to years [42, 135, 138]. Considering that assessments of stabilization are typically conducted within days or weeks of treatment and environmental temperatures are typically < 40 ^{o}C, such an approach would be impractical. Thermal analysis is widely used in the identification of new phases formed in lime or cement stabilized soils and has been used to identify CSH in lime/cement stabilized systems [135, 138-140]. To our knowledge, no previous study

has applied thermal analysis to the investigation of the influence that perturbants may have on pozzolanic activity in either lime- or cement-stabilized soils.

In this study, heat-flow differential scanning calorimetry (DSC) and thermogravimetric analysis (TG) were used to elucidate the mode of action of organic matter on pozzolanic activity in lime-stabilized soils. In cases where peaks are difficult to decipher or differentiate the complementary derivative of the thermal signals will be used to identify peaks locations and limits. We postulated that if the negative impact of organic matter on lime stabilization is due to the inhibition of pozzolanic product formation, then formation of CSH should decrease with increasing organic matter content. On the other hand, if soil cementation by CSH, rather than the formation of CSH, is being inhibited by organic matter, then CSH formation should be similar, irrespective of organic matter source or content.

3.2. Materials and methods

3.2.1. Soils, lime and natural organic matter

We used model soils comprising of 60.0% quartz sand and 40.0% smectitic clay, by weight. Two such soils were used: one containing Gonzales clay (Southern Clay Products, Gonzales, TX) and the other a Panther Creek clay (Ward Natural Science, Rochester, NY). X-ray diffraction confirmed both clays to be smectites (to be discussed later). The clays were described by the suppliers as a Ca-bentonite and Na-montmorillonite, respectively and were selected to represent smectitic soil with different mineralogies. For simplicity, the model soils will be referred to as GB and PCM for Gonzalez bentonite and Panther Creek montmorillonite, respectively. Clays were

obtained as fine powders and were used as received. Cation exchange capacity of the GB clay was 81 cmol kg^{-1} and that of the PCM clay was 93 cmol kg^{-1}. The quartz sand used was Ottawa sand. The lime used was a hydrated lime ($CaOH_2$) obtained from Fisher Scientific. Organic matter from 4 sources was used: (i) a commercial humic acid (cHA; MP Biomedical, Solon, OH); soil humic acid (sHA); soil fulvic acid (sFA) and lignite. The cHA was used as received and the sHA and sFA were extracted from a forest soil and purified according to techniques described in Tan [19]. The lignite was received as large clods from a local mine site (Rockdale, TX) and prior to using, was grounded to pass through a 63 micron sieve.

3.2.2. Paste experiments

Two sets of paste experiments were conducted. The first set of paste experiments was conducted primarily to elucidate qualitative changes in lime-soil reaction products as a function of lime content in the absence of organic matter. In these experiments, 1: 1 solid: solution pastes were incubated under conditions of 100% humidity and 23 ^{o}C for 10 days. Pastes contained: 10g model soil; 0 to 20% hydrated lime; and an equivalent mass of de-ionized water. The second set of the paste experiments was conducted to evaluate the effect of different sources of natural organic matter on lime-clay reactions. The composition of the pastes in these experiments were: 10.0 g model soil; 8.0% or 12.0% hydrated lime for the GB and PCM, respectively; 0 to 5.0% natural organic matter; and an equivalent mass of de-ionized water. Incubation temperature and humidity conditions were the same as in set 1 but incubation time was 28 days rather than 10 days.

Following incubation the pastes were flash frozen using liquid nitrogen (to inhibit further reaction), freeze dried, lightly crushed and sieved through a 63 micron (#230) sieve. Mineralogical composition of the <63 micron fraction was assessed using X-ray diffraction (XRD), DSC and TG/DTG. For XRD analysis (Bruker, Madison, WI), samples were mounted as dry powders and scanned over the 4-70 2θ range. For DSC and TG/DTG analysis (SDT Q600, TA instruments, New Castle, DE), approximately 20 mg of <63 micron fraction of each paste were placed in a ceramic sample crucible and analyzed between 50 and 1000 ^{o}C at a ramping rate 10 ^{o}C min^{-1}.

3.2.3. Core experiments

Cylinderical cores, 5 cm high and 3.3 cm in diameter, of model soil-lime-organic matter mixtures were made using the Harvard miniature apparatus (Humboldt, Norridge, IL.). Each core contained 60% sand, 40% clay, 6% lime, 0 to 5% cHA and 22.5% moisture content by weight and was packed to a dry bulk density of 1.63 g cm^{-3}. Cores were incubated at 100% humidity and 23 ^{o}C for 3, 7, 10, 14 and 28 days. For a given incubation period, triplicates of cores were made for each of the four cHA contents resulting in a total of 24 (4 cHA content × 2 clay types × 3 replicates) cores per incubation period.

Following incubation, the unconfined compressive strengths (UCS) of the cores were measured (Instron Universal Testing System, model 5583, Norwood, MA) then the cores were dried at 70 ^{o}C for 24h, lightly crushed and sieved through a 63 micron sieve. About 40 mg of the ≤ 63 micron fraction was then analyzed by DSC and TG/DTG as described earlier.

3.3. Results and discussion

3.3.1. Lime-soil reactions in organic matter-free conditions

Thermograms for GB, PCM and hydrated lime starting materials are shown in Fig. 7 and those for the 10 days incubated lime-soil pastes are shown in Fig. 8. Comparison of the thermograms in the two figures shows several common, as well as distinct, features. Endothermic effects and associated weight loss observed at 50- 200 ^{o}C and >300 ^{o}C in both the clays and incubated pastes are attributable to dehydration and dehydroxylation of clay[141], respectively. Endothermic effects and associated weight loss in the lime starting material and pastes are attributable to dehydration/ dehydroxylation of the $CaOH_2$ (350-500 ^{o}C) and degradation of $CaCO_3$ (500-700 ^{o}C). The presence of $CaCO_3$ in the starting material and incubated pastes are indicative of carbonation. The weight loss associated with $CaCO_3$ impurity in the starting material was 4.2%. Detectable carbonation was only apparent in incubated lime-soil paste samples containing >8% lime (for PCM) and >12% lime for the GB samples. This coincided with the occurrence of unconsumed lime (as evidenced by the 350-500 ^{o}C endotherm in these samples) and was consistent with previous work which found that $CaCO_3$ often form as a result of the reaction of CO_2 with lime in lime-stabilized soils [39, 138, 142].

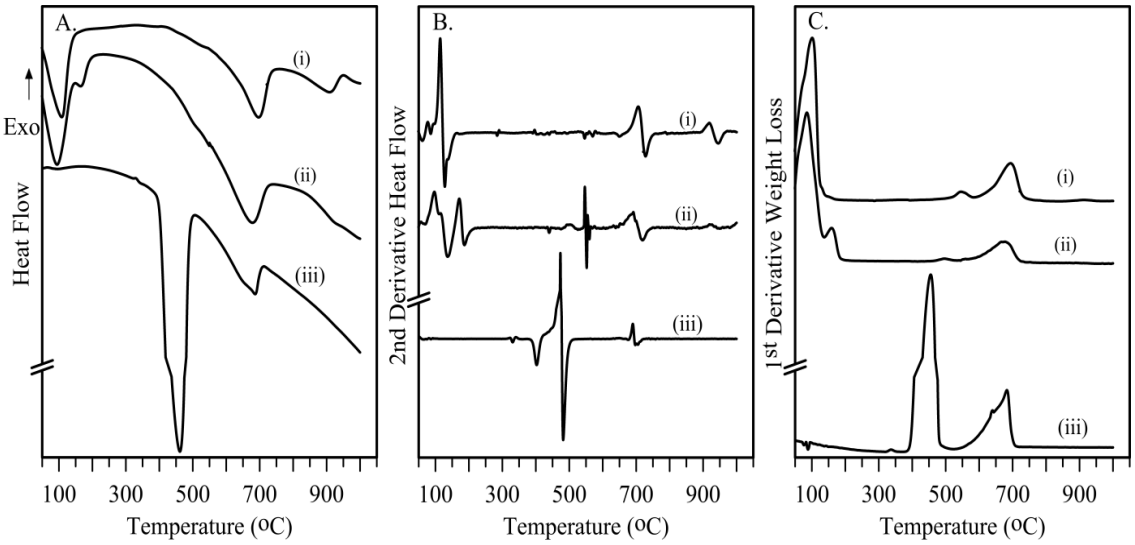

Fig. 7. (A and B) Differential scanning calorimertry and (C) derivative thermogravimetry thermograms of (i) Panther Creek montmorillonite, (ii) Gonzalez bentonite, and (iii) hydrated lime starting materials.

In addition to carbonation reactions, difference in the hydration characteristics of the clays (Fig. 7), changes in hydration characteristics with lime content and formation of new reaction products in the lime-soil paste were also apparent (Fig. 8). Differences in the thermal behavior of the clays are attributable to differences in the dominant exchangeable cations and their respective hydration characteristics. For example, the endothermic peak at approximately 170 ^{o}C in the GB starting material (not observed in the PCM starting material) is consistent with the loss of water from the hydration sphere of Ca^{2+}[143].

Increasing lime content in the lime-soil paste resulted in the broadening of the dehydration region to higher temperatures (Fig. 8). In GB pastes containing ≥12% lime

and PCM pastes containing ≥6% an additional weight loss (dehydration) peak around 150 ^{o}C is apparent (Fig. 8B and E).

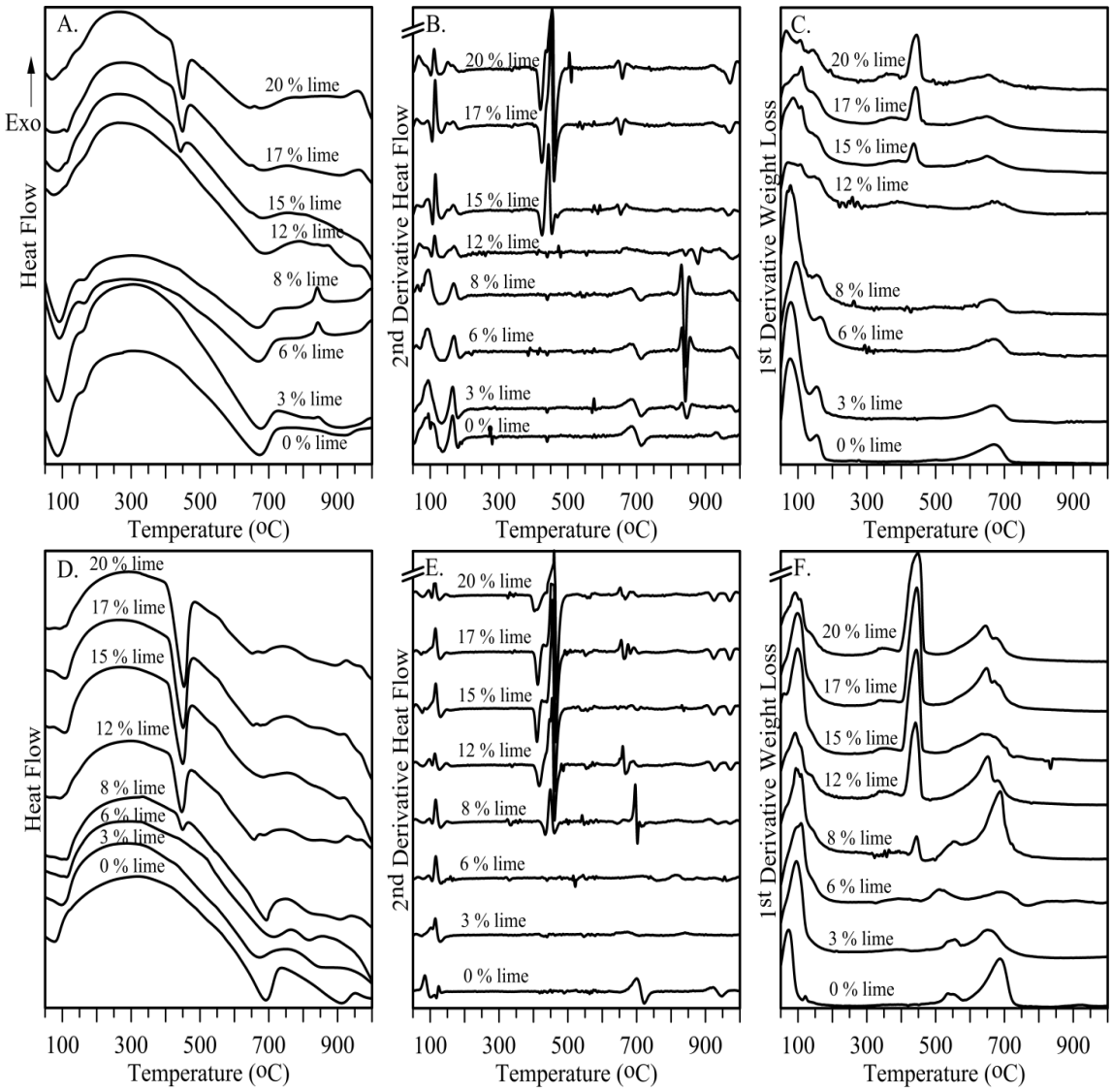

Fig. 8. (A, B, D and E) Differential scanning calorimertry and (C and F) derivative thermogravimetry thermograms of 10 day incubated (A-C) Panther Creek montmorillonite and (D-F) Gonzales bentonite pastes containing different amounts of hydrated lime.

Coincident with the occurrence of the 150 ^{o}C dehydration peak is a doublet of exothermic peaks occurring in the 800- 900 ^{o}C range for the 12% lime GB paste and the 900-1000^{o}C range for >12% lime GB pastes and ≥6% lime PCM pastes. These peaks are indicative of the formation of new reaction products. Earlier studies [138-140, 144] of lime-clay systems have attributed the occurrence of water loss peaks around 120-160^{o}C to the dehydration of CSH and exothermic peaks in the 900-1000 ^{o}C range to the recrytallization of CSH2. The exothermic nature and the absence of any weight loss associated with the 900-1000 ^{o}C peaks are consistent with such recrytallization reactions [141]. Further evidence of CSH2 formation is suggested by the additional weight loss around 300-350^{o}C in these samples. Glenn [138] suggested that the occurrence of this additional weight loss is useful in distinguishing CSH2 from CSH1. Designation of the 150 ^{o}C peak to the sole dehydration of CSH, was difficult since dehydration of interlayer and associated hydrated cations (such as Ca^{2+}) occurs in the same region.

Formation of new reaction products was also evident in the 3-8% lime GB pastes (Fig. 8A and B). In contrast to that observed at higher lime contents and for PCM pastes, the new reaction product in these pastes was evident as a single exotherm between 800-900 ^{o}C. No weight loss was associated with the exothermic peak, also consistent with a re-crystallization reaction.

Earlier studies [138, 140] have attributed the occurrence of an exothermic peak around 850 ^{o}C to the presence of CSH1. The increase in intensity of the 850^{o}C peak with lime content up to 8% lime is indicative of increase CSH1 production with lime content. At 12% lime there appears to be a transition from CSH1 to CSH2 formation. For the PCM pastes only CSH2 formation was observed, with its production increasing up to 12% lime and then leveling off. The formation of CSH2 appears to be favored under excess lime conditions. No new reaction products were observed in the 3% lime PCM paste, however some transitions were apparent when compared to the 0 % lime sample. Most notably were changes in hydration and the disappearance of the dehydroxylation peak at around 950 ^{o}C. X-ray diffraction analysis (Fig. 9) also showed an increase in interlayer d-spacing (from 1.0 – 1.4 nm) consistent with increase hydration and Ca^{2+} exchange for Na^{+} [39, 138]. Only diffraction peaks attributable to starting materials and possibly calcite were observed in lime-soil paste of Fig. 9, indicating that the new reaction products formed were either present in small quantities (<5%) or amorphous to poorly crystalline.

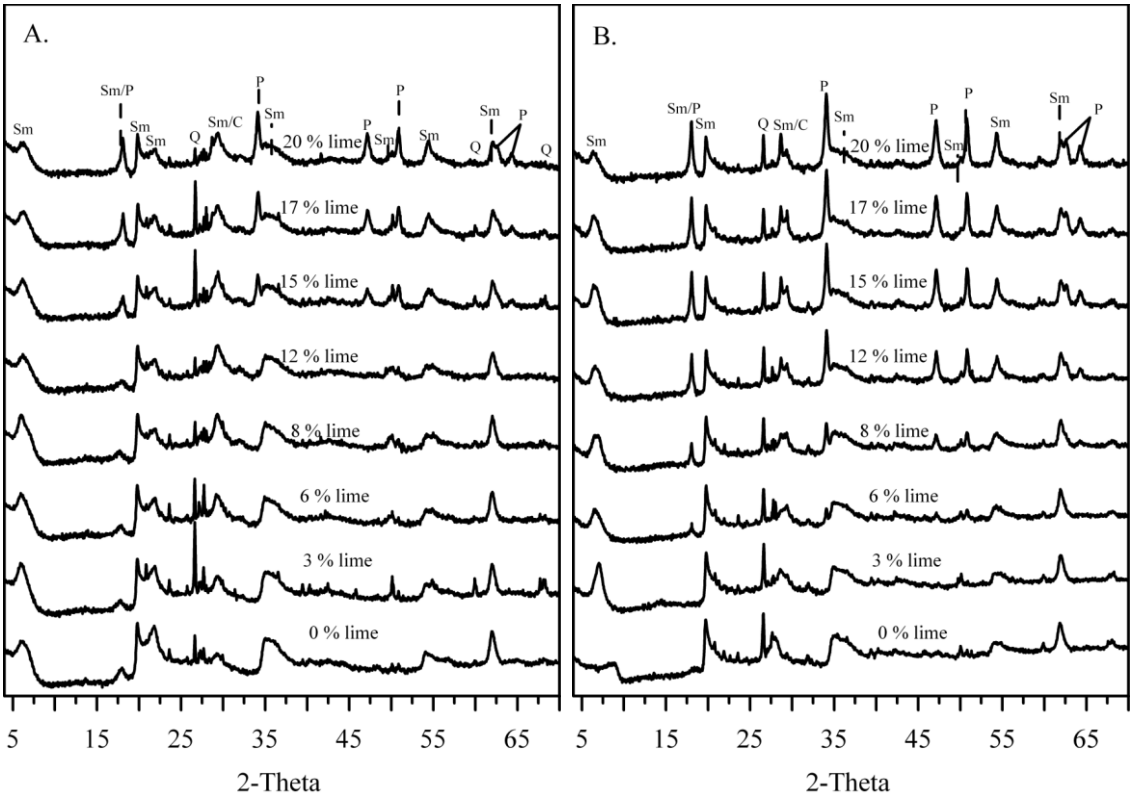

Fig. 9. X-ray diffractograms of 10 day incubated 1:1 soil: water (A) Gonzales bentonite, and (B) Panther Creek montmorillonite pastes containing 0-20% hydrated lime. Peaks indicate the presence of smectite (Sm), $CaOH_2$/ portlandite (P), quartz (Q) and possibly calcite(C).

3.3.2. Lime-soil reactions in the presence of natural organic matter

Differential scanning calorimetry thermograms for core samples containing varying quantities of organic matter are shown in Fig. 10. As in the organic matter free paste experiments, exothermic peaks attributable to the formation of CSH phases were also observed in core samples containing organic matter. New exothermic peaks in the 200-600 ^{o}C range, which increased in intensity with increasing organic matter content

were attributable to the oxidation of the added humic acid (cHA). Other peaks such as those observed between 300 ^{o}C and 350 ^{o}C in the 3 day GB sample as well as the 3 and 7 day PCM samples appear to be transitional phases, likely associated with the hydrated lime starting material (Fig. 7).

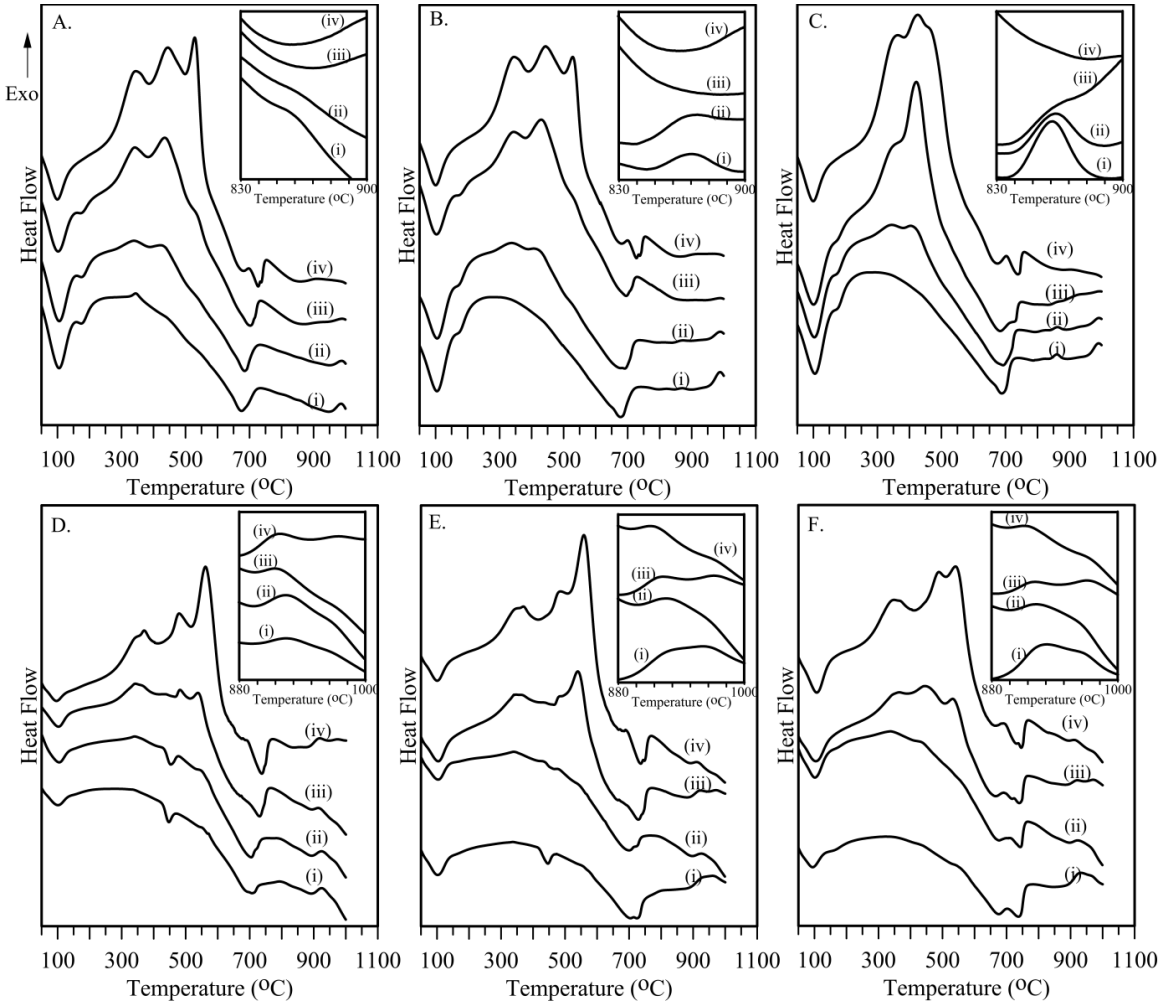

Fig. 10. Thermograms of (A-C) Gonzalez bentonite and (D-F) Panther Creek montmorillonite core samples containing six percent hydrated lime plus (i) 0, (ii) 0.5, (iii) 2 or (iv) 5% commercial humic acid. Samples were incubated at 100% humidity and 23 ^{o}C for (A, D) 3 days, (B, E) 7 days or (C, F) 28 days.

For a given incubation period, the concomitant decrease in the intensity (and in some cases the absence) of the CSH peaks observed with increasing cHA content suggests that the presence of humic acid had an inhibitory effect on the formation of CSH (Fig. 10 insets). Unconfined compressive strengths (UCS) of the lime-stabilized cores also decreased with increasing humic acid content (Fig. 11).

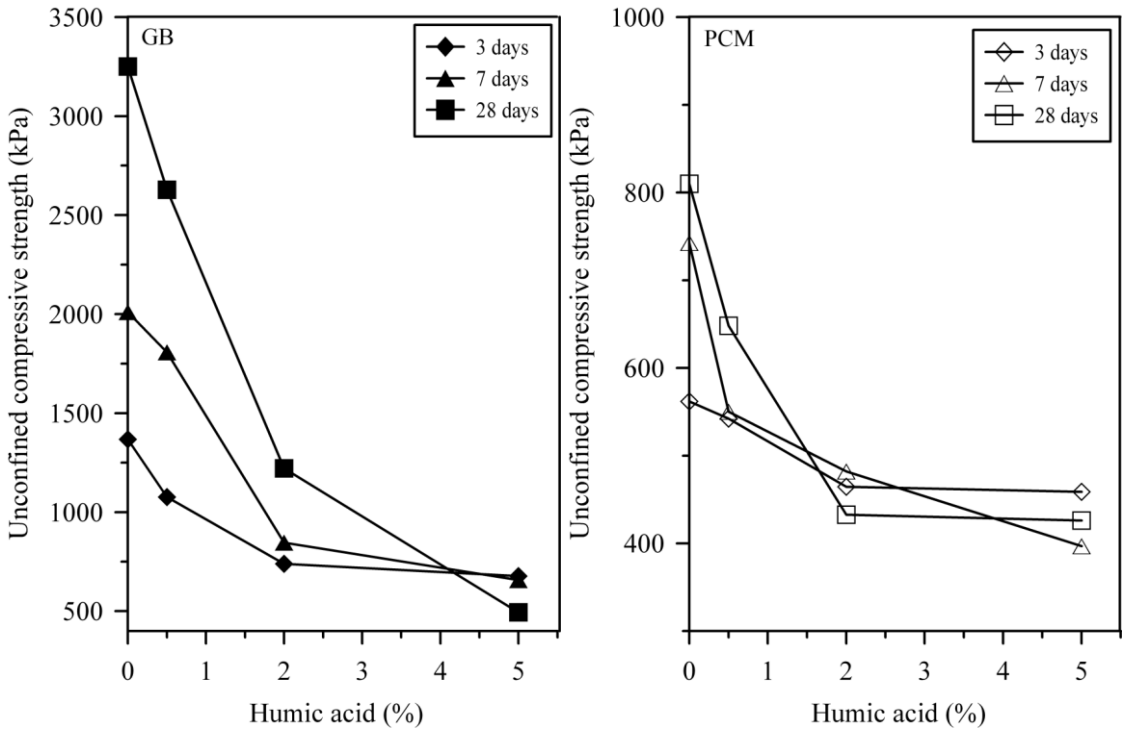

Fig. 11. Unconfined compressive of lime-stabilized cores as a function of humic acid added. Samples were incubated at 100% humidity and 23 ^{o}C for 3 days, 7 days or 28 days.

A strong linear correlation between the UCS of the cores and the amount of energy evolved (given by peak area) during CSH re-crystallization points to a direct link

between CSH formation and strength development (Fig. 12). This was a very significant observation as it points to the inhibition of CSH formation as the primary mode of action of natural organic matter as a perturbant in lime stabilized soils. The decrease in intensity of the CSH peaks with increasing cHA content also provides a valid explanation for the observed decrease in strength gains in lime/cement stabilized soils as soil organic matter content increase. In the presence of organic matter, changes in CSH formation (peak intensity) varied with both the type of clay and the CSH phase formed. For example, although the formation of CSH1 was completely inhibited in GB samples containing 5% cHA (and in some cases 2% cHA) CSH2 formation in the PCM was only retarded. This suggests that in addition to organic matter content, soil mineralogy is likely to significantly influence the degree to which organic matter inhibits CSH formation and subsequently lime/cement stabilization in soils. The fact that even for the same organic matter source, lime content, clay content and incubation conditions differences in CSH inhibition were observed also presents one possible explanation for the variability in successful stabilization of organic soils reported in the literature [44, 145, 146].

Both the formation of CSH and the inhibition of its formation by cHA showed evidence consistent with kinetically-controlled processes. As can be seen from the insets in Fig. 10, with the exception of the 5% cHA GB sample (which showed no evidence of CSH formation even after 28 days of incubation) the intensity of the CSH peaks for a given cHA content generally increased with time, indicative of increase CSH formation and is consistent with studies of strength development in lime/cement stabilized soils

[39]. Further evidence of the kinetically-controlled inhibition of CSH formation by organic matter was seen in GB samples containing 2% cHA. Calcium silicate hydrate formation in these samples was not observed until after 10 days of incubation (compare to 3 days for 0 and 0.5% cHA samples). This additional lag of 7 days is consistent with an initial inhibition on CSH formation which is overcome with time. Such inhibition was most likely due to cHA exhibiting kinetic controls on the dissolution and/or precipitation stage of CSH formation because of HA known acid-base properties or ability to complex Ca^{2+} [18, 19] .

A number of possible mechanisms, possibly acting simultaneously, could account for the observed inhibitory effects of organic matter on CSH formation. The first and most commonly cited mechanism is the complexation of dissolved Ca^{2+} ions by organic matter in order to satisfy its cation exchange capacity. Eades and Grim [42] suggested that replacement of absorbed cations on clays by Ca^{2+} precedes the formation of new reaction products with CSH forming only after exchange sites become fully occupied by Ca^{2+}. In the presence of natural organic matter sources such as humic and fulvic acids the cation exchange capacity of the soil will increase [19]. More Ca^{2+} would be required to satisfy the cation exchange capacity of the soil and thereby reduce the amount of Ca^{2+} available for CSH formation. Complexation of Ca^{2+} would therefore be expected to affect the precipitation phase of CSH formation and have been used to explain lower strengths gain in lime stabilized soils [44, 145, 146]. Based on equilibrium principles one would actually expect complexation of Ca^{2+} to enhance the dissolution of lime. Similarly, since complexation would increase with organic matter content it is

reasonable to expect increase dissolution of lime in the presence of organic matter. An increase in the level of carbonation (as indicated by the double endotherm around 700-800 ^{o}C) with organic matter content points to the presence of increasing amounts of dissolved Ca^{2+} (Fig. 10).

A second possible mechanism is the buffering of the pH by the organic matter. Acidic functional groups from the organic matter may buffer the pH, reducing the dissolution of silicate minerals and limiting the amount of silica available for CSH formation. This may explain why precipitation of CSH2, with its higher Ca: Si, was less affected by increasing organic matter content. Other possible mechanisms include; (i) the direct interaction of dissolved organic components with clays thereby reducing the surface area available for dissolution, and (ii) interaction of dissolved or undissolved organic matter with dissolved silica species thereby inhibiting nucleation and precipitation of CSH phases.

In addition to inhibitory effects on CSH formation and increase carbonation, organic matter may also influence the hydration characteristics of the clay. The absence of the endotherm attributable to interlayer water associated with hydration sphere of Ca^{2+} (approx. 160 ^{o}C), particularly in the 5% cHA GB samples, suggest that organic matter may influence lime-smectite reaction through alteration of the clay's interlayer (Fig. 10). This was supported by X-ray diffraction which showed a decrease in the interlayer spacing of the 5% cHA GB sample compared to the 0, 0.5 and 2% cHA samples (Appendix 1).

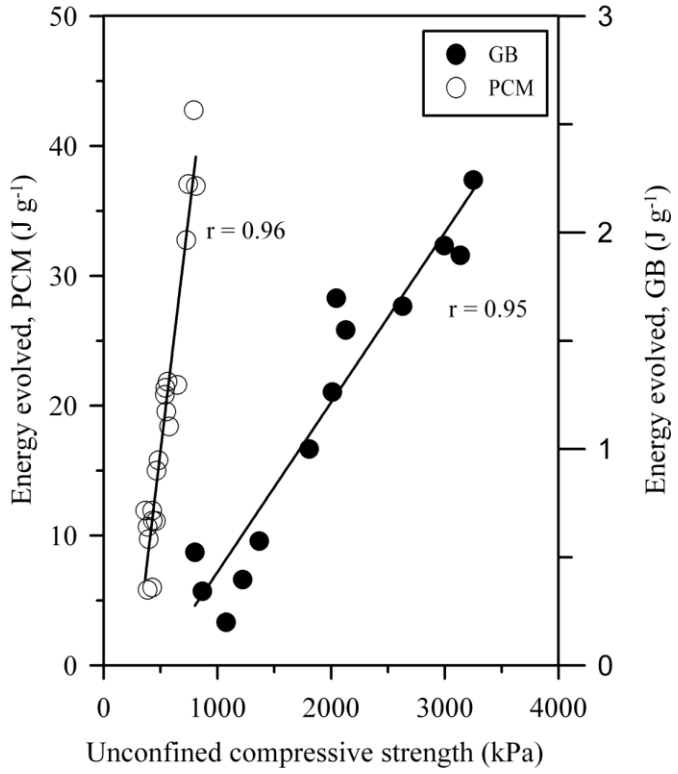

Fig. 12. Relationship between unconfined compressive strength of lime stabilized cores and integral heat of CSH re-crystallization.

3.3.3. Effect of natural organic matter source on calcium silicate hydrate formation

Increasing soil fulvic acid (sFA), soil humic acid (sHA), commercial humic acid (cHA) or lignite content all had an inhibitory effect on the formation of CSH in the lime stabilized paste (Fig. 13). In addition to varying with the amount of a given organic matter source, the degree of inhibition was also a function of the type of natural organic matter, the nature of the clay and subsequently the CSH phase formed. By assuming that; (i) maximum formation of CSH was achieved in the 0% organic matter samples, and (ii) the energy evolved during re-crystallization is directly proportional to the CSH formation, the change in CSH formation for a given source can be calculated as: ΔCSH_x

$= 1- (ECSH_{x,\,i} / ECSH_{x,\,0})$ where, Δ_{CSHx} represents the change in formation of CSH phase x (1 or 2); and $E_{CSHx,\,i} / E_{CSHx,0}$ is the ratio of the energy (J g^{-1})evolved during recrytallization of CSH1 or CSH2 in the presence of i amount of a given organic source to that evolved in the absence of that organic matter source $(E_{CSHx,0})$. In this study the value of i was 0.5, 2, or 5% of cHA. sFA, sHA or lignite. Energy of re-crystallization of CSH was determined by integration of heat flow thermograms shown in Fig. 13. Limits for integration were determined from the second derivative thermograms.

With the exception of lignite, which had similar effects on CSH1 and CSH2 formation, the effect of natural organic matter was greater on CSH1 formation than on CSH2 formation. For example, an addition of 2% sFA resulted in a 53% decrease in CSH2 formation compared to 100% loss in CSH1 formation (Fig. 14). For a given CSH phase the general order of influence of natural organic matter on its formation was cHA $\geq$ sFA > sHA > Lig. That lignite had the least negative impact on CSH formation could be attributed to its lower solubility, lower CEC and lower buffering capacity compared to cHA, sFA or sHA. In contrast to the humic and fulvic acids which would be soluble under the high pH conditions created by the addition of lime to a soil, lignite is insoluble due largely in part to its non-polar nature. Interactions involving soluble species from lignite are therefore unlikely. Similarly the absence of any significant cation exchange capacity or acidic characteristics makes complexation of Ca^{2+} or buffering unlikely mechanisms accounting for the changes in CSH formation due to increasing lignite content (Fig. 14). It is unclear what mechanisms are operational in the lignite samples.

The larger effect of sFA on CSH formation compared to sHA is attributable to the greater acidic/CEC character of fulvic acids compared to humic acids.

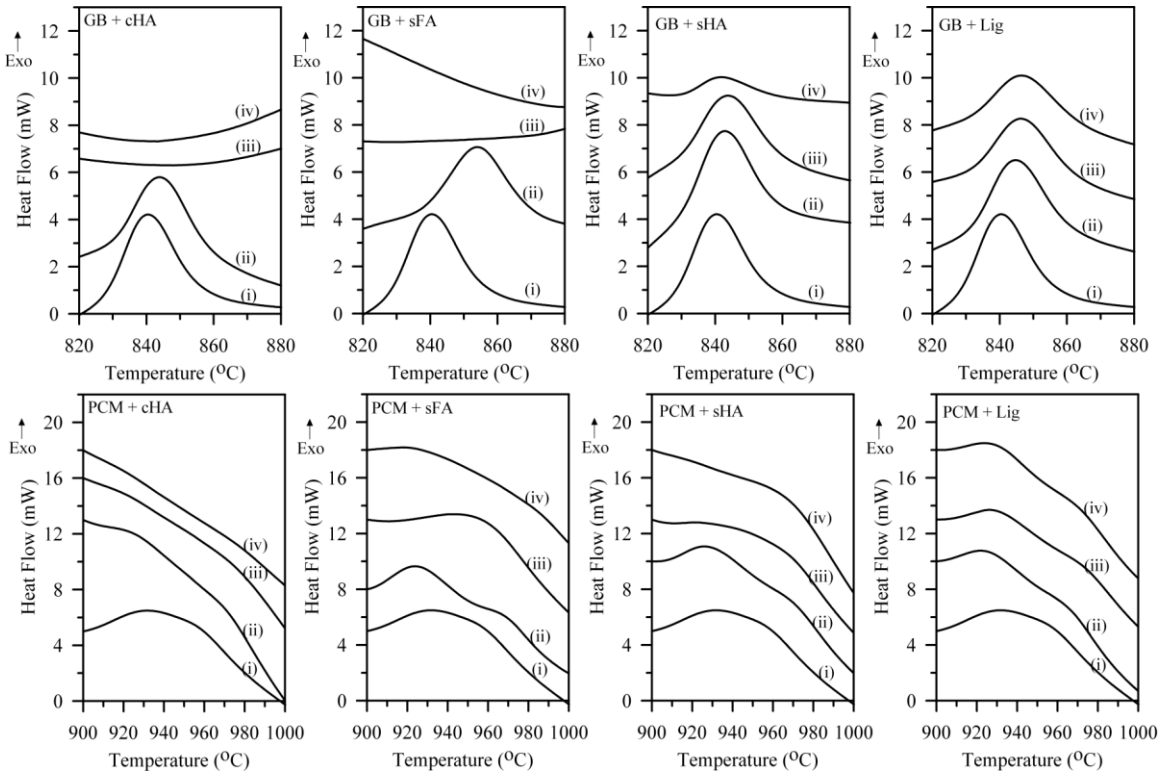

Fig. 13. Intensity of DSC peaks attributable to CSH formation in GB (8% lime) and PCM (12% lime) pastes containing (i) 0, (ii) 0.5, (iii) 2 or (iv) 5% natural organic matter as commercial humic acid (cHA), soil fulvic acid (sFA), soil humic acid (sHA) and lignite (Lig). Samples were incubated at 100% humidity and 23 °C for 28 day

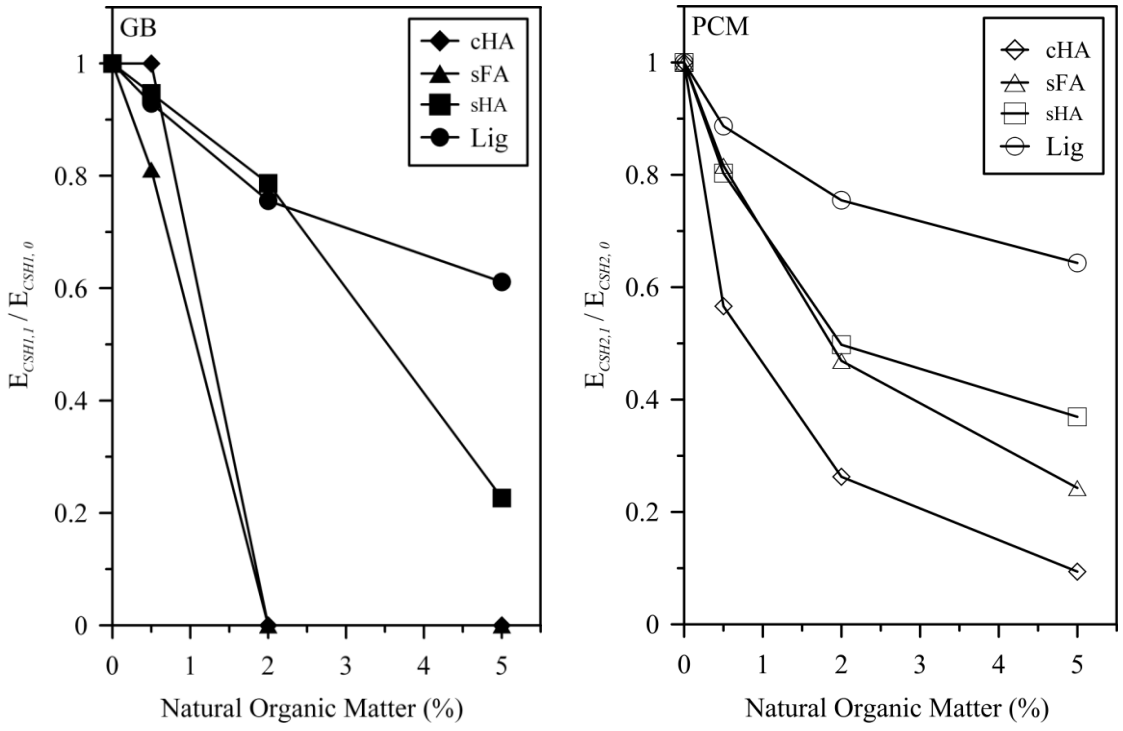

Fig. 14. Change in calcium silicate hydrate formation with natural organic matter content in GB and PCM pastes. Values are based on the integral heats of CSH re-crystallization in organic matter containing samples ($E_{CSH,\ i=0.5,\ 2\ or\ 5\%}$) compared to organic-free samples ($E_{CSH,\ 0}$). Natural organic matter was present as commercial humic acid (cHA), soil fulvic acid (sFA), soil humic acid (sHA) and lignite (Lig).

3.4. Summary and conclusions

Thermal analysis was used to investigate the influence of natural organic matter on calcium silicate hydrate formation in two model soils containing clays of different mineralogies (a Gonzales bentonite and a Panther Creek montmorillonite) in an effort to understand the mechanism of organic matter control on CSH formation in lime-stabilized soils. In the absence of organic matter, the quantity and type of CSH phase formed in a given soil was found to depend on the nature of the clay and the amount of lime added. Formation of CSH1 was favored in the Gonzales bentonite at 3- 8% lime,

while CSH2 was favored at higher lime contents and in the Panther Creek montmorillonite. The organic matter used in this research was found to inhibit both CSH1 and CSH2 formation in lime stabilized soils. The degree of inhibition was a function of the amount and type of organic matter, as well as the CSH phase. Increasing organic matter content increased the inhibition of CSH formation. For the organic matter sources studied a general order of cHA ≥ sFA > sHA > Lig can be described. Humic and fulvic acids had a greater inhibitory effect on CSH1 than CSH2 while lignite had the similar effects on both CSH phase.

In addition to pointing to the inhibition of CSH formation as a primary mode of action of organic matter influence on pozzolanic activity in the lime stabilized soils, the results of this research has significant implications for lime stabilization of soils. Paramount to any discussion on the topic is the recognition that mitigation of organic soils using lime as stabilizer is a multi-variate problem. Significant consideration must be given to soil and environmental characteristics including (but not limited to) the nature of the soil minerals, amount and characteristics of the organic matter present and the type of pozzolanic product likely to be formed.

CHAPTER IV

TEMPERATURE-DEPENDENT TRANSFORMATIONS IN PLANT-DERIVED BIOCHARS: IMPLICATIONS FOR CATION EXCHANGE CHARACTERISTICS AND CADMIUM SORPTION AS DETERMINED BY FLOW ADSORPTION CALORIMETRY

4.1. Introduction

Plant-derived biochars are carbon-rich solid residues formed from incomplete combustion of plant biomass. Global estimates of plant-derived biochars production from vegetation fires are on the order of 0.004 – 0.3 Gt C y^{-1} [34, 147]. Twenty to fifty percent of the feedstock used in the thermal conversion of plant biomass to biofuel is converted to biochar [148-152]. Despite indications of susceptibility to oxidative and microbial degradation [91, 153-155]; plant-derived biochars have slow rate of turnover in the environment [34, 35, 156]; and accumulate in fire-impacted soils, where they can account for up to 80% of the soil organic carbon [35, 63, 157, 158]. Understanding the physicochemical characteristics of plant-derived biochars and their impact on different biogeochemical cycles is of great ecological and environmental importance.

Physicochemically, plant-derived biochars are heterogenous mixtures of thermally altered biomacromolecules [87, 88]. Two major factors influencing the degree of thermal alteration in plant-derived biochars are temperature and plant material chemistry [34, 49, 88, 91, 99, 159]. For a given formation temperature, biochars derived from carbohydrate plant materials are more thermally altered than those derived from

nitrogenous materials [88]. For a given plant material, thermal alteration increases with formation temperature [34, 91, 159].

Variability in thermal alteration yield plant-derived biochars with significantly different bulk and surface characteristics [74, 80, 81, 91, 95, 160]. In general, increasing thermal alteration; increases polyaromatic characteristics, porosity and surface area; but decreases polar characteristics of the biochars. The influence of such changes on the sorption of nonpolar and nonionic polar organic adsorbates to plant-derived biochar have been systematically elucidated [80, 81, 95, 96, 104, 160]. For instance, Chen et al.[81] found that the transitional behavior (polarity-selective => porosity selective => non-selective) observed for naphthalene, nitrobenzene and *m*-nitrobenzene sorption onto pine-needle biochars were due to changes in biochar aromaticity, porosity and surface area; as a function of temperature. Recent studies have shown that plant-derived biochars also have the ability to sorb environmentally significant ionic species, such as heavy metals [79, 83, 102]. However, a systematic understanding of how changes in the surface or bulk properties of the biochar influences biochar-metal interactions is needed.

The reality is that research on the sorption of ionic species, such as heavy metals, to plant-derived biochars is still in its infancy [102]. In contrast, sorption of heavy metals onto other carbon-rich materials such as humic materials, activated carbon and carbon nanotubes have been widely studied [100, 161-174]. Although the physicochemical properties of these other carbon-rich materials may differ significantly from plant-derived biochars, they may provide useful insights on sorption involving plant-derived biochars. For example, studies on heavy metal sorption to humic materials, activated

carbon and carbon nanotubes all indicate that functional group chemistry of the carbon-rich material and solution chemistry are the primary factors driving sorption. It is widely accepted that oxygenated functional groups are the primary sites for heavy metal sorption on these materials [169, 172-178].

Both elemental and molecular level data indicate that the surfaces of plant-derived biochars are comprised of numerous oxygenated moieties (e.g. –OH, -COOH, -O-, =O, and –CHO) [34, 49, 81, 88, 91, 99]. Therefore, it would be reasonable to assume that oxygenated functional groups on the surfaces of the plant-derived biochars are the primary sites of heavy metal sorption. We postulated that the sorption of ionic species, such as heavy metals to plant-derived biochars is controlled by both the type and distribution of oxygenated functional groups on surface of the biochar.

A systematic study to evaluate the influence of combustion temperature and plant material chemistry on the surface and metal sorption properties of plant-derived biochars was conducted. Functional group chemistry of the plant-derived biochars was investigated using diffuse reflectance infrared fourier transform spectroscopy (DRIFTS), and flow adsorption micro-calorimetry (FAMC) was used to study metal sorption characteristics on the plant-derived biochars. The use of infrared spectroscopy to study functional group chemistry of carbon-rich materials is well established [96-98, 179-183]. Using flow adsorption micro-calorimetry to study adsorption/desorption processes has several advantages over traditional batch sorption techniques. For example, FAMC; is not subject to well known limitations associated with the use of batch sorption techniques [184-189]; is more sensitive to changes occurring at the liquid/solid interface

than batch adsorption isotherms [190, 191]; allows for the direct measurement of heats of reaction and simultaneous collection of heat and sorption data at temporal resolutions on the order of seconds [192-195]; can be used to resolve complex reactions occurring more or less simultaneously but at different rates [196]. With FAMC, multiple adsorption/desorption cycles can be performed on a single sample, thereby allowing for the easy differentiation of reversible/irreversible processes [192, 193, 196].

Specific objectives of the study were: (i) to assess changes in functional group chemistry of plant-derived biochars, as a function of formation temperature and plant species; and (ii) to elucidate and compare sorptive characteristics of a simple cation (K^+) and a heavy metal (Cd^{2+}) on plant-derived biochars formed under different temperature conditions.

4.2. Materials and methods

4.2.1. Plant-derived biochars and biochar preparation

Biochars used in this study represented a range of combustion temperatures (200- 650 ^oC) and three plant species [49]. The three species represented were honey mesquite (*Prosopis glandulosa* Torr.), cordgrass (*Spartina spartinae*) and loblolly pine (*Pinus taeda)*, referred to as HM, CG and PI, respectively. Taxonomically the plant materials can be further divided into angiosperms (HM, CG) versus gymnosperm (PI); woody (HM, PI) versus non-woody (CG); C_3 (HM, PI) versus C_4 (CG); and legumes (HM) versus non-legumes (CG, PI). Biochars were prepared at increments of 50 ^oC from 200 to 650 ^oC, according to procedures outlined by Kuo et al. [49]. In brief, prior to charring samples of the different plant materials were dried in an oven at 60 ^oC for 3d.

The dried plant material were then placed in quartz crucibles and charred at the desired temperatures in a muffle furnace for 1h, under oxygen-limited conditions. After charring, the newly formed biochars were allowed to cool overnight, grounded to pass through a 60 mesh (250 μm) sieve and stored in glass vials. Unless otherwise specified, biochars were used without any further processing.

4.2.2. Chemical composition of biochars

Elemental composition (CHNO) of the plant-derived biochars were determined by Kuo et al. [49]. Molecular composition/ functional group chemistry of the biochars was further evaluated using diffuse reflectance infra-red fourier transform spectroscopy (DRIFTS). For DRIFTS analysis, spectra of each biochar sample were collected in the OH-stretching (3700-3100 cm^{-1}), CH-stretching (3100- 2700 cm^{-1}) and the finger-print (1900-700 cm^{-1}) regions using a Magna-IR 560 spectrometer (Thermo-Nicolet, Madison, WI) equipped with a Gemini HATR/diffuse reflectance sampling head (Spectra Tech, Shelton, CT). Each spectrum was collected at a resolution of 16 cm^{-1} and was based on 500 co-added scans. Second derivative analysis (Savitzy-Golay method [197]) and peak deconvolution (assuming gaussian peak shape) were performed on each spectra to determine peak positions and peak intensities, respectively. Prior to second derivative analysis and peak deconvolution spectra were subjected to smoothing (Savitzy-Golay method [197]) and baseline correction (assuming linear baseline) in the respective analysis window (OH-stretch, CH-stretch and finger-print). All spectral processing was performed using the Omnic software (version 8.0, Thermo Fisher Scientific Inc., MA, USA).

4.2.3. Flow adsorption micro-calorimetry experiments

4.2.3.1. The flow adsorption micro-calorimeter

The calorimeter used was a dual-mode, variable-gain flow adsorption micro-calorimeter that was designed and built in-house specifically for studying reactions occurring at the solid/liquid interface of granular sorbents (Fig. 15). A similar design was used in earlier publications to study sorption characteristics of different contaminants on soils and synthetic metal oxides [192-195] . The calorimeter can be operated in both injection and flow-through modes with signal amplifications of ×1000, ×2000, ×5000, or ×10000.

The sensing unit of the calorimeter (Fig. 15) was thermistor-based and consisted of: (i) a reference thermistor (Thermistor 1), which senses the temperature of the incoming solution; (ii) a calibrating resistor, for calibrating heat signal to known heat input; (iii) a column, containing the sorbent; and (iv) a column thermistor (Thermistor 2), which senses the temperature of the effluent. The difference in temperature between Thermistor 1 and 2 is the calorimetric output (heat signal) and is amplified and recorded as a voltage output over time (usually 5s intervals), with a return to baseline (or zero difference) considered to be the end of the reaction.

The heat signal may be a flat line (zero difference), exothermic or endothermic and is attributed to interactions between the sorbate and the sorbent. A flat line prior and after an exotherm or endotherm is indicative of a baseline before and after a reaction, respectively. The absence of an exotherm or endotherm is indicative of no sorption. In addition to being indicative of whether a reaction is endothermic or exothermic, when

combined with heat calibration data and differences between initial sorbate and effluent concentrations, the heat signal can be used to directly determine molar heats of reaction. Differences in molar heats of reaction for different sorbates with the same sorbent are indicative of differences in the bonding strength of each sorbate with the sorbent of interest. Larger molar heats of reaction, in this case molar heat of adsorption, are indicative of stronger bond formation and are useful in deciphering between physical sorption and actual bond-forming sorption mechanisms. Differences in reaction kinetics at a given flow rate or at variable flow rates may also be elucidated qualitatively (by comparing the shape of heat signal) or quantitatively (by calculating the rate at which heat is released or adsorbed).

4.2.3.2. Cation exchange and cadmium sorption characteristics on plant-derived biochars

Flow adsorption micro-calorimetry was used to elucidate surface charge, cation exchange and cadmium sorption characteristics on honey mesquite (HM) , loblolly pine (PI) and cordgrass (CG) biochars formed at 200, 300, 350, 550 and 650 ^{o}C. The selected biochars represented 3 low temperature (200, 300, 350 ^{o}C) and 1 high temperature (550 ^{o}C for CG; 650 ^{o}C for HM and PI) biochar from each plant species. All experiments were carried out with the calorimeter in the flow-through mode of operation; a solution flow rate of 0.30- 0.35 mL min^{-1}; signal amplification of ×5000; an ionic strength of 10 mM; and using 50- 60 mg of biochar. Before using, biochar samples were hydrated in 10 mM NaCl (no pH adjustment) for at least 5 days. After hydration, the samples were packed into the calorimeter micro-column as slurries. Glass fiber wool was placed at

both ends of the micro-column to hold the biochar in place. After packing, the sample was flushed with 10 mM NaCl (pH 9.0±0.1 for cation exchange; pH 5.0±0.1 for cadmium sorption experiments) for 3-5 h until a stable baseline (indicating thermal equilibrium of the system) was obtained.

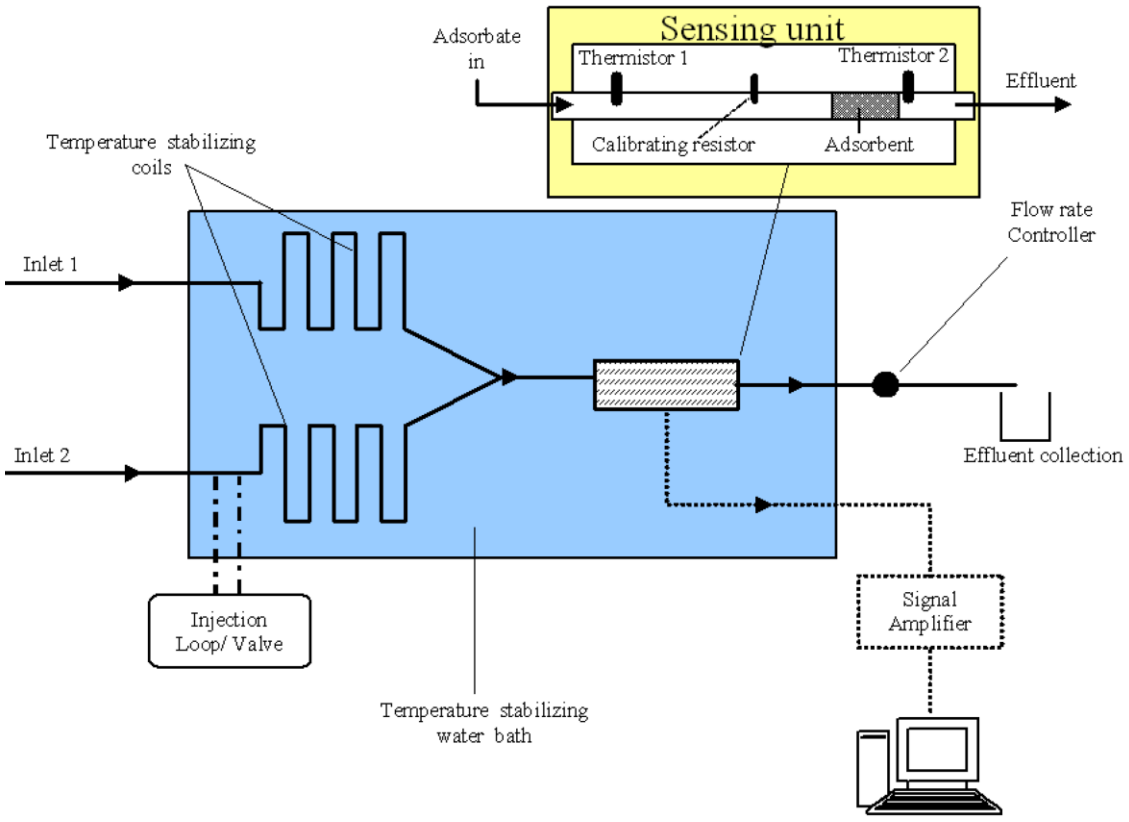

Fig. 15. Schematic of dual-mode variable-gain flow adsorption micro-calorimeter.

Surface charge and cation exchange characteristics of the plant-derived biochars were evaluated using, K^+ (10 mM KCl) and Na^+ (10 mM NaCl) at pH 9.0±0.1, 7.0±0.1, 5.0±0.1 and 3.0±0.1 (order of treatment) as probe cations. Desired solution pH was

obtained through the dropwise addition of 1N HCl or 1M KOH (for KCl) and 1M NaOH (for NaCl) to unadjusted solutions. At each pH studied, following the attainment of thermal equilibrium in NaCl (also indicative of available cation exchange sites on the biochar being saturated by Na^+), heat signals for 2- 3 cation treatment cycles were collected. A cation exchange treatment cycle consisted of one K^+/Na^+ (K^+ replacing Na^+) treatment followed by a Na^+/K^+ (Na^+ replacing K^+) treatment. In a K^+/Na^+ treatment, 10 mM KCl (at the desired pH) was allowed to flow through the Na^+-saturated biochar column at 0.30– 0.35 ml min^{-1} until the heat signal returned to baseline; indicative of the attainment of thermal equilibrium in KCl. Here, thermal equilibrium in KCl also indicated complete replacement of the previously adsorbed Na^+ on cation exchange sites of the biochar by K^+ thereby resulting a K^+-saturated biochar. For the accompanying Na^+/K^+ treatments, solution flow rate and pH conditions were similar to that for K^+/Na^+ treatments however, instead of KCl, 10mM NaCl was allowed to flow through the K^+-saturated biochar. A return to baseline of the heat signal, during the Na^+/K^+ treatment, was indicative of thermal equilibrium in NaCl and the complete replacement of K^+ on available cation exchange sites of the biochar by Na^+.

Following the last K^+/ Na^+ treatment at pH 3±0.1 , the micro-column was removed from the calorimeter, flushed with 5 ml (~20 pore volumes) of nanopure water (Diamond UV ultra-pure water system, Branstead International, Iowa, USA) to remove any entrained K^+ from the biochar and used for quantitative K^+ adsorption experiments. In the quantitative K^+ adsorption experiments, 20 mL of 10 mM NaCl (pH 3±0.1; flow rate = 0.15 – 0.20 ml min^{-1}) was passed through the micro-column to desorb the

adsorbed K^+ from the biochar. The adsorption and desorption of K^+ was then repeated using 40 ml of the 10 mM KCl (flow rate = 0.30 – 0.35 ml min^{-1}), for the K^+ adsorption cycle, and 20 ml of the 10 mM NaCl at 0.15- 0.2 ml min-1, for the K^+ desorption cycle. The leachate was collected during the desorption cycle and analyzed for K^+ by ion chromatography (Nutrient and Water Analysis Lab., Texas A & M University). Duplicate runs of K^+ adsorption and desorption were performed at pH 3±0.1, pH 5±0.1, pH 7±0.1 and pH 9±0.1 respectively. Here we were interested in quantifying the number of available cation exchange site and the charge density with solution pH, biochar formation temperature and plant species. To facilitate calculation of charge density, total specific surface area of the biochars were also determined by single point N_2 Brunauer-Emmet-Teller (N_2-BET; p/p_o = 0.30) analysis using a Quantasorb Jr. surface area analyzer (Quantachrome Instruments, Boynton Beach, FL). Potassium adsorption data were also combined with K^+/Na^+ heat signal data to determine the molar heats of K^+ adsorption onto the biochars.

For cadmium sorption experiments, biochar hydration and column packing procedures were the same as described earlier. However, the initial flushing and equilibrium conditions were established at pH 5±0.1 (10 mM NaCl) rather than at pH 9±0.1. After obtaining a stable baseline in the NaCl, a single treatment cycle of Cd^{2+} (5 mM $CdCl_2$; pH 5±0.1; 0.3- 0.35 ml min^{-1}) was done. Following cadmium treatment the column was removed from the calorimeter, flushed with 5 mL nanopure water (to remove entrained Cd^{2+}), and dried at 75 ^oC for 24 h. After drying, the sample was weighed and the biochar ashed (600 ^oC for 8 h). The ash was then digested in HCl (110

^{o}C for 1h) and analyzed for Cd^{2+} using ICP (Soil, Water and Forage Testing Lab., Texas A & M University). Untreated samples were also ashed, digested and analyzed for background Cd^{2+}. Background concentrations of Cd^{2+} in the untreated biochar samples were all below the method detection limit (3.62×10^{-4} mg L^{-1}).

4.3. Results and discussion

4.3.1. Temperature-dependent transformations in plant-derived biochars

4.3.1.1. Transformations in biochars inferred from elemental analysis

Elemental (CHNO) and biomacromolecule (hemicellulose, cellulose and lignin) composition of the uncharred plant materials and biochars are shown in Table 5. Atomic ratios indicate that while N distribution varied with plant species (one N atom every 200 C atoms for PI; one N every 100 C atoms for CG and one N atom every 50 C atoms for HM biochars) it was largely unaffected by biochar formation temperature. The relatively high distribution of N in the HM biochars, compared to CG and PI biochars was due to the fact that honey mesquite is leguminous and has the ability to incorporate nitrogen into its structure via nitrogen-fixation [198-200] . The apparent persistence of nitrogen during the charring process have been reported by other researchers [87-90, 201] and has been attributed to: (i) the formation of thermally-stable heterocyclic and heteraromatic N structures (e.g. sugar-amino acid products formed via Maillard-type reactions), and (ii) steric hindrances (e.g. in organic domains where the transfer of energy and thermal degradation is comparatively impeded with respect to external areas).

Table 5
Biomacromolecule and elemental composition of plant-derived biochars.

	Biomacromolecule			Elemental composition				Elemental ratio				
	Hemicellulose	Cellulose	Lignin	N	C	H	O	N/C	H/C	O/C	Weight loss	Ash
	%			%							%	%
Loblolly pine												
PI raw	10.4	56.4	15.0	0.19	45.9	6.5	46.1	0.004	1.70	0.753	0	1.34
PI200				0.27	51.8	6.2	39.6	0.004	1.44	0.573	6.28	2.06
PI250				0.29	55.7	5.8	36.3	0.004	1.25	0.489	16.9	1.86
PI300				0.30	63.8	5.2	28.3	0.004	0.98	0.333	39.1	2.35
PI350				0.40	68.3	4.3	23.6	0.005	0.76	0.259	55.7	3.42
PI400				0.39	71.4			0.005			64.1	4.10
PI450				0.43	73.3			0.005			68.3	6.40
PI500												
PI550												
PI600												
PI650				0.26	83.8			0.003			73.3	5.50
Honey mesquite												
HM raw	11.5	54.1	11.5	1.39	44.7	6.3	42.1	0.027	1.69	0.706	0	5.51
HM200				1.29	47.2	6.0	39.3	0.023	1.53	0.624	8.75	6.14
HM250				1.51	52.3	5.7	33.7	0.025	1.31	0.483	23.7	6.85
HM300				1.60	62.1	4.7	22.2	0.022	0.91	0.268	46.1	9.44
HM350				1.70	63.5	4.2	20.6	0.023	0.79	0.243	54.6	10.0
HM400				1.68	64.6	3.5	18.6	0.022	0.65	0.216	61.7	11.7
HM450				1.55	68.1	3.2	18.2	0.020	0.56	0.200	65.5	13.4
HM500												
HM550												
HM600												
HM650				1.47	72.6	1.8	8.5	0.017	0.30	0.088	71.6	15.6
Cord grass												
CGraw	31.7	41.7	4.2	0.46	41.0	6.4	43.3	0.010	1.87	0.792	0	8.79
CG200				0.54	46.2	5.8	36.9	0.010	1.51	0.599	17.7	10.6
CG250				0.57	49.3	5.4	32.4	0.010	1.31	0.493	29.6	12.4
CG300				0.71	56.1	4.2	22.0	0.011	0.90	0.294	50.1	17.1
CG350				0.77	55.2	3.5	20.3	0.012	0.76	0.276	57	20.2
CG400				0.75	55.1	3.1	18.2	0.012	0.68	0.248	63.7	23.0
CG450												
CG500												
CG550				0.66	54.1	2.2	12.8	0.010	0.49	0.177	72.2	30.3
CG600												

In contrast to N, the distribution of O and H in the biochars varied with formation temperature; but was similar at a given formation temperature, irrespective of plant species (Fig. 16). Oxygen and hydrogen distribution in the uncharred plant materials were approx. one O and 2 H every C (consistent with a typical monosaccharide sub-

unit). In biochars formed at 650 ^{o}C, the O and H distribution were an order of magnitude lower than the uncharred plant materials, with approx. one O every 10 C and 1 H every 3 carbon. This indicated that, relative to N, O and H were preferentially lost with increasing biochar formation temperature. Inflection points in Fig. 16 indicated that: (i) the rate of change in O and H distribution were different for the biochars formed at temperatures above and below, 200 ^{o}C and 300 ^{o}C; and (ii) rate of change in O and H distribution in the biochars occurs more or less simultaneously. For the temperature range studied, O distribution decreased at an average rate of: 9.0×10^{-4} atoms $\cdot$ $^{o}C^{-1}$, between 25^{o}C and 200 ^{o}C; 3.0×10^{-3} atoms $\cdot$ $^{o}C^{-1}$ between 200 and 300 ^{o}C; and 6.0×10^{-4} atoms $\cdot$ $^{o}C^{-1}$ between 300 and 650 ^{o}C. For the same temperature ranges, the rates of H loss were 1.7, 1.9 and 2.8 times that of O, respectively. Similar inflection points were observed in weight loss data, up to biochar formation temperatures around 500 ^{o}C (Fig. 17), suggesting that weight loss during the charring process (at least up to 500 ^{o}C) was closely associated with changes in O and H content.

Ratios of H: O loss of approx. 2 was consistent with loss of water, and suggested that dehydration was a major mechanism responsible for thermal transformations in the plant-derived biochars [49, 91, 201, 202]. Up to 200 ^{o}C, dehydration was attributable to the loss of physically adsorbed water. At higher temperatures, dehydration was attributable to the loss of "chemical" water associated with the thermal degradation of hemicelluloses, cellulose and lignin [203].

Hydrogen: oxygen losses lower than 2 (as observed in biochars formed at temperatures $\leq$300 ^{o}C), pointed to the involvement of simultaneous

dehydration/deoxygenating mechanisms during the thermal transformation of the biochars. Such mechanisms would include the cracking of oxygen-containing functional groups during the thermal degradation of hemicellulose and cellulose in the plant tissues. Yang et al. [204] found that the thermal degradation of hemicellulose was accompanied by the release of CO_2 and CO with maximum release of both gases occurring around 280 ^oC. They attributed the release of CO_2 from hemicellulose to the cracking and abscission of C-C and C-O connected to the main hemicellulose branch. The release of CO was attributed the cracking of ether (C-O-C) and carbonyl (C=O) functional groups.

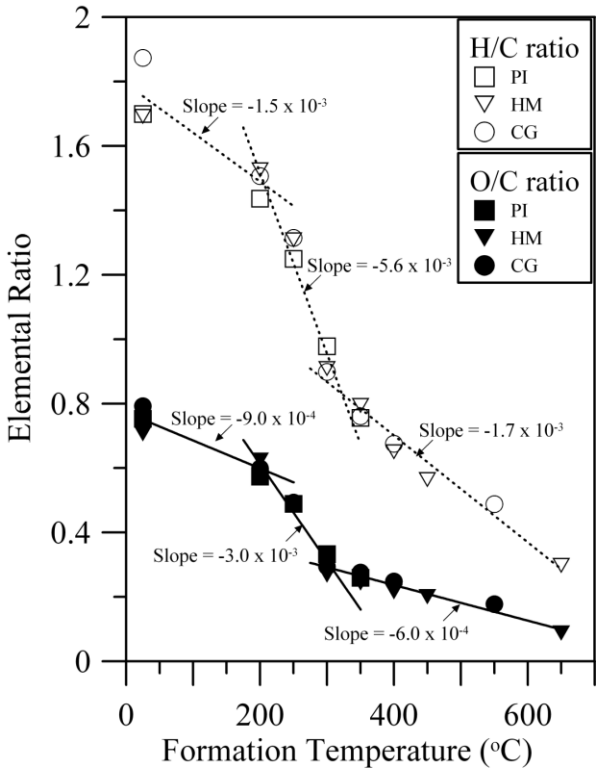

Fig. 16. H/C (open symbols) and O/C (closed symbols) ratio for loblolly pine (PI), honey mesquite (HM), and cord grass (CG) biochars.

Hydrogen: oxygen losses greater than 2 (observed at biochar formation temperatures ≥300) suggested that in addition to dehydration, dehydrogenation mechanisms were also important to the thermal transformation of the biochars. Possible dehydrogenation mechanisms operational during the formation of the biochars would include demethylation ($-CH_3$), demethylenation ($-CH_2$), demethoxylation ($-OCH_3$) and aromatization. The increase in H: O loss (1.7 at $T \leq 200\ ^oC$; 1.9 at $200\ ^oC < T \leq 300\ ^oC$; 2.8 at $T > 300\ ^oC$), indicated that the significance of dehydrogenation mechanisms in biochar transformation increases with biochar formation temperature. This would be consistent with observations of increased aromatization with biochar formation temperature [34, 159]. Data from gas evolution studies on the thermal degradation of plant biomacromolecules also points to the increase significance of dehydrogenation mechanisms at higher temperatures. For example, Yang et. [204] found that - during the thermal degradation of hemicellulose, cellulose and lignin - H_2 was evolved at temperatures >400 and increased at higher temperatures.

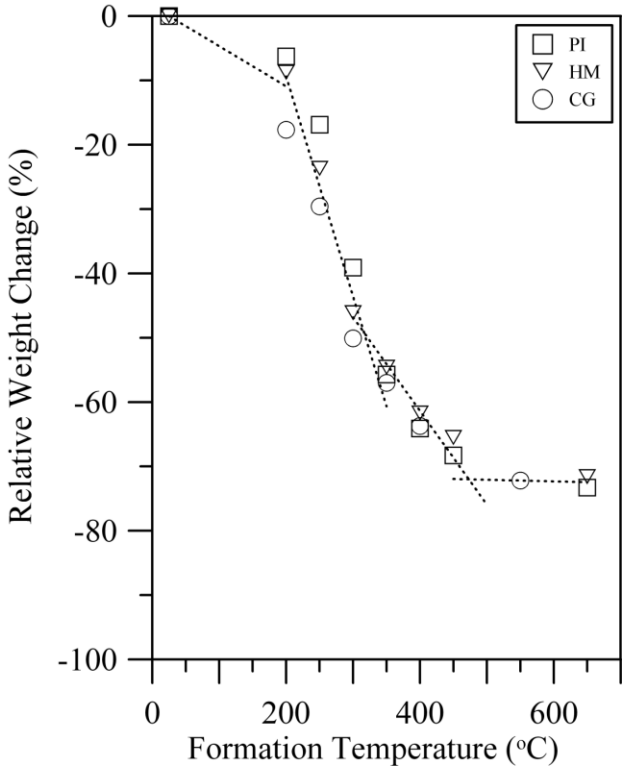

Fig. 17. Weight loss during formation of loblolly pine (PI), honey mesquite (HM) and cord grass (CG) biochars.

4.3.1.2. Transformations inferred from infrared spectroscopy

Infrared (IR) spectra in the OH-stretch region for the plant-derived biochars are shown in Fig. 18. Here, changes in spectral behavior with biochar formation temperature are largely attributable to temperature induced changes in the inter- and intra-molecular hydrogen bonding (including hydration) characteristics of the lignin, cellulose and hemicellulose biomacromolecules comprising the plant materials [205]. Based on second derivative analysis of the infrared spectra (Fig. 18), 3 (in the case of CG) and 4 (in the case of HM and PI) dominant peaks were identifiable in the OH stretch region for biochars formed at 200 ^{o}C; one around 3285 cm^{-1}, one around 3350 cm^{-1}, one around

3435-3450 cm^{-1} and one around 3530 cm^{-1} (observable only in the wood biochars). These peaks were attributable to inter-chain hydrogen bonds that have been re-arranged or weakened during the early stages of the charring process [205-208]. Peaks around 3285 and 3350 cm^{-1} were consistent with peak positions reported for weakened O2 – H2···O6 (H-bonding between OH at C2 position of one glucosidic ring and O at the C6 position of an adjacent ring) and O3 – H3···O5 (H-bonding between OH at C3 position of one glucosidic ring and the O at the C5 position of another) H-bonds in cellulose, respectively [205]. Similarly, the peak around 3435-3450 cm^{-1} and that around 3530 cm^{-1} was consistent with that reported for OH groups that are involved only in weak or no hydrogen bonding, respectively [205, 206]. Coupling of H: O atomic ratios with infra-red spectroscopy data suggests that the major mechanisms accounting for transformations in the biochars produced at 200 ^{o}C, were dehydration and hydrogen bond weakening.

For plant-derived biochars produced at temperatures greater than 200 ^{o}C, the intensity of the OH-stretch peaks (identifiable in the biochars formed at 200 ^{o}C), generally decreased with increasing biochar formation temperature (Fig. 18). Consistent with changes in H: O atomic ratio, the largest changes in OH peak intensity were observed in biochars formed between 200 and 300 ^{o}C. Peaks attributable to weakly H-bonded hydroxyls (~3450 cm^{-1}), as well as weakened O3 – H3···O5 (~3350 cm^{-1}) and O2 – H2···O6 (~3285 cm^{-1}) inter-chain H-bonds showed the greatest change in peak intensity with losses of 63-82%, 62-67% and 74-100%, respectively. The O2 – H2···O6 peak was absent from the spectra of biochars formed at temperatures above 300 ^{o}C. Such decrease

in the intensity of the OH stretch peaks between 200 and 300 ^{o}C was consistent with further weakening and the breaking of inter-chain hydrogen bonds, as well as dehydroxylation - due to thermal degradation/transformation of hemicellulose and cellulose - during biochar formation.

That thermal degradation of cellulose was a major mechanism responsible for differences between biochars produced at 200 and 300 ^{o}C is also supported by X-ray diffraction analysis of the biochars. No peaks attributable to cellulose were present in x-ray diffractograms of biochars formed at temperatures greater than 250 ^{o}C (Appendix 4).

Dehydration in biochars produced between 200 to 300 ^{o}C, as implied from H: O losses, suggested the involvement of a simultaneous dehydrogenation-dehydroxylation process. This would be consistent with intra- and inter-ring dehydration, hydroxyl radical H-abstraction, as well as furan formation mechanisms which has been used to explain the loss of "chemical" water from hydrolyzable biomacromolecules, during their thermal degradation [203].

For biochars formed at temperatures ≥ 300 ^{o}C, two new peaks were observable; one around 3630 cm^{-1} and the other around 3230 cm^{-1}. These peaks were attributable to free OH (hydroxyls not involved in intermolecular hydrogen bonding) and hydroxyls from carboxylic groups, respectively [209]. Intensities of both these peaks increased and decreased simultaneously, with maxima occurring in biochars formed at temperatures between 300 and 400 ^{o}C (Fig. 18 inset).

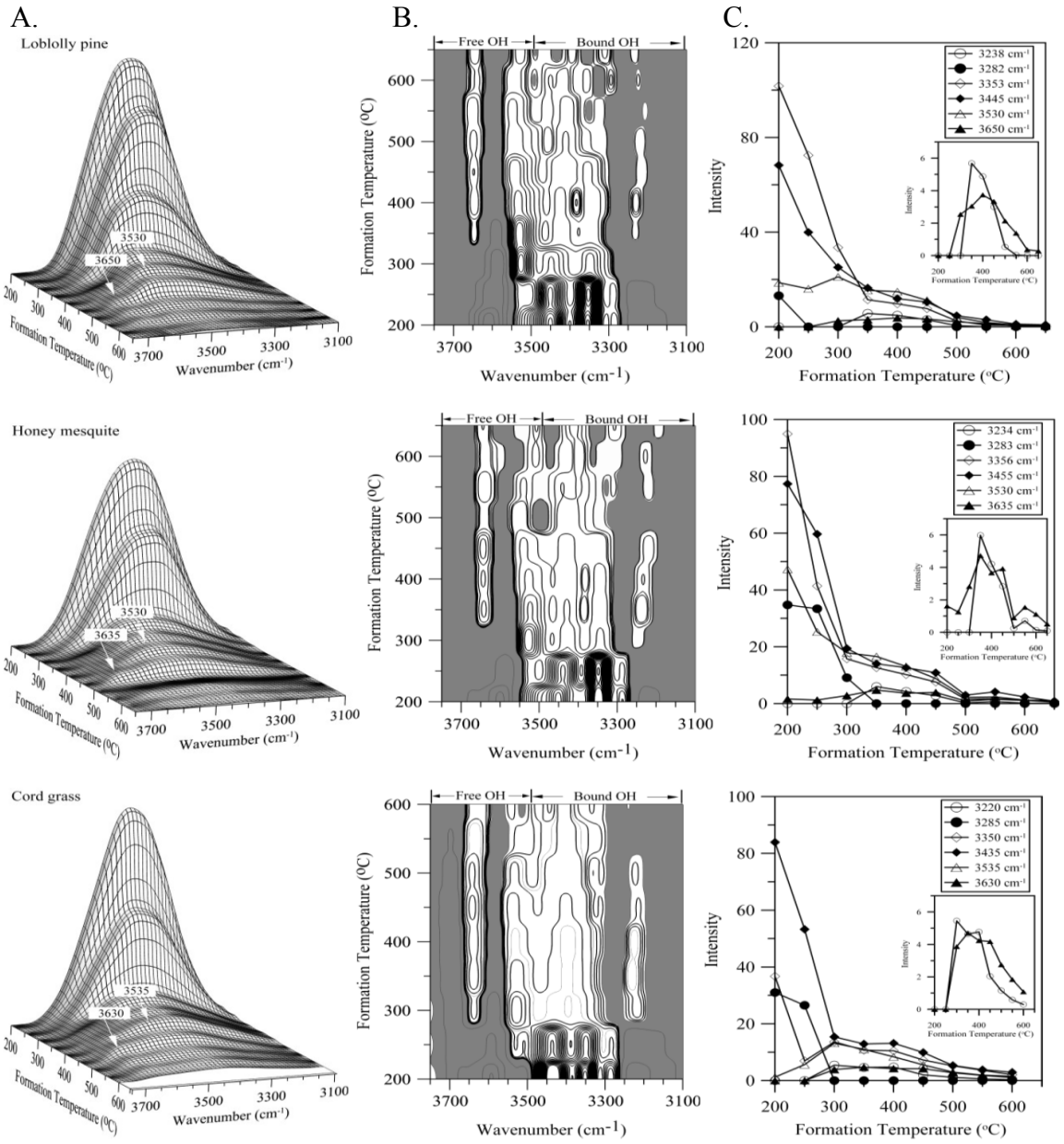

Fig. 18. Infrared spectroscopy analysis in the OH-stretch range for plant-derived formed at temperatures between 200 and 650 °C. (A) 3D representation of the IR spectra; (B) second derivative analysis (white- negative, gray- positive); (C) peak intensity.

The simultaneous increase in the concentration of free OH and carboxylic functional groups on the surface of the biochars suggested that the same process or

coupled processes are responsible for molecular transformations in biochars formed at temperatures between 300 and 400 ^{o}C. Oxidation, depolymerization/fragmentation reactions during the thermal degradation of hemicellulose, cellulose and lignin are known to yield various carboxylic and hydroxylated decomposition products [203, 210]. Therefore, it would be reasonable to assume that these processes are responsible for the increase in concentration of the carboxylic and free OH groups on the surface of the biochars formed at temperatures between 300 and 400 ^{o}C. The decrease in the concentration of both the carboxylic and free OH at biochar formation temperatures >450 ^{o}C, highlights the instability of these groups at higher temperatures.

Spectral data obtained for the plant-derived biochars in the CH-stretch (3100-2700 cm^{-1}) region of the infra-red spectrum are shown in Fig. 19. Alkyl/aliphatic CH (C-CH_n) show adsorption peaks in the 2700- 3000 cm^{-1} range, while alkenes and aromatic CH (C=CH) show absorbs in the 3000- 3100 cm^{-1} range [204, 209]. Two peaks were observable in the aliphatic CH range for biochars produced at 200 ^{o}C, irrespective of plant species. These peaks, observed at 2930 and 2860 cm^{-1}, were attributable to asymmetric methylene (-CH_2) and asymmetric methyl (-CH_3) groups, respectively [209]. Methylene groups are common features of hemicelluloses and cellulose, while methyl groups are likely associated with lignin and hemicellulose – in plant tissues [204]. Methyl groups in lignin and hemicelluloses may also exist as methoxyl (-OCH_3).

Decreasing peak intensity (Fig. 19) indicated that methylene and methyl concentration in plant-derived biochars decreased with increasing formation temperature. Concentrations of methylene and methyl groups in biochars formed at 200

^{o}C were 2- 3, 4- 6 and 9- 14 times that of biochars formed at 300, 350, 400 ^{o}C, respectively. For biochars formed at 500 ^{o}C, the concentration of methylene and methyl groups were <1% of that for biochars formed at 200 ^{o}C. Such changes in the concentration of methyl and methylene groups with increasing biochar formation temperature indicate that demethylation, demethoxylation and demethylenation are major transformation processes in biochar formation.

The new peak observable, in Fig. 19, between 3100 and 3000 cm^{-1} in biochars formed at temperatures ≥350 ^{o}C is due to the presence of double-bond CH (C=C-H) groups. Peak intensities suggested that C=C-H: (i) generally increased with biochar formation temperature; (ii) accounted for 0-7, 13- 20 and >90 percent of CH in biochars formed at 350, 400 and 500 ^{o}C, respectively; and (iii) was the dominant CH functional groups in biochars formed at temperatures ≥450 ^{o}C.

Increased concentration of C=C-H with biochar formation temperature, was consistent with increased conjugation and pointed to dehydrogenation/aromatization as significant transformation processes in biochar formation. That C=C-H were only dominant in biochars formed at ≥450 ^{o}C support other studies that suggest that biochars formed under temperature conditions consistent with natural vegetation fires do not have extensive polyaromatic structures [49, 88].

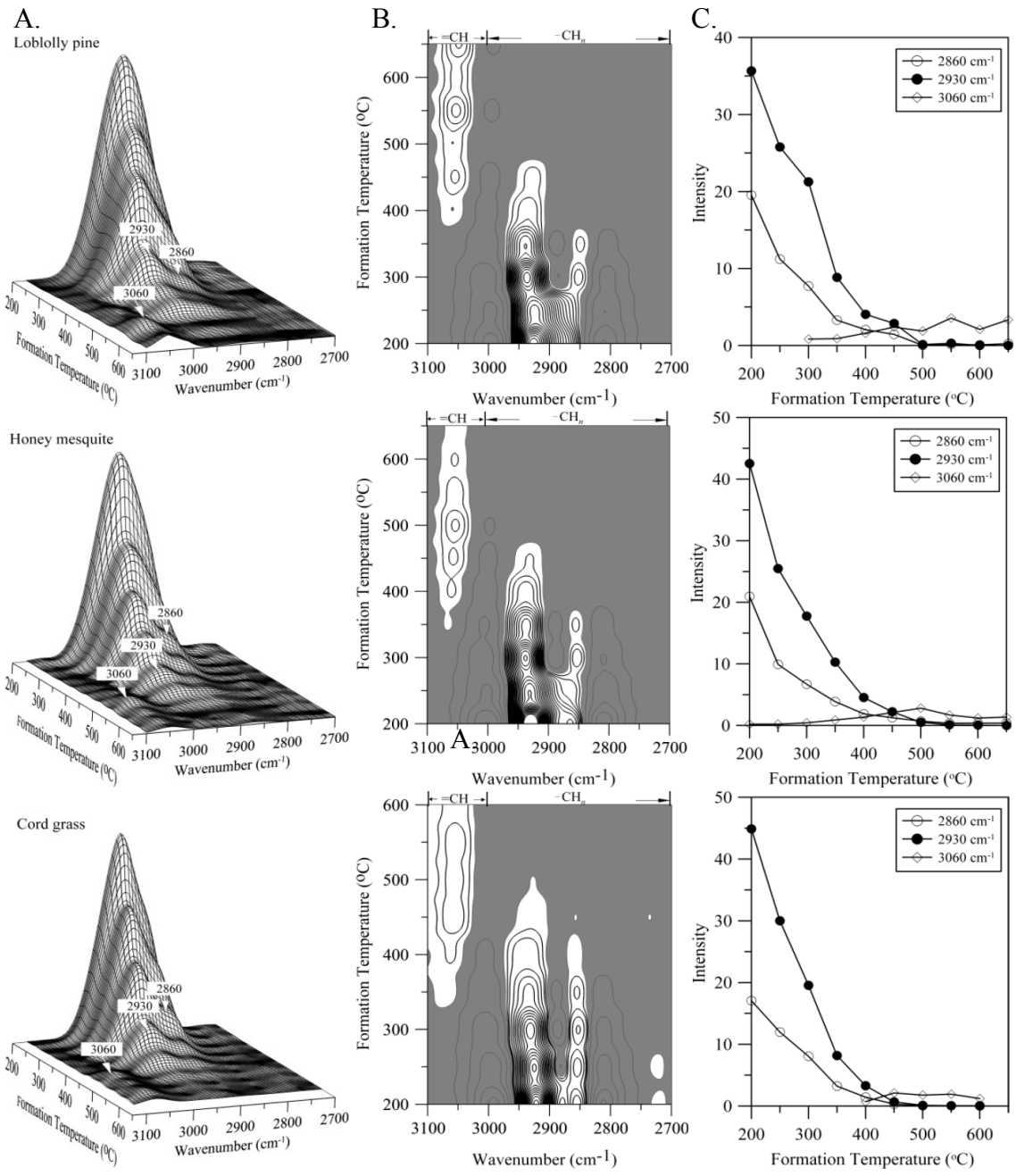

Fig. 19. Infrared spectroscopy analysis in the CH-stretch range for plant-derived formed at temperatures between 200 and 650 °C. (A) 3D representation of the IR spectra; (B) second derivative analysis (white- negative, gray- positive); (C) peak intensity.

Spectral variations between plant-derived biochars in the fingerprint region (1900- 700 cm^{-1}) are shown in Fig. 20. Variations were far more complex than those observed in the OH-stretch or CH-stretch regions. In addition to more peaks, peaks identified in the fingerprint region were attributable to a larger variety of functional groups. Assignment of functional groups to different peaks were largely based on work by Yang et al. [204] and Stuart [209]. Peak deconvolution and assignment of peaks to specific classes of compounds were difficult due to significant peak overlap in the C=O (1800-1700 cm^{-1}), C=C (1650- 1550 cm^{-1}), C-O-C/C-O (1350-1000 cm^{-1}) and OCH_3 (1470-1440 cm^{-1}) regions. The C=O groups in ketones, aldehydes, amides and carboxylic acids all display a strong peak in the 1800- 1700 cm^{-1} range and were difficult to differentiate [209]. A similar case existed with C=C in aromatic rings and alkenes which both display a peak in the 1600 cm^{-1} region.

Despite difficulty in peak deconvolution, 3D representations and 2^{nd} derivation analysis of the fingerprint region highlighted some important transformations with biochar formation temperature and plant species (Fig. 20). For example, 3D representation indicated that with the exception of aromatic H (900- 700 cm^{-1}) which increased, the concentration of all functional groups decreased, with increasing formation temperature. Second derivative analysis also showed a new peak (~820 cm-1 in HM and PI; 760 cm-1 in CG) in biochars formed at temperatures >350 ^{o}C. Both the increase in the concentration of aromatic H and the new aromatic H peak, confirmed the significance of aromatization as a mechanism of transformation during biochar formation, particularly at high temperatures.

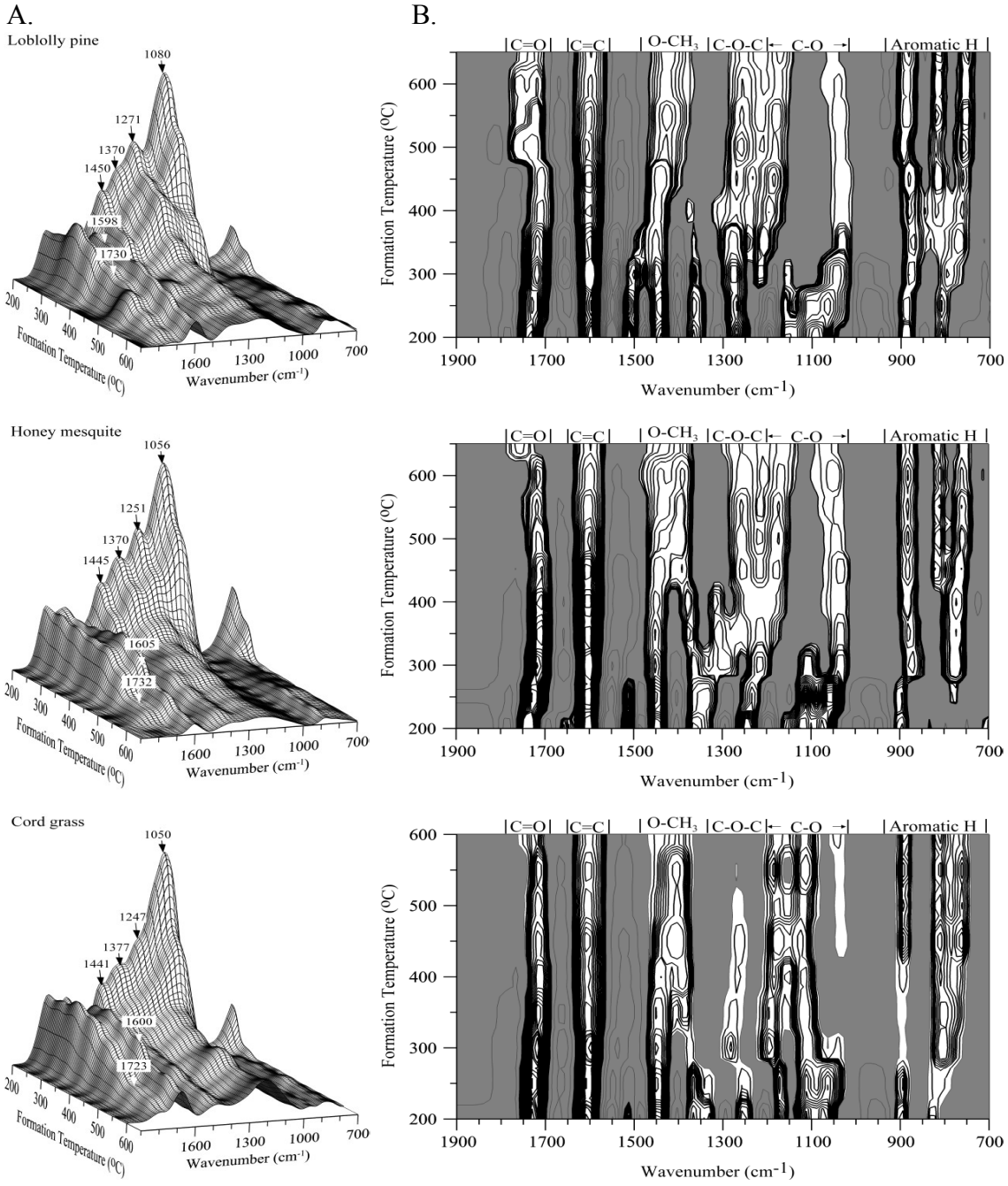

Fig. 20. Infrared spectroscopy analysis in the finger-print region for plant-derived formed at temperatures between 200 and 650 ^{o}C. (A) 3D representation of the IR spectra; (B) second derivative analysis (white- negative, gray- positive).

The new aromatic H peaks, observed in formed at temperatures >350 ^{o}C, were also indicative of changes in H substitution and subsequently the aromatic configuration of the biochars. The peak around 900 cm^{-1} was consistent of 4 or 5 H per aromatic ring; the peak in the 850- 800 cm^{-1} range was specific to H being at the 1, 2, 3, 4- ; 1, 2, 4- or 1,4- substitution positions; and the peak in the 800- 750 cm^{-1} was specific to H being at the 1, 2- substitution positions [209]. Such substitutions would suggest that aromatic domains in the biochars were on the order of 2-4 aromatic rings. This would be consistent with estimates of Knicker et al. [88] who found that, in contrast to soot and other black carbon, which had large polyaromatic domains, aromatic domains in plant-derived biochars (formed under conditions consistent with natural vegetation fires) were less than 6 aromatic rings.

Differences in spectral characteristics in the C=O, C=C, C-O-C/C-O and OCH_3 regions also provided important insights into thermal transformation mechanisms involved in biochar formation. For example, only slight changes in the concentration of C=O and C=C function groups were apparent in the 3D spectra of biochars formed between 200 and 400 ^{o}C (Fig. 20). In contrast, the concentration of C-O-C/C-O and OCH_3 functional groups decreased drastically with increasing formation temperature in the same biochars. In addition to highlighting a sequence for bond cleavage such changes, confirms demethoxylation and, pointed to ether bond-breaking and decarbonylation as significant mechanisms in biochar formation. Ether bond-breaking was more significant at biochar formation temperatures <400 ^{o}C and would include pyranose ring-cracking (during cellulose or hemicellulose degradation) and aryl-alkyl

ether bond cleavage (during hemicellulose or lignin degradation). On the other hand, decarbonylation was more significant at biochar formation temperatures >400 ^{o}C and would include the degradation of acids, aldehydes, ketones and amides.

4.3.2. Thermal transformations influences surface charge characteristics of plant-derived biochars

A summary of the dominant mechanisms controlling the functional group chemistry of plant-derived biochars formed at temperatures up to 650 ^{o}C is shown in Table 6. Here, we examine linkages between transformation mechanisms and surface properties of the plant-derived biochars.

Table 6
Dominant mechanisms active in plant-derived biochars formed at temperatures up to 650 ^{o}C. Mechanisms were inferred from elemental and infrared spectroscopy data.

Biochar formation temperature (^{o}C)	Mechanism
T ≤ 200	Dehydration (loss of physical water) Hydrogen bond weakening
200 ≤ T ≤300	Dehydration (loss of chemical water) Dehydroxylation Ether bond cleavage Demethylation/demethoxylation Demethylenation
300 ≤ T ≤450	Oxidation Depolymerization/fragmentation Decarbonylation/decarboxylation Conjugation/aromatization
>450	Aromatization/dehydrogenation

The cation exchange capacity (CEC), specific surface area (SSA) and surface charge density (as a function of pH) of different plant-derived biochars are shown in Table 7. Selected biochars belonged to one of the 4 temperature ranges defined in Table 6. Cation exchange and specific surface area measurements for the biochars were consistent with values reported for different soils, plant-derived biochars and other naturally-occurring carbon-rich materials [74, 201, 211-217]; but were 1-2 orders of magnitude lower than values reported for soil extracted organic matter, or modified activated carbon and carbon nanotubes [218-222].

Table 7
Surface properties of plant-derived biochars used in flow adsorption micro-calorimetry experiments.

			Surface charge density, σ^-			
Biochars	$CEC_{pH\ 7}$ [a]	SSA [b]	pH 3	pH 5	pH 7	pH 9
	cmol kg^{-1}	$m^2\ g^{-1}$	----------μmol m^{-2}----------			
Loblolly pine						
PI200	16.5	0.796±0.099	54.6	154	206	232
PI300	16.9	1.13±0.012	31.2	109	150	152
PI350	23.8	2.03±0.038	30.1	56.4	117	137
PI650	2.12	81.7±3.51	0.102	0.197	0.259	0.319
Honey mesquite						
HM200	14.9	0.580±0.015	34.5	252	256	274
HM300	18.3	1.28±0.021	23.0	135	143	168
HM350	18.7	1.82±0.101	13.0	98.9	103	106
HM650	5.73	107±2.00	0.216	0.465	0.536	0.620
Cord grass						
CG200	8.05	0.783±0.036	25.4	66.7	103	116
CG300	44.5	1.14±0.080	120	345	391	436
CG350	42.8	2.03±0.042	67.7	161	211	257
CG550	32.4	15.1±0.697	5.74	17.1	21.5	21

[a] Cation exchange capacity at pH 7
[b] Specific surface area (single point N_2-BET)

For biochars formed at 200 ^{o}C, CEC for wood biochars were about twice that for the cord grass biochars. However, for biochars formed at temperatures ≥300 ^{o}C the opposite was true with the CG biochars exhibiting 2-16 times more CEC than the comparable HM and PI biochars. In general, for a given temperature ≥300 ^{o}C, CEC followed the order CG >> HM = PI. The higher CEC in the wood biochars formed at 200 ^{o}C , relative to CG200, was attributed to additional carboxylic group present as calcium oxalate in these biochars. The increase in surface charge density with pH is also consistent with the pH-dependent charged functional groups, such as carboxylic acid. X-ray diffraction analysis of the biochars showed that for HM200 and PI200, cellulose and calcium oxalate were the only crystalline phases present in detectable quantities (Appendix 4). Calcium oxalate was detectable only in HM and PI biochars formed at temperatures ≤400 ^{o}C. For formation temperatures >400 ^{o}C, only $CaCO_3$ were identified in the X-ray diffractograms of HM and PI biochars. This was consistent with the thermal degradation of calcium oxalate to calcite [223]. No calcium oxalate was detected in the CG biochars. X-ray diffraction indicated that, except for cellulose in CG200 and CG250, the only crystalline phases present in the CG biochars were halite (NaCl) and sylvite (KCl). Halite and sylvite were present in all the CG biochars, and was consistent with the coastal original of the cord grass feedstock used to make the biochars [49].

The higher CEC in CG biochars formed at temperatures ≥300 ^{o}C, compared to the wood biochars, was explainable by considering differences in the thermal degradation of the plant materials. Firstly, the HM and PI biochars were derived from woody tissue while the CG biochars were derived from soft tissue [49]. Oxidation of

lignin in soft tissues yields an abundance of cinnamyl phenols, which are virtually absent from woody tissues [224-226]. In contrast to other classes of methoxylated phenols (vanillyl and syringyl), present in lignin, the cinnamyl class is comprised only of acids. Kuo et al. [99] found that the cinnamyl: vanillyl ratio in the uncharred CG, HM and PI plant materials used in this study was 1.13, 0.06 and 0.01 respectively. We believe that the higher CEC in the CG biochars are due at least in part to dissociation of carboxylic groups in the cinnamyl acids. The presence of inorganic salts is also known to influence the chemistry of cellulosic biochars [227-230]. Boon et al. [227] proposed that thermal degradation of cellulose occurred via three major pathways (transglycosylation, cycloreversion, and E_i-elimination); with the dominant mechanism being determined by combustion condition and the presence of inorganic salts. The presence of alkali and alkaline metals is known to inhibit cellulose degradation via the transglycosylation pathway- as evident by a decrease in the formation of levoglucosan [229, 230]. It would be reasonable to suggest that, given the presence of Ca^{2+} (from Ca-oxalate) in the woods and K^+ and Na^+ (from NaCl and KCl) in the grass biochars, cycloreversion and or E_i-elimination were the dominant thermal degradation pathway of cellulose in our biochars. Based on the additional evidence from our DRIFTS analysis, we believe that cycloreversion leading to the formation of additional carboxylic acid groups was the dominant mechanism responsible for cellulose degradation in biochars formed at >300 ^oC. This would be consistent with the waterloo model proposed by Piskorz et al. [228] and is supported by data from Kuo et al. [49] which showed a drastic decrease in the levoglucosan content of biochars formed at temperatures >250 ^oC. The higher CEC in

the CG biochars could also (at least in part) attributed to cycloreversion of hemicellulose, given that hemicellulose content in the cord grass feedstock was approximately 3 times that of the HM and PI feedstocks. Ash from biochars may also contribute to CEC since they contain metal hydr(oxides), whose surfaces may exhibit negative charge characteristics (particularly at pH values greater than their $pK_{a)}$. In general, CG biochars had higher ash content than the wood biochars (Table 5). However, CEC contributions from ash in our study would be insignificant, since the pK_a of metal hydr(oxides) are typically greater than pH 7 [192].

In addition to varying with plant species, CEC of the plant-derived biochars also varied considerably with biochar formation temperatures. For a given plant species, biochars formed at 300 or 350 ^oC had the highest CEC (Table 6). Biochars formed at 550 ^oC (CG) or 650 ^oC (HM, PI) had 10%, 70%, and 90% less CEC than CG350, HM350 and PI350, respectively. On the other hand CG200, HM200 and PI200 had 80%, 20%, and 2% less CEC than CG300, HM300 and PI300, respectively. That the difference in CEC between wood biochars formed at 200 and 300 ^oC were considerably lower, than between CG200 and CG300, was attributable to the presence of Ca-oxalate in the wood biochars. Conversely, that the difference in CEC between wood biochars formed at 350 and 650 ^oC was considerably higher, than between CG350 and CG550, was attributable to the preservation of organic components of CG in phytoliths (silica structures common in some grasses), thereby inhibiting its thermal degradation [201]. The presence of phytoliths in our CG samples could not be ruled out for two primary reasons: (i) the higher ash content of the CG biochars and; (ii) during acid digestion of the biochar ash

we visually observed the presence of silica in CG digests, but no silica was observed in the digests of the wood biochars. Fraysee et al. [231] estimated that the pK_a of silanol groups (>Si-OH^o) on the surfaces of silica phytoliths from several different plant species was 7.5±0.2. Given the relatively high ash content of the CG biochars (8.8 to 30.3) the contribution of CEC from silica phytoliths could not be ruled out. However, the amount of CEC attributable to these phytoliths would be small compared to carboxylic acids, which have much lower pK_a.

The general trend of CEC increasing up to biochar formation temperatures of 300 and 350 ^oC and then decreasing thereafter, was consistent with our DRIFTS data which showed that biochars formed at 300 to 400 ^oC had the highest concentration of free OH and carboxylic acids on their surfaces. Similarly, Kuo et al. [99] found that the acid/aldehyde ratio in vanillyl and syringyl phenols, produced as a result of the oxidation of lignin in the CG, PI and HM biochars , increased with biochars formation temperature; reaching a maximum at 300-350 ^oC. Cation exchange capacity, DRIFTS and lignin oxidation data all highlighted the significance of: (i) inter- and intra-molecular bond cleavage, oxidation and defragmentation/depolymerization mechanisms; and (ii) the type of oxygenated functional group in the development of surface charge on plant-derived biochars. A good demonstration of this is in considering the O/C ratios of biochars (a proxy of the abundance oxygenated functional groups). Despite having considerably higher O/C , biochars formed at 200 ^oC had lower CEC than those formed 300 or 350 ^oC. We attributed this to molecular configuration of the plant macromolecules in the biochars. At 200 ^oC intra-and inter-molecular hydrogen bonding

are dominant in the biochars and only a small amount of dissociable hydroxyls/carboxyls are available for dissociation. However, as the temperature increases above 200 ^{o}C and thermal degradation of the macromolecules sets in, the hydrogen bonding network disintegrates resulting in defragmentation/depolymerization. Although some oxygenated functional groups may be lost during thermal degradation, accounting for the decline in O/C ratio, the net effect of oxidation and defragmentation/depolymerization is an increase in hydroxyls/carboxyls available for dissociation. We believe that it is the subsequent dissociation of H from these functional groups, particularly carboxylic groups, in an aqueous environment that are responsible for the higher CECs observed in biochars formed at 300 and 350 ^{o}C compare to those formed at 200 ^{o}C. The lower CEC in the CG550, PI650 and HM650 are due to further loss of these oxygenated functional groups with increasing temperature, as the thermal degradation of the "fragments", and carbonization/aromatization of the biochar increases. This would be consistent with both our DRIFTS data, which showed a rapid decline in C=O concentrations in biochars formed above 400 ^{o}C, and; the waterloo model for the thermal degradation of cellulosic materials [228], which showed an increase then decrease, of the acid content of cellulose biochar with increasing temperature.

Further evidence of carboxylic acid groups being the primary contributor to the CEC of the plant-derived biochars was also apparent from variations in surface charge with pH (Table 6). Irrespective of formation temperature or plant species, for a given biochar, surface charge density increased with pH. On average surface charge density on the biochars were 4.9±1.9 times higher at pH 9 than at pH 3. The largest change was

observed between pH 3 and 5 with surface charge density increasing by a factor of 3.7±2.1, compared to 1.3±0.3 and 1.1±0.1 from pH5- 7 and pH 7- 9, respectively. In addition to indicating that the plant-derived biochars were dominated by pH-dependent charge, the variations in surface charge with pH were consistent with the dissociation of a weak acid, with an acid dissociation constant (pK_{a1}) between pH 3 and 5. Using a modified Henderson-Hasselbalch model we estimated the pK_{a1} values of 4.45, 3.94 and 4.30 for the PI, HM and CG biochars, respectively. The model used to estimate pK_{a1} was of the form: $f_{RCOO^-,\,pH_i} = 1 - [10^{-c(pH_i - pK_{a1})}/\,(1 + 10^{-c(pH_i - pK_{a1})})]$, where $f_{RCOO^-,\,pH_i}$ is the fraction of deprotonated carboxylic groups on the biochar surface at a given pH value pH_i, c is a curve fitting parameter and pK_{a1} is the first acid dissociation constant of the RCOOH on the biochar surface. Values of pK_{a1} and c are determined by least square optimization of the model, based on a plot of $f_{RCOO^-,\,pH_i}$ versus pH. The fitting parameter c ranges in value from 0 to 1. At $c = 1$ the model is equivalent to the Henderson-Hasselbalch equation and defines a surface dominated by a single monoprotic acid. On the other hand, values of $c < 1$ define a surface comprising of several acidic functionalities with slightly different pK_{a1}. In such as case, acid dissociation constants would represent an average pK_{a1} rather than an absolute value.

Experimental data and model fits for the PI, HM and CG biochars are shown in Fig. 21. It was assumed that at pH 9 all the RCOOH sites are deprotonated and therefore $f_{RCOO^-,\,pH_i}$ was equal to 1. Values for $f_{RCOO^-,\,pH_i}$ at pH7, pH5 and pH3 were subsequently calculated as a ratio of the charge density at the respective pH to that at pH9. Estimated pK_{a1} values of 4.45, 3.94, and 4.30 for PI, HM and CG biochars, respectively were

consistent with those reported for natural organic matter (including humic and fulvic acids) [232] and hydroxylated benzoic acids commonly formed during the thermal degradation of lignin [233-235]. For example, Erdemgil et al. [234] reported pK_{a1} ranges of 4.30-4.58, 4.08-4.31, 3.86-4.20, 4.32-4.39 and 4.27-4.56 for *p*-hydroxybenzoic, vanillic, syringic, *p*-coumaric and ferulic acids, respectively. This provided additional evidence to support the contribution of thermally produced syringyl, vanillyl and cinnamyl (*p*-coumaric and ferulic) acids to surface charge on plant-derived biochars. The fact that values for *c* (0.35, 0.68, and 0.34 for PI, HM and CG biochars, respectively) varied considerably from 1, also suggested that a heterogenous mix of these acidic functionalities (rather than a single dominant acidic group) control surface charge in plant-derived biochars.

Table 7 also showed that, surface charge density on the plant-derived biochars varied with plant species and formation temperature. Irrespective of solution pH, surface charge density on HM200 and PI200 biochars were 1.4-3.8 times higher than CG200 biochar. Surface charge density on HM and PI biochars also decreased consistently with increasing formation temperature. However, for CG biochars, surface charge density initially increased (200-300 ^{o}C) and then decreased with increasing formation temperature. The higher surface charge density of the HM200 and PI200 biochars, compared to CG200, was consistent with CEC data and, as discussed earlier, was attributable to the presence of Ca-oxalate in the wood biochars. Similarly, the initial increase in surface charge density between CG200 and CG300 was consistent with CEC data. Here increases in surface charge was attributable to the increased availability of

carboxylic groups, as a result of the disintegration of the hydrogen bonding network and thermal degradation of biomacromolecules in cord grass.

The decrease in surface charge density with increasing formation temperature, observed in PI, HM and CG plant-derived biochars, can be explained by considering the simultaneous effects of temperature on surface charge and specific surface area. As discussed earlier, surface charge on the biochars increased up to formation temperatures of 300 ^{o}C (for CG) or 350 ^{o}C (for HM and PI) and then decreased thereafter. On the other hand, specific surface area of the PI, HM and CG biochars increased with formation temperature over the entire temperature range (Table 7). With the exception of CG biochars, for temperature ranges where both surface charge and specific surface area increased with formation temperature, surface area increased at a faster rate than surface charge. Additionally, while surface charge decreased at formation temperatures >300 ^{o}C (CG) or 350 ^{o}C (HM and PI), specific surface area increased significantly for the same temperature range. The net effect of either scenario is that a given number of charge is spread over a continuously enlarging area as biochar formation temperature increases.

Increasing specific surface area with biochar formation temperature has been attributed to increasingly accessible internal surfaces, due to volatilization of tars (produced as a result of thermal degradation of hemicellulose, cellulose or lignin) from the microporous structure of the biochars [81, 236, 237].

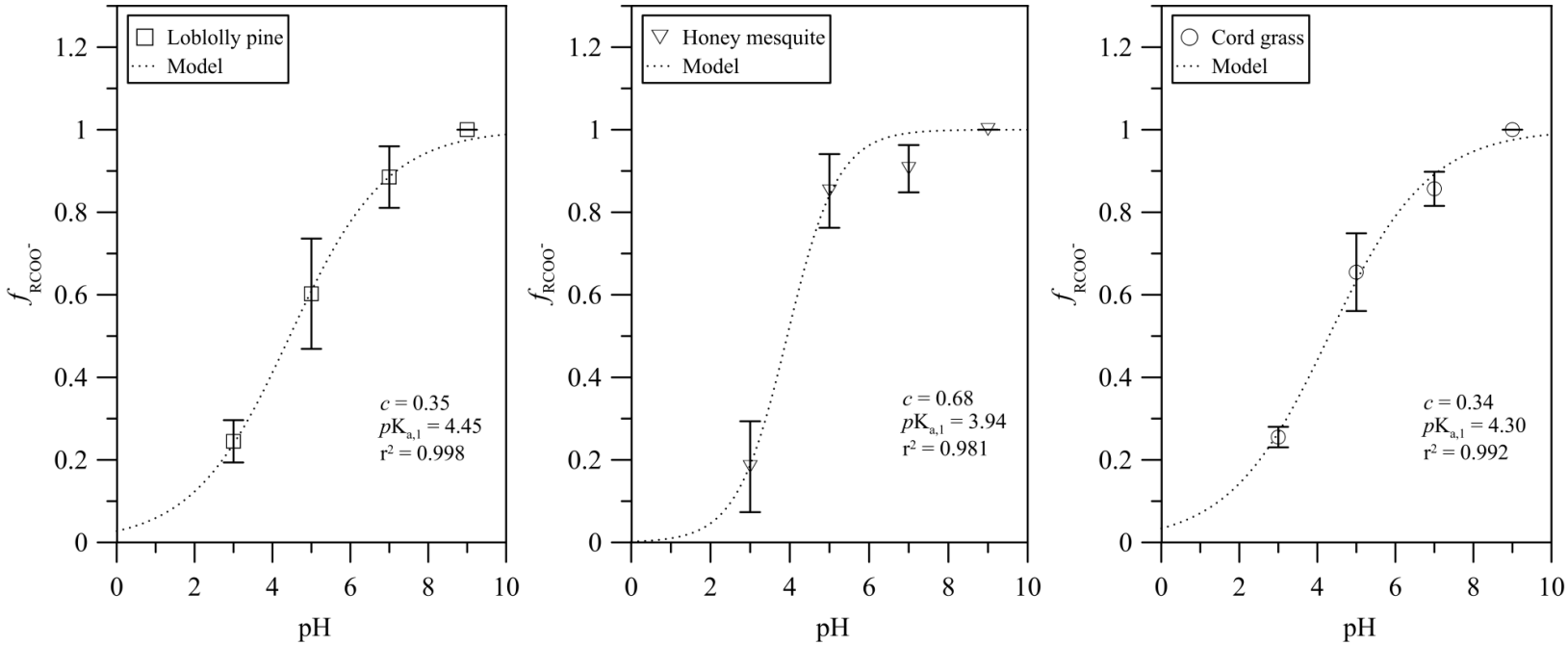

Fig. 21. Dissociation characteristics of acidic functional groups on the surface of loblolly pine, honey mesquite and cord grass plant-derived biochars. Values for the fraction of dissociated acidic groups, f_{RCOO^-}, at a given pH is the average for biochars formed at 250, 300, 350, 550 (for CG) and 650 ^{o}C (for HM and PI), respectively. Error bars represent the standard deviation across formation temperatures.

The lack of significant internal microporosity is a plausible explanation for the low surface areas (< 3 m^2 g^{-1}) observed in PI, HM, and CG biochars formed at 200, 300 and 350 ^oC (Table 7). This may also account for the lack of variability in SSA, across plant species, observed in these biochars. The drastic increase in SSA of biochars formed at 550 ^oC (CG) and 650 ^oC (HM and PI) suggested that significant volatilization of tar, and the accompanying increase in microporosity, occurred in the 350 to 650 ^oC temperature range. This was consistent with observations made by Chen et al. [81] who found that surface area of pine needle biochars increased sharply from 19.92 m^2 g^{-1} to 112 m^2 g^{-1}between formation temperatures of 300 and 400 ^oC.

In contrast to plant-derived biochars formed at lower temperatures, SSA of those formed at 550 ^oC and 650 ^oC varied significantly with plant species. Specific surface area of these higher temperature biochars followed the order HM > PI > CG. Variability in SSA suggested significant differences in the micropore structure of these biochars. This was particularly obvious when comparing grass to wood biochars. The significantly lower SSA of CG550 (15.1 m^2 g^{-1}), compared to HM650 (107 m^2 g^{-1}) and PI650 (81 m^2 g^{-1}), suggested much lower microporosity in grass than wood biochars. This was not surprising given that the chemical structure of the cell wall of grasses differ significantly from those other plants [238]. The lower SSA and associated microporous structure of CG550 may also be attributed to the blocking of micropores by silica phytoliths present in the cord grass [239]. Silica phytoliths would be more thermally stable than the Ca-oxalate phtyoliths in the wood biochars and would persist at higher temperatures than the 400 ^oC at which Ca-oxalate thermally degrades [223, 240].

4.3.3. K^+/Na^+ exchange on plant derived biochars as determined by flow adsorption micro-calorimetry

A typical suite of heat signal curves obtained for K^+ replacing Na^+ (K^+/Na^+) and Na^+ replacing K^+ (Na^+/K^+) on the surface of the plant-derived biochars is shown in Fig. 22. Exothermic heat signal indicated that K^+/Na^+ on the biochars was an exothermic process. Similarly, the endothermic heat signal indicated that the reverse reaction, Na^+/K^+, was an endothermic process. Differences in the shape of the heat signals also pointed to differences in K^+/Na^+ and Na^+/K^+ sorption characteristics. However, despite these differences, for a given pH; the total energy evolved during a K^+/Na^+ cycle or absorbed during a Na^+/K^+ cycle were the same (Fig. 22B). In addition to showing that the heats of both reactions were the same, Fig. 22B also indicated that K^+/Na^+ and Na^+/K^+ sorption on the plant-derived biochars were both reversible reactions. Similar observations have been reported for other sorbent systems and were characteristic of simple ion exchange [192, 194, 195]. Observed differences in the shape of K^+/Na^+ and Na^+/K^+ heat signals were therefore attributed to difference in K^+ and Na^+ sorption kinetics, rather than difference in sorption mechanisms.

The sharper K^+/Na^+ heat signals in Fig. 22, compared to Na^+/K^+, was consistent with a faster apparent rate of K^+ sorption onto the biochar surface and suggested a higher affinity for K^+ relative to Na^+. That the biochar surface had a higher affinity for K^+ than Na^+ correlated well with the lyotropic series for cation exchange on a given negatively charge surface [215]. Since K^+ and Na^+ are both monovalent, the difference in affinity was attributed to differences in hydrated radius. Based on Coulomb's law, the interaction

energy between a charged surface and an oppositely charged solute is proportional to the solute's charge and inversely proportional to the hydrated radius [215]. The smaller hydrated radius of the K^+ ion (0.331 nm), compared to that of Na^+ (0.358 nm, [241]), allows for a closer association between the negatively charged biochar surface and the positively charge K^+ ion.

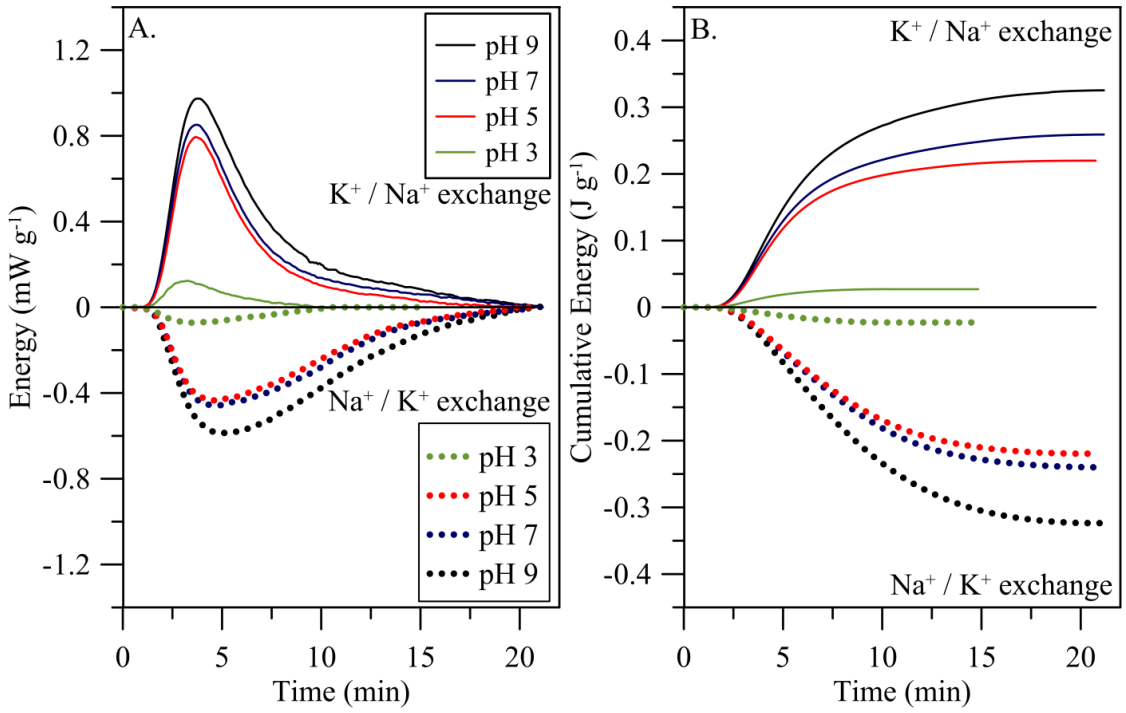

Fig. 22. Typical heat signals for ion exchange reaction between K^+ and Na^+ on plant-derived biochars.

The smaller hydrated K^+ ions are also likely to be subject to less steric hindrances (such as charge shielding), compared to the larger Na^+, thereby allowing for easier access to the cation exchange sites. Sorption studies on other carbon-rich materials have also found that, for cations of the same valence, smaller hydrated cations are more

readily adsorbed via cation exchange [242-244]. For example, Duong et al. [242] found that, compared to Co^{2+} and Cd^{2+}, Ni^{2+} was more readily adsorbed to kraft paper pulp. They postulated that the higher sorption of Ni^{2+} was due to its smaller hydrated radius, and subsequent potential to penetrate deeper into the pulp.

Fig. 22 also showed that heat signal intensities, cumulative energies and therefore the amount of heat evolved or absorbed during K^+/Na^+ or Na^+/K^+ exchange, varied with solution pH. The trend was similar to that observed from surface charge data, which showed an increase in the surface charge density of cation exchange sites on the biochars, with increasing pH. Increased evolution or absorption of heat with increasing pH, was consistent with increase deprotonation of surface functional groups; and was supportive of the biochar surface being dominated by pH-dependent cation exchange sites. The simultaneous variability in reaction energies and surface charge with pH, also suggested a direct relationship between the amount of energy evolved or adsorbed (during K^+/Na^+ or Na^+/K^+) and the amount of K^+ or Na^+ adsorbed, respectively. This was confirmed by Fig. 23, which showed a strong linear relationship between heats of K^+/Na^+ exchange (E_{Total}) and the quantity of K^+ adsorbed (K_{Exch}). Correlation coefficients between E_{Total} and K_{Exch} were 0.95, 0.96 and 0.97 for PI, HM and CG biochars, respectively.

Strong linear relationships between heats of adsorption and the quantity of sorbate adsorbed have also been reported for ion exchange on metal hydr(oxides) [192]. In such cases, providing that the intercept is not significantly different from zero, the average molar heat of adsorption (ΔH_{ads}) is equivalent to the slope of the E_{Total} versus

K_{Exch} regression line. Slopes of E_{Total} versus K_{Exch} for the PI, HM and CG biochars were 3.61, 3.19 and 7.92 J mmol^{-1} of K^+ respectively. By convention, since K^+/Na^+ exchange is an exothermic process, molar heats of K^+/Na^+ exchange ($\Delta H_{ads,\ K^+/Na^+}$) were -3.61, -3.19 and -7.92 kJ mol^{-1}, respectively. These values were comparable with molar heats of ion exchange on other materials [169, 192, 194, 195]. Rhue et al. [195] reported ΔH_{ads} values of 7.5 kJ mol^{-1} and 7.8 kJ mol^{-1} for K^+/Na^+ and K^+/Ca^{2+}, respectively. Lyubchik et al. [169] calculated a ΔH_{ads} value of 3.05 kJ mol^{-1} for Cr^{3+} adsorption to an activated carbon. Based on this value they concluded that sorption of Cr^{3+} on the activated carbon occurred via ion exchange.

The more negative molar heat of K^+/Na^+ exchange obtained for the CG biochars suggested that K^+ was more favorably adsorbed onto these surfaces, compared to the wood biochars. This was reflected in both the amount of K^+ adsorbed and the amount of energy evolved. For a given pH and biochar formation temperature, the amount of K^+ adsorbed and the amount energy evolved was consistently 2-3 times higher in the CG, than in HM and PI biochars (Fig. 23). Since deprotonated carboxylic groups were the primary sites of K^+ sorption on both the grass and wood biochars, we postulated that the observed differences in molar heats of K^+ sorption were due to structural differences in the hydrocarbon backbone to which the carboxyls are attached. Data from Kuo et al. [99] showed that although the benzoic acid derivative, vanillic acid was present in appreciable quantities in the CG, HM and PI biochars, its concentration was 2-4 times higher in the wood biochars (HM and PI), than in the grass biochars (CG). On the other hand, the cinnamic acid derivatives – *p*-coumaric and ferulic acid – were found in

appreciable quantities only in the CG biochars. In cases where the cinnamic acids were detected in the wood biochars, their concentrations were 1-2 orders of magnitude lower than in the grass biochars. Kuo et al. [99] attributed the higher *p*-coumaric and ferulic acid concentrations in the CG biochars to the abundance of cinnamyls in the lignin of soft plant tissues. Cinnamyls are virtually absent from the lignin of woody tissues [224-226]. Structural differences in benzoic versus cinnamic type carboxylic groups could account for the differences in molar heats of K^+ adsorption between the grass and wood biochars. Structurally, the primary difference between benzoic and cinnamic acid derivatives is the presence of an ethylenic group between the phenyl ring and the carboxylic acid group in the cinnamic acids.

In addition to influencing the proximity of the carboxyl, the presence of the ethylenic group in the cinnamic acids will influence the electron-donating and electron-withdrawing characteristics of the phenyl ring and carboxylic group, respectively. The net effect is a greater H^+ donating ability for cinnamic acids compared to their the benzoic acid counterparts [245]. This would be consistent with our findings which showed that K^+ was more favorably adsorbed to the cinnamic acid dominated CG biochars compared to the benzoic acid dominated HM and PI biochars. Similar structure-reactivity relationships have been used to explain the greater free radical scavenging ability of cinnamic acids, compared to benzoic acids [245, 246].

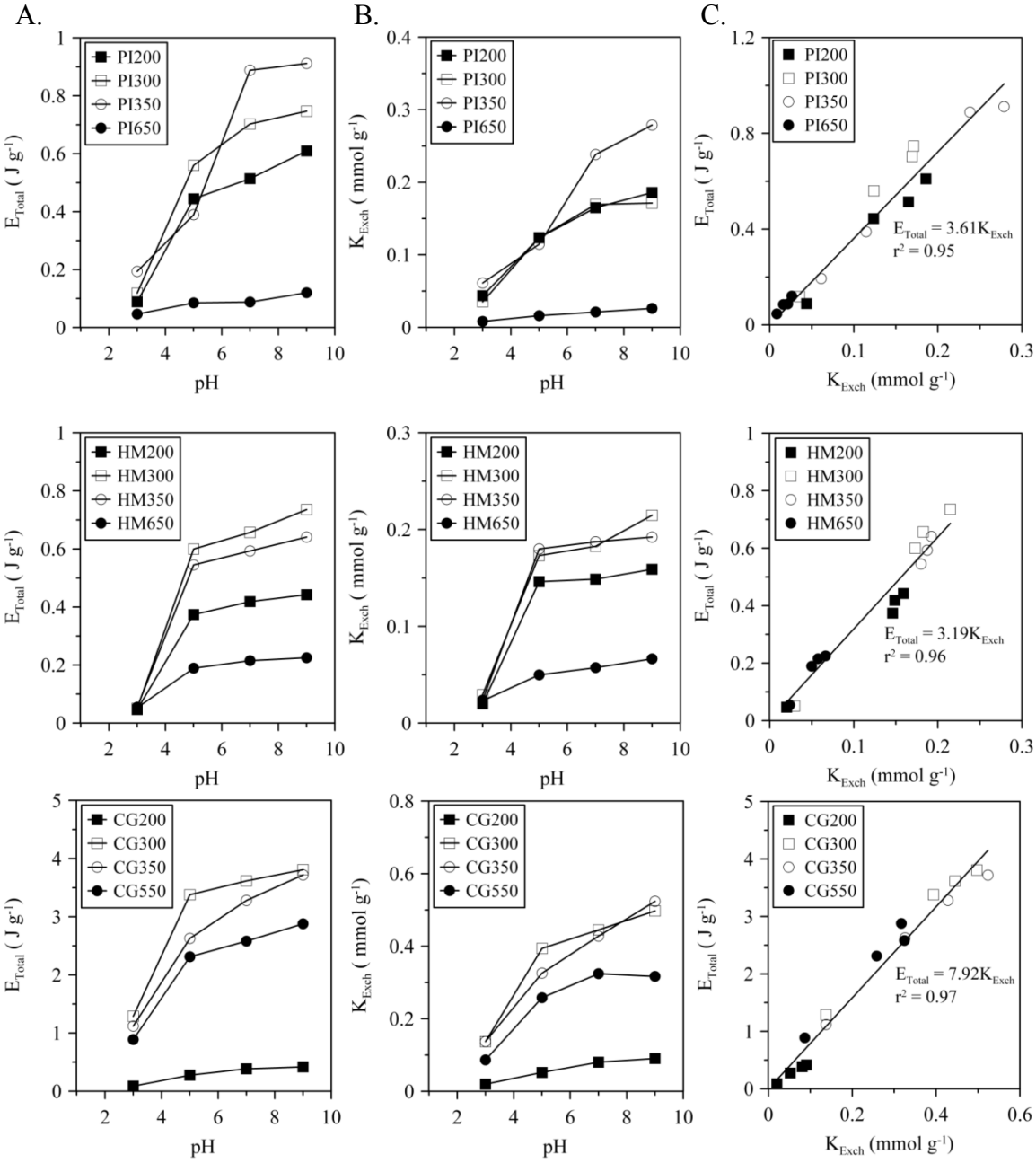

Fig.23. Variation in (A) energy evolved, (B) K^+ adsorbed and (C) their relationship as a result of K^+/Na^+ exchange on loblolly pine (PI), honey mesquite (HM) and cord grass (CG) biochars at different solution pH.

The total amount of energy evolved during K^+/Na^+ exchange on the CG, PI and HM biochars also varied with biochar formation temperature (Fig. 23). For a given plant species, maximum heat evolution was observed in the 300 ^oC or 350 ^oC biochars. This was indicative of K^+ sorption capacity being highest in these biochars, and was consistent with cation exchange and DRIFTS data which showed that cation exchange capacity, as well as the concentration of free OH and carboxylic groups were highest in the 300 to 400 ^oC range. Kuo et al. [99] also showed that acid: aldehyde ratios, for syringic and vanillic lignin oxidation products in the biochars, were highest in the 300 to 350 ^oC temperature range.

4.3.4. Cadmium (Cd^{2+}) sorption characteristics on plant derived biochars as determined by flow adsorption micro-calorimetry

Heat signals for Cd^{2+} sorption onto Na^+-saturated PI, HM and CG biochars are shown in Fig. 24. In all cases endotherms were obtained; indicating that, irrespective of plant species or biochar formation temperature, Cd^{2+} sorption onto the plant-derived biochars was endothermic. Despite being opposite to observations for K^+/Na^+ exchange, the endothermic nature of Cd^{2+} sorption on the biochars was consistent with studies of heavy metal sorption on other carbon-rich materials [83, 169, 247-249] and mineral surfaces [250, 251]. Liu et al. [83] found that, consistent with expectations of endothermic reactions, higher reaction temperatures favored the sorption of Pb^{2+} onto pinewood and rice husk biochars. Similar observations have been reported for Pb^{2+}, Zn^{2+} and Ni^{2+} sorption on carbon nanotubes [249], as well as Cd^{2+} sorption to activated carbon [247, 248]. That K^+ replacing Na^+ on the biochar surface was exothermic, but

Cd^{2+} replacing Na^{+} was endothermic may be related to differences in the hydration characteristics of Cd^{2+} and K^{+}. For example, compared to K^{+}, Cd^{2+} has a larger enthalpy of hydration (Cd^{2+} = 1830 kJ mol^{-1}, K^{+} = 330 kJ mol^{-1}[252]) and larger hydrated radius (Cd^{2+} = 0.426 nm, K^{+} = 0.331 nm [241]). The net effect is that the hydration sphere of Cd^{2+} is more tightly held together, than that of K^{+}, and therefore requires higher activation energy to initiate sorption. This would explain why Cd^{2+}sorption increases with temperature and is consistent with observations by Latenois et al. [251] who found that the holding of some thermal energy was necessary to initiate Cd^{2+} sorption on a macroporous silica.

Differences in the shape and duration of the heat signals in Fig. 24 suggested changes in Cd^{2+} sorption characteristics with biochar formation temperature. For biochars formed at temperatures below 350 ^{o}C the shape and duration of the Cd^{2+} heat signals; were similar to those for K^{+}/Na^{+} exchange, but were considerably different from those obtained for Cd^{2+}sorption on the biochars formed at ≥350 ^{o}C. Similarities between the heat signals for Cd^{2+} sorption on biochars formed at temperatures <350 ^{o}C, and K^{+}/Na^{+} exchange suggest the involvement of ion exchange during Cd^{2+} sorption. On the other hand, differences in heat signals obtained for biochars formed at ≥350 ^{o}C suggested the involvement of an additional mechanism(s). Evidence for such additional mechanism(s) was apparent 15 minutes after the onset of Cd^{2+} sorption and appeared to be preceded by ion exchange.

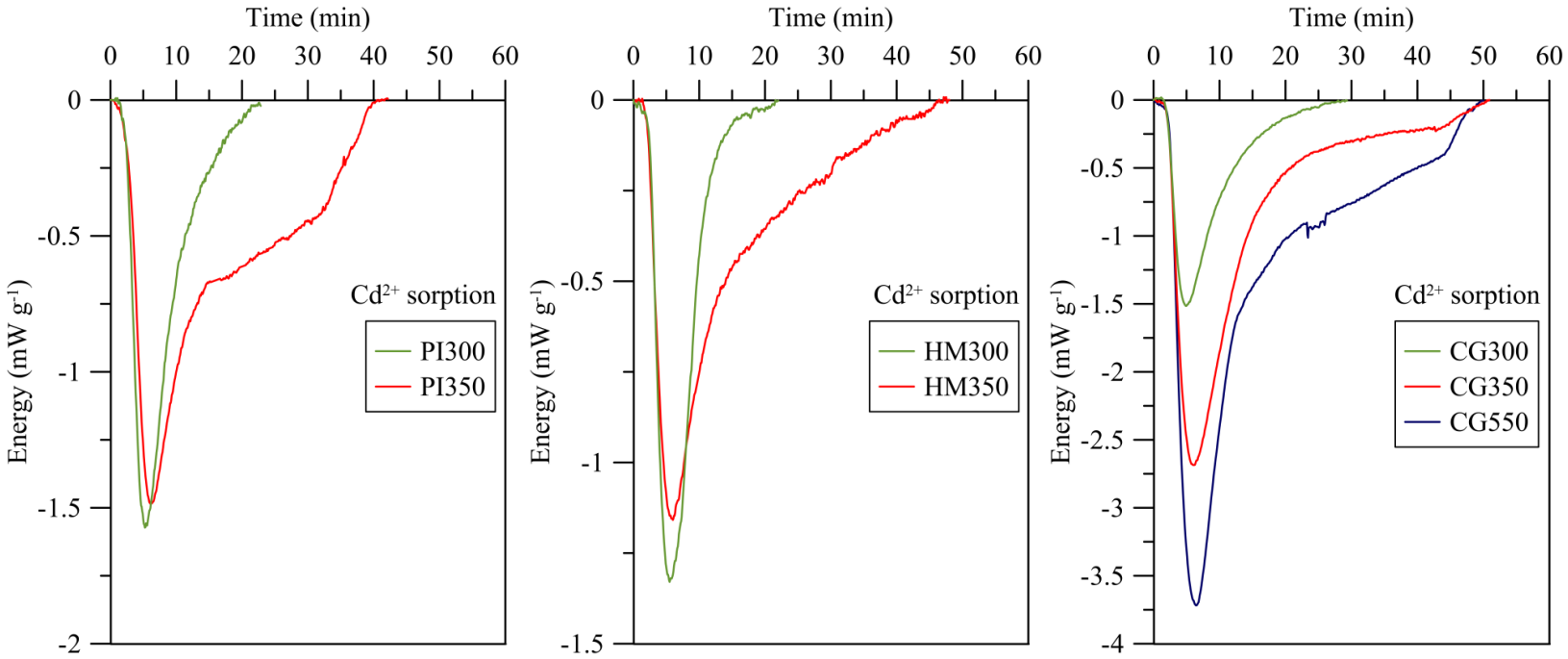

Fig. 24. Calorimetric heat signals for Cd^{2+} sorption onto selected Na^{+}-saturated loblolly pine (PI), honey mesquite (HM) and cord grass (CG) biochars.

Further evidence for the involvement of a second mechanism, besides simple ion exchange, during Cd^{2+} sorption on the biochars can be seen in Fig. 25. Biochars formed below 350 ^{o}C clustered around a common line and those formed at higher temperatures clustered along another line. Regression parameters for the two lines were different, suggesting that Cd^{2+} was possibly adsorbed by different reaction mechanisms.

Both single and multiple mechanisms have been used to explain heavy metal sorption on different biochars. Based on estimates of Gibb's free energy, Liu and Zhang [83], attributed sorption of Pb^{2+} on rice husk and pinewood biochars (produced at 300 ^{o}C) solely to physical adsorption. On the other hand, Chen et al. [102] concluded that sorption of Ag^{+} and Cu^{2+} on maple wood biochars (produced at 400 ^{o}C) occurred at least by two mechanisms. As evidence they pointed to the fact that; (i) stoichiometrically, observed decrease in pH (indicative of proton exchange) with Ag^{+} and Cu^{2+} sorption was inconsistent with pure ion exchange; and (ii) pH decrease with sorption was not significantly different on an oxygenated biochar sample compared to a hydrogenated sample. In addition to ion exchange, Chen et al. [102] suggested that sorption of Ag^{+} and Cu^{2+} on their biochars may also occur via surface complexation, with other functional groups (eg. R-OH, R-O-R, R=O, R-CHO).

At least from a qualitative perspective, both the conclusion by Lui and Zhang [83] and Chen et al. [102] were consistent with observed variations in the shape of Cd^{2+} heat signals in our study. Quantitative information on Cd^{2+} adsorbed to the PI, HM and CG biochars, as well as associated ΔH_{ads}, is summarized in Table 8. The amount of Cd^{2+} adsorbed on the biochars were consistent with reported values for maximum sorption

capacities of Cd^{2+} on oxidized carbon nanotubes [253, 254] and activated carbon [255, 256]. For CG and PI biochars, the amount of Cd^{2+} adsorbed generally increased with biochar formation temperature and was positively correlated to surface area (r^2 = 0.982 and 0.999 for CG and PI, respectively). No such relationship was found between the amount of Cd^{2+} adsorbed on the HM biochars, biochar formation temperature or surface area. The reason for this is unknown, but suggests species-dependent differences in Cd^{2+} sorption characteristics on plant-derived biochars. The strong correlation between surface area and the Cd^{2+} adsorbed on the CG and PI biochars indicated that Cd^{2+} sorption was a surface controlled process.

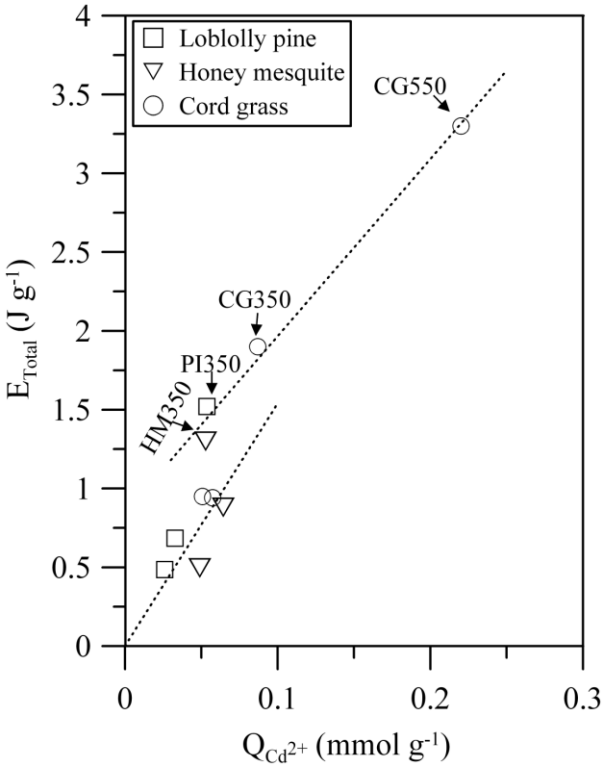

Fig. 25. Relationship between the heat of adsorption (E_{Total}) and amount of Cd^{2+} adsorbed on plant-derived biochars.

Comparison of Cd^{2+}: K^+ ratios showed varying degrees of surface charge saturation (Table 8). Assuming monodentate sorption of Cd^{2+} and a purely electrostatic (ion) exchange mechanism, surface charge saturation on the biochars would be equivalent to Cd^{2+}: K^+. On the other hand, if bidentate sorption is assumed the surface charge saturation would be double the Cd^{2+}: K^+ ratio. Marzal et al. [247] found that Cd^{2+} sorption on activated carbon was best modeled when bidentate sorption is assumed. Here, bidentate sorption will also be assumed. With such assumptions surface charge saturation would range between 26 and 218 %. Surface charge saturation decreased with surface charge density, suggesting that cation exchange was favored at lower surface charge densities (Fig. 26). This was unexpected, but consistent with steric effects arising from charge shielding. An alternative explanation is that Cd^{2+} was unable to effectively displace Na^+ from the Na^+-saturated biochar surface. This would be consistent with observations made by Youssef et al. [174] who found that Cd^{2+} sorption on several activated carbons was considerably decreased in the presence of Na^+.

Values of surface charge saturation greater than 1 (Cd^{2+}: $K^+ > 0.5$) are indicative of Cd^{2+} being adsorbed onto other surface sites, besides cation exchange sites. Two biochars (CG200 and CG550) had surface charge saturation values greater than 1 (Table 8), suggesting the involvement of other reaction mechanism(s) besides ion exchange. One likely mechanism was surface complexation on uncharged oxygenated functional groups [102].

Molar heats of Cd^{2+} sorption on the biochars were between +10.1 and +28.3 kJ mol^{-1} and were 1.7 to 8.3 times higher than the associated ΔH_{ads} for K^+/Na^+ exchange

(Table 8). The considerably higher values of ΔH_{ads} for Cd^{2+} compared to K^+/Na^+ exchange were supportive of earlier suggestions of the involvement of other reaction mechanisms (besides simple ion exchange) in Cd^{2+} adsorption. Values of ΔH_{ads} for Cd^{2+} sorption were lower than that expected for covalent bond formation, but was consistent with expectations for surface complexation. An ion exchange/ surface complexation mechanism would account for Cd^{2+} sorption on biochars formed at <350 ^oC. Molar heats of adsorption for biochars formed at ≥350 ^oC were comparable to ΔH_{ads} for biochars formed at lower temperatures. The tailing observed in heat signal peaks for the ≥350 ^oC biochars was therefore attributable to diffusion, suggesting that Cd^{2+} sorption in these biochars occurred via an ion exchange/surface complexation/diffusion mechanism.

Similar ΔH_{ads} values to those shown in Table 8 have been reported for Cd^{2+} sorption on activated carbon [247, 248, 255] and macroporous silica [251]. Marzal et al. [247] reported ΔH_{ads} between +10 and +30 kJ mol^{-1}. They attributed variations in ΔH_{ads} to Cd^{2+} being adsorbed to different hydroxo species on the surface of the activated carbon. A similar scenario could also be used to explain variations in our ΔH_{ads} values and was consistent with earlier observations which showed that the surface of the biochars were comprised of acidic groups with different pK_a. Latenois et al. [251] also found that the ΔH_{ads} for the first molecule of Cd^{2+} adsorbed was different from that for the second. Variations in the energy input required to adsorb each additional molecule of Cd^{2+} would have also contributed to variations in ΔH_{ads} values obtained in our study.

Table 8
Quantity of Cd^{2+} and K^+ adsorbed and their energetics of sorption onto loblolly pine (PI), honey mesquite (HM) and cord grass (CG) biochars at pH5.

Biochar	$K_{Exch,\ pH5}$[a]	Q_{Cd2+}[b]	Q_{Cd2+} / $K_{Exch,\ pH5}$[c]	$\Delta H_{ads,\ K+/Na+}$[d]	$\Delta H_{ads,Cd2+}$[e]
	-- $\times 10^{-5}$ mol g^{-1}--		mol mol^{-1}	---------- kJ mol^{-1}---------	
Loblolly pine					
PI200	12.4	2.60	0.210	-3.60	+18.7
PI300	12.4	3.28	0.265	-4.53	+20.9
PI350	11.5	5.37	0.467	-3.39	+28.3
Honey mesquite					
HM200	14.6	6.44	0.441	-2.55	+13.7
HM300	17.3	4.89	0.283	-3.46	+10.1
HM350	18.0	5.20	0.289	-3.03	+24.6
Cord grass					
CG200	5.20	5.70	1.09	-5.27	+16.4
CG300	39.4	5.10	0.129	-8.57	+18.7
CG350	32.6	8.70	0.267	-8.06	+21.8
CG550	25.8	22.0	0.853	-8.94	+15.0

[a] K^+ adsorbed at pH5
[b] Cd^{2+} adsorbed at pH5
[c] Fraction of exchange sites occupied by Cd^{2+}
[d] Molar heats of K^+/Na^+ exchange
[e] Molar heats of Cd^{2+} sorption

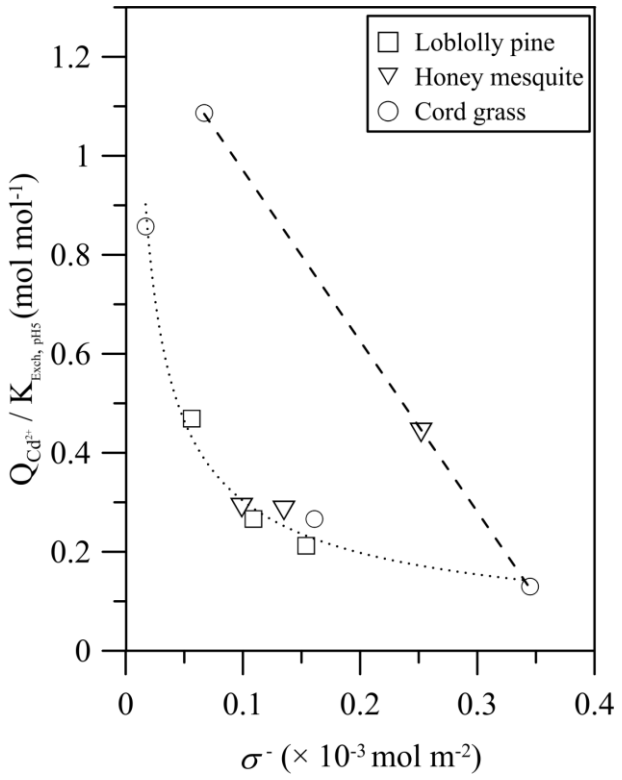

Fig. 26. Variation in Cd^{2+} saturation of cation exchange sites with surface charge density (σ^-) on plant-derived biochars.

4.4. Summary and conclusions

Changes in the functional group chemistry, cation exchange and cadmium sorption on plant-derived biochars (formed at temperatures between 200 and 650 ^{o}C) from three species were studied using DRIFTS and FAMC. Changes in biochar spectral behavior in the OH-stretch region of the infrared spectrum were consistent with dehydroxylation/dehydration, hydrogen bond weakening and formation of carboxylic groups. Dehydroxylation/dehydration from the thermal degradation of cellulose accounted for differences in spectral behavior of biochars formed at less than 300 ^{o}C. For biochars formed in the temperature range 300≤ T≤ 500 ^{o}C spectral differences were

attributed to hydrogen bond weakening and formation of carboxylic groups. The highest concentration of free OH and carboxylic groups were observed in biochars formed in 300- 400 ^{o}C range. Spectral variation in the CH stretch range indicated that for biochars formed at temperatures ≥450 ^{o}C, the dominant CH functional groups were double-bond CH (=CH) suggesting higher degree of conjugation or aromatic character than biochars formed at lower temperatures. For biochars for at <450 ^{o}C demethylation, demethylenation and dehydrogenation accounted for spectral differences in the CH stretch range. Spectral variations in the fingerprint region of the infrared spectra were consistent with thermal transformation processes inferred from the OH-stretch and CH-stretch spectra of the plant-derived biochars.

Surface charge characteristics of the different biochars studied were also consistent with observed spectral variations. For example, the highest CECs were observed in biochars formed in the 300- 400 ^{o}C range, consistent with DRIFTS data which showed that these biochars had the highest concentrations of free OH and carboxylic groups (the most probable sites for cation exchange).

Surface chemistry of the plant-derived biochars also varied across species. In addition to differences in CEC, differences in specific surface area, charge density and molar heats of K^{+}/Na^{+} exchange were also observed. Cation exchange capacity of the biochars followed the general trend: CG>> HM= PI. Molar heats of K^{+}/Na^{+} exchange were -7.92, -3.19 and -3.61 kJ mol^{-1} for CG, HM and PI, respectively, suggesting that K^{+}/Na^{+} exchange was more favorable on the grass rather than wood biochars. Flow adsorption micro-calorimetry data also suggested that Cd^{2+} sorption on biochars formed

at temperatures <350 ^{o}C occurred via an ion exchange/surface complexation mechanism, but for biochars formed at higher temperatures Cd^{2+} was adsorbed via a ion exchange/surface complexation/diffusion controlled mechanism.

The findings of this research have significant implications for understanding the role of plant-derived biochars in the geochemical cycling of nutrients and contaminants. For example, one would expect the cord grass biochars used in this study, with their higher CEC and charge density to be a more effective sorbents of heavy metals than the wood biochars. Conversely, the HM and PI biochars with their higher surface areas, lower CEC and charge density are likely to be more effective sorbents of hydrophobic/ nonpolar contaminants.

CHAPTER V

SUMMARY

Calorimetric techniques were used to study organic- inorganic reactions in two different systems. The primary objectives were to elucidate potential mechanism(s) by which: (i) natural organic matter (NOM) influences strength development in lime-stabilized soils, and; (ii) plant-derived biochars reacts with cations in aqueous environments.

Natural organic matter influenced strength development in lime-stabilized soils through the direct inhibition of the formation of pozzolanic reaction products. The degree of inhibition was dependent mainly on the type of pozzolanic reaction product, and the amount and source of organic matter. The formation of the pozzolanic reaction product, calcium silicate hydrate II (CSH2) was less affected by NOM, than was the formation of CSH1. For a given pozzolanic product, the inhibition increased with NOM content. The effect of organic matter source followed the order fulvic acid> humic acid> lignite. Formation of CSH pozzolanic reaction products decreased by 50-100%, 20-80% and 20-40% in the presence of ≥2% fulvic acid, humic acid and lignite, respectively.

Cation interactions with plant-derived biochars were complex and depended both on the nature of the cation and biochar surface properties. Reactions involving the alkali cation, K^+; occurred via electrostatic ion exchange, on deprotonated functional groups located on the biochar surface and; were exothermic with molar heats of reaction (ΔH_{ads}) between -3 and -8 kJ mol^{-1}. In contrast, reactions involving the transition metal cation, Cd^{2+} were endothermic with ΔH_{ads} between +10 and +30 kJ mol^{-1}. Reaction

mechanism(s) for Cd^{2+} varied from ion exchange/surface complexation in biochars formed at <350 ^{o}C, to an ion exchange/surface complexation/diffusion-controlled mechanism in biochars formed at ≥350 ^{o}C. For a given cation, differences in sorption characteristics were attributable to temperature-dependent or plant species dependent variations in the properties of the biochars.

REFERENCES

[1] A.S. Goudie, The Human Impact on the Natural Environment: Past, Present, and Future. 6th ed., Blackwell Publishing, Malden, Massachusetts 2006.

[2] G. Friedl, A. Wuest, Aquat. Sci. 64 (2002) 55.

[3] L. Cuo, D.P. Lettenmaier, B.V. Mattheussen, P. Storck, M. Wiley, Hydrol. Process 22 (2008) 4205.

[4] P.R. Poulton, Can. J. Plant Sci. 76 (1996) 587.

[5] L.J. Almaleh, J.D. Grob, R.H. Gorny, Environ. Geol. 22 (1993) 308.

[6] C.C. Holt, R.J. Freer-Hewish, Proc. Inst. Civ. Eng.: Transport 129 (1998) 228.

[7] R. Baker, N. Bessaih, Proc. Inst. Civ. Eng.: Water Maritime and Energy 118 (1996) 199.

[8] J.E. Loehr, J.J. Bowders, J.W. Owen, L. Sommers, W. Liew, Transp. Res. Rec. 1714 (2000) 1.

[9] R.E. Sojka, D.L. Bjorneberg, J.A. Entry, R.D. Lentz, W.J. Orts, Adv. Agron. 92 (2007) 75.

[10] L.E. Katz, D.N. Humphrey, P.T. Jankauskas, F.A. DeMascio, Hazard. Waste Hazard. Mater. 13 (1996) 283.

[11] D.H. Moon, D.G. Grubb, T.L. Reilly, J. Hazard. Mater. 168 (2009) 944.

[12] M.A. Brainwood, S. Burgin, B. Maheshwari, Agric. Water Manage. 70 (2004) 151.

[13] R.E. Turner, N.N. Rabalais, Bioscience 41 (1991) 140.

[14] S.M. Cha, S.J. Ki, K.H. Cho, H. Choi, J.H. Kim, Water Sci. Technol. 59 (2009) 2437.

[15] M.J. Angilletta, E.A. Steel, K.K. Bartz, J.G. Kingsolver, M.D. Scheuerell, B.R. Beckman, L.G. Crozier, Evol. Appl. 1 (2008) 286.

[16] P.S. Levin, N. Tolimieri, Animal Conserv. 4 (2001) 291.

[17] E. Baran, C. Myschowoda, Aquat. Ecosyst. Health Manag. 12 (2009) 227.

[18] F.J. Stevenson, Humus Chemistry: Genesis, Composition, Reactions. 2nd ed., John Wiley & Sons, New York, 1994.

[19] K.H. Tan, Humic Matter in Soil and the Environment: Principles and Controversies. Marcel Dekker, New York, 2003.

[20] J.H. Seinfeld, J.F. Pankow, Annu. Rev. Phys. Chem. 54 (2003) 121.

[21] M.O. Andreae, P.J. Crutzen, Science 276 (1997) 1052.

[22] R.G. Derwent, M.E. Jenkin, C.E. Johnson, D.S. Stevenson, J. Atmos. Chem. 44 (2003) 57.

[23] K. Tsigaridis, M. Kanakidou, Atmos. Chem. Phys. 3 (2003) 1849.

[24] R.J. Griffin, D.R. Cocker, J.H. Seinfeld, D. Dabdub, Geophys. Res. Lett. 26 (1999) 2721.

[25] M. Kanakidou, K. Tsigaridis, F.J. Dentener, P.J. Crutzen, J. Geophys. Res.-Atmos. 105 (2000) 9243.

[26] B.R.T. Simoneit, Appl. Geochem. 17 (2002) 129.

[27] P.J. DeMott, M.D. Petters, A.J. Prenni, C.M. Carrico, S.M. Kreidenweis, J.L. Collett, H. Moosmuller, J. Geophys. Res.-Atmos. 114 (2009).

[28] K.A. Koehler, P.J. DeMott, S.M. Kreidenweis, O.B. Popovicheva, M.D. Petters, C.M. Carrico, E.D. Kireeva, T.D. Khokhlova, N.K. Shonija, Phys. Chem. Chem. Phys. 11 (2009) 7906.

[29] Y. Shinozuka, A.D. Clarke, P.F. DeCarlo, J.L. Jimenez, E.J. Dunlea, G.C. Roberts, J.M. Tomlinson, D.R. Collins, S.G. Howell, V.N. Kapustin, C.S. McNaughton, J. Zhou, Atmos. Chem. Phys. 9 (2009) 6727.

[30] M. Kanakidou, J.H. Seinfeld, S.N. Pandis, I. Barnes, F.J. Dentener, M.C. Facchini, R. Van Dingenen, B. Ervens, A. Nenes, C.J. Nielsen, E. Swietlicki, J.P. Putaud, Y. Balkanski, S. Fuzzi, J. Horth, G.K. Moortgat, R. Winterhalter, C.E.L. Myhre, K. Tsigaridis, E. Vignati, E.G. Stephanou, J. Wilson, Atmos. Chem. Phys. 5 (2005) 1053.

[31] V. Ramanathan, G. Carmichael, Nat. Geosci. 1 (2008) 221.

[32] N.H. Batjes, Eur. J. Soil Sci. 47 (1996) 151.

[33] W.H. Schlesinger, J.A. Andrews, Biogeochemistry 48 (2000) 7.

[34] C.M. Preston, M.W.I. Schmidt, Biogeosciences 3 (2006) 397.

[35] J. Lehmann, J. Skjemstad, S. Sohi, J. Carter, M. Barson, P. Falloon, K. Coleman, P. Woodbury, E. Krull, Nat. Geosci. 1 (2008) 832.

[36] W. Lee, P. Westerhoff, Water Res. 43 (2009) 2233.

[37] J.F. Lu, T. Zhang, J. Ma, Z.L. Chen, J. Hazard. Mater. 162 (2009) 140.

[38] R.L. Sinsabaugh, S. Findlay, in: S. Findlay, R.L. Sinsabaugh (Eds.), Aquatic Ecosystems: Interactivity of Dissolved Organic Matter; Academic Press, San Diego, CA, 2003, p 479.

[39] F.G. Bell, Eng. Geol. 42 (1996) 223.

[40] G. Rajasekaran, S. Narasimha Rao, Ocean Eng. 23 (1996) 325.

[41] C.D.F. Rogers, S. Glendinning, Transp. Res. Rec. 1721 (2000) 9.

[42] J.L. Eades, R.E. Grim, High. Res. Board, Bull. 262, Washington, DC (1960) 51.

[43] O.H. Ingles, in: F.G. Bell (Eds.), Ground Engineer's Reference Book; Butterworths, London, 1987, p 1.

[44] K.E. Clare, P.T. Sherwood, J. Appl. Chem. 4 (1954) 625.

[45] K.E. Clare, P.T. Sherwood, J. Appl. Chem. 6 (1956) 317.

[46] D.H. Chen, Z.M. Si, M. Saribudak, J. Perform. Constr. Facil. 23 (2009) 100.

[47] M.B. Hampton, T.B. Edil, in: A. Maher, D.S. Yang (Eds.), Soil Improvement for Big Digs: Geotechnical Special Publication; American Society of Civil Engineers, Reston, Virginia, 1998.

[48] K. Pousette, J. Mácsik, A. Jacobsson, R. Andersson, P. Lahtinen, in: Bredenberg, Holm, Broms (Eds.), Dry Mix Methods for Deep Soil Stabilization; Balkema, Rotterdam, 1999, p 85.

[49] L.-J. Kuo, B.E. Herbert, P. Louchouarn, Org. Geochem. 39 (2008) 1466.

[50] J.M. Novak, W.J. Busscher, D.L. Laird, M. Ahmedna, D.W. Watts, M.A.S. Niandou, Soil Sci. 174 (2009) 105.

[51] G. Cornelissen, M. Elmquist, I. Groth, O. Gustafsson, Environ. Sci. Technol. 38 (2004) 3574.

[52] G. Cornelissen, O. Gustafsson, Environ. Sci. Technol. 38 (2004) 148.

[53] G. Cornelissen, O. Gustafsson, Environ. Sci. Technol. 39 (2005) 764.

[54] G. Cornelissen, J. Haftka, J. Parsons, O. Gustafsson, Environ. Sci. Technol. 39 (2005) 3688.

[55] G. Cornelissen, Z. Kukulska, S. Kalaitzidis, K. Christanis, O. Gustafsson, Environ. Sci. Technol. 38 (2004) 3632.

[56] T.A.J. Kuhlbusch, P.J. Crutzen, Global Biogeochem. Cycles 9 (1995) 491.

[57] G. Cornelissen, O. Gustafsson, T.D. Bucheli, M.T.O. Jonker, A.A. Koelmans, P.C.M. Van Noort, Environ. Sci. Technol. 39 (2005) 6881.

[58] T.A.J. Kuhlbusch, Science 280 (1998) 1903.

[59] S. Kwon, J.J. Pignatello, Environ. Sci. Technol. 39 (2005) 7932.

[60] C.A. Masiello, E.R.M. Druffel, Science 280 (1998) 1911.

[61] O. Gustafsson, P.M. Gschwend, Geochim. Cosmochim. Acta 62 (1998) 465.

[62] M.W.I. Schmidt, A.G. Noack, Global Biogeochem. Cycles 14 (2000) 777.

[63] J.O. Skjemstad, D.C. Reicosky, A.R. Wilts, J.A. McGowan, Soil Sci. Soc. Am. J. 66 (2002) 1249.

[64] B. Liang, J. Lehmann, D. Solomon, S. Sohi, J.E. Thies, J.O. Skjemstad, F.J. Luizao, M.H. Engelhard, E.G. Neves, S. Wirick, Geochim. Cosmochim. Acta 72 (2008) 6069.

[65] B.T. Nguyen, J. Lehmann, J. Kinyangi, R. Smernik, S.J. Riha, M.H. Engelhard, Biogeochemistry 89 (2008) 295.

[66] E.D. Goldberg, Black Carbon in the Environment: Properties and Distribution. John Wiley, New York, 1985.

[67] H.P.H. Arp, G.D. Breedveld, G. Cornelissen, Environ. Sci.Technol. 43 (2009) 5576.

[68] R.C. Brandli, T. Hartnik, T. Henriksen, G. Cornelissen, Chemosphere 73 (2008) 1805.

[69] G. Cornelissen, H.P.H. Arp, A. Pettersen, A. Hauge, G.D. Breedveld, Chemosphere 72 (2008) 1581.

[70] M.A. Rondon, J. Lehmann, J. Ramirez, M. Hurtado, Biol. Fertil. Soils 43 (2007) 699.

[71] C. Steiner, B. Glaser, W.G. Teixeira, J. Lehmann, W.E.H. Blum, W. Zech, J. Plant Nutr. Soil Sci. 171 (2008) 893.

[72] D.D. Warnock, J. Lehmann, T.W. Kuyper, M.C. Rillig, Plant and Soil 300 (2007) 9.

[73] K.Y. Chan, L. Van Zwieten, I. Meszaros, A. Downie, S. Joseph, Aust. J. Soil Res. 46 (2008) 437.

[74] J.W. Gaskin, C. Steiner, K. Harris, K.C. Das, B. Bibens, Trans. ASABE 51 (2008) 2061.

[75] N. Singh, R.S. Kookana, J. Environ. Sci. Health, Part B 44 (2009) 214.

[76] J.I. Hedges, G. Eglinton, P.G. Hatcher, D.L. Kirchman, C. Arnosti, S. Derenne, R.P. Evershed, I. Kogel-Knabner, J.W. de Leeuw, R. Littke, W. Michaelis, J. Rullkotter, Org. Geochem. 31 (2000) 945.

[77] C.A. Masiello, Marine Chem. 92 (2004) 201.

[78] H. Abdullah, H.W. Wu, Energ Fuel 23 (2009) 4174.

[79] X.D. Cao, L.N. Ma, B. Gao, W. Harris, Environ. Sci. Technol. 43 (2009) 3285.

[80] B.L. Chen, Z.M. Chen, Chemosphere 76 (2009) 127.

[81] B.L. Chen, D.D. Zhou, L.Z. Zhu, Environ. Sci. Technol. 42 (2008) 5137.

[82] J.L. Gaunt, J. Lehmann, Environ. Sci. Technol. 42 (2008) 4152.

[83] Z.G. Liu, F.S. Zhang, J. Hazard. Mater. 167 (2009) 933.

[84] K. Hammes, R.J. Smernik, J.O. Skjemstad, M.W.I. Schmidt, Appl. Geochem. 23 (2008) 2113.

[85] R.J. Whelan, The Ecology of Fire, Cambridge University Press, Cambridge; New York, 1995.

[86] H.A. Wright, A.W. Bailey, Fire Ecology: United States and Southern Canada, Wiley, New York, 1982.

[87] H. Knicker, Biogeochemistry 85 (2007) 91.

[88] H. Knicker, A. Hilscher, F.J. González-Vila, G. Almendros, Org. Geochem. 39 (2008) 935.

[89] H. Knicker, K.U. Totsche, G. Almendros, F.J. Gonzalez-Vila, Org. Geochem. 36 (2005) 1359.

[90] G. Almendros, H. Knicker, F.J. González-Vila, Org. Geochem. 34 (2003) 1559.

[91] J.A. Baldock, R.J. Smernik, Org. Geochem. 33 (2002) 1093.

[92] P.M. Trompowsky, V.d.M. Benites, B.E. Madari, A.S. Pimenta, W.C. Hockaday, P.G. Hatcher, Org. Geochem. 36 (2005) 1480.

[93] X. Wang, B. Xing, Environ. Sci. Technol. 41 (2007) 8342.

[94] Y. Chun, G.Y. Sheng, C.T. Chiou, B.S. Xing, Environ. Sci. Technol. 38 (2004) 4649.

[95] H.W. Sun, Z.L. Zhou, Chemosphere 71 (2008) 2113.

[96] D.Q. Zhu, S. Kwon, J.J. Pignatello, Environ. Sci. Technol. 39 (2005) 3990.

[97] K.J. Rockne, G.L. Taghon, D.S. Kosson, Chemosphere 41 (2000) 1125.

[98] J.A. Menendez, J. Phillips, B. Xia, L.R. Radovic, Langmuir 12 (1996) 4404.

[99] L.-J. Kuo, P. Louchouarn, B.E. Herbert, Org. Geochem. 39 (2008) 1522.

[100] O.S. Amuda, A.A. Giwa, I.A. Bello, Biochem. Eng. J. 36 (2007) 174.

[101] S.Y. Wang, M.H. Tsai, S.F. Lo, M.J. Tsai, Bioresour. Technol. 99 (2008) 7027.

[102] J.Y. Chen, D.Q. Zhu, C. Sun, Environ. Sci. Technol. 41 (2007) 2536.

[103] M. Sander, J.J. Pignatello, Environ. Sci. Technol. 39 (2005) 1606.

[104] D.Q. Zhu, J.J. Pignatello, Environ. Sci. Tech. 39 (2005) 2033.

[105] T.H. Nguyen, H.H. Cho, D.L. Poster, W.P. Ball, Environ. Sci. Technol. 41 (2007) 1212.

[106] Y. Kaneko, M. Abe, K. Ogino, Colloids Surf. 37 (1989) 211.

[107] L. Li, P.A. Quinlivan, D.R.U. Knappe, Carbon 40 (2002) 2085.

[108] B.A. Schumacher, Methods for Determination of Total Organic Carbon (TOC) in Soils and Sediments, United States Environmental Protection Agency, Las Vegas, Nevada, 2002.

[109] S.R. Abella, B.W. Zimmer, Soil Sci. Soc. Am. J. 71 (2007) 545.

[110] R.N. Fernandez, D.G. Schulze, D.L. Coffin, G.E. Vanscoyoc, Soil Sci. Soc. Am. J. 52 (1988) 1023.

[111] M.E. Konen, P.M. Jacobs, C.L. Burras, B.J. Talaga, J.A. Mason, Soil Sci. Soc. Am. J. 66 (2002) 1878.

[112] F. Chen, D.E. Kissel, L.T. West, D. Rickman, J.C. Luvall, W. Adkins, J. Soil Water Conserv. 60 (2005) 51.

[113] R.A. Bowman, W.D. Guenzi, D.J. Savory, Soil Sci. Soc. Am. J. 55 (1991) 563.

[114] G.W. McCarty, J.B. Reeves, V.B. Reeves, R.F. Follett, J.M. Kimble, Soil Sci. Soc. Am. J. 66 (2002) 640.

[115] F.A. Ibarra, J.R. Cox, M.H. Martin, T.A. Crowl, D.F. Post, R.W. Miller, G.A. Rasmussen, Soil Sci. Soc. Am. J. 59 (1995) 1120.

[116] M.E. Konen, C.L. Burras, J.A. Sandor, Soil Sci. Soc. Am. J. 67 (2003) 1823.

[117] D.G. Schulze, J.L. Nagel, G.E. Van Scoyoc, T.L. Henderson, M.F. Baumgardner, D.E. Stott, in: J.M. Bingham, E.J. Ciolkosz (Eds.), 1993, p 71.

[118] S.A. Wills, C.L. Burras, J.A. Sandor, Soil Sci. Soc. Am. J. 71 (2007) 380.

[119] E.E. Schulte, B.G. Hopkins, in: F.R. Magdoff (Eds.), Soil Organic Matter: Analysis and Interpretation; Soil Science Society of America, Madison, Wisconsin, 1996, p 21.

[120] A. Walkley, Soil Sci. 63 (1947) 251.

[121] R.A. Bowman, Commun. Soil Sci. Plant Anal. 29 (1998) 501.

[122] J.S. Kern, Soil Sci. Soc. Am. J. 58 (1994) 439.

[123] V.J. Kilmer, L.T. Alexander, Soil Sci. 68 (1949) 15.

[124] A. Dreimanis, J. Sediment. Res. 32 (1962) 520.

[125] U.S. Salinity Laboratory Staff, Diagnosis and Improvement of Saline and Alkali Soils, Rev. ed. Agric. Handbk. 60, U.S. Gov. Print. Office, Washington, DC, 1969.

[126] Soil Survey Staff, Soil Survey Laboratory Methods Manual, Soil Surv. Invest. Rep. 42, U.S. Gov. Print. Office, Washington, DC, 1996.

[127] D.W. Nelson, L.E. Sommers, in: A.L. Page, R.H. Miller, D.R. Keeney (Eds.), Methods of Soil Analysis, Part 2 - Chemical and Microbiological Properties, 2nd ed.; Agronomy Society of America - Soil Science Society of America, Madison, Wisconsin., 1982, p 539.

[128] K. Islam, B. Singh, A. McBratney, Aust. J. Soil Res. 41 (2003) 1101.

[129] R.L. Malcolm, P. Maccarthy, Environ. Sci. Technol. 20 (1986) 904.

[130] M.M.D. Sierra, M. Giovanela, E. Parlanti, E.J. Soriano-Sierra, Chemosphere 58 (2005) 715.

[131] J.M. Novak, G.L. Mills, P.M. Bertsch, J. Environ. Qual. 21 (1992) 144.

[132] S.J. Traina, J. Novak, N.E. Smeck, J. Environ. Qual. 19 (1990) 151.

[133] A. Majzik, E. Tombacz, Org. Geochem. 38 (2007) 1330.

[134] L.N. Alexandrova, Sov. Soil Sci. (Engl. Transl.) 2 (1960) 190.

[135] S. Diamond, J.L. White, W.L. Dolch, Clays Clay Miner. 12 (1963) 359.

[136] H. Chen, Q. Wang, Bull. Eng. Geol. Environ. 65 (2006) 445.

[137] H. Tremblay, J. Duchesne, J. Locat, S. Leroueil, Can. Geotech. J. 39 (2002) 535.

[138] G.R. Glenn, High. Res. Rec. (1970) 122.

[139] A. Bakolas, E. Aggelakopoulou, A. Moropoulou, J. Therm. Anal. Calorim. 92 (2008) 345.

[140] P. Ubbriaco, F. Tasselli, J. Therm. Anal. Calorim. 52 (1998) 1047.

[141] A.D. Karathanasis, in: A.L. Ulery, R.L. Drees (Eds.), Methods of Soil Analysis, Part 5: Mineralogical Methods; Soil Science Society of America, Madison, Wisconsin, 2008, p 117.

[142] J.L. Eades, F.P. Nichols, R.E. Grim, High. Res. Board, Bull. 335, Washington, DC (1962) 31.

[143] B. Caglar, B. Afsin, A. Tabak, E. Eren, Chem. Eng. J. 149 (2009) 242.

[144] A. Bakolas, E. Aggelakopoulou, A. Moropoulou, S. Anagnostopoulou, J. Therm. Anal. Calorim. 84 (2006) 157.

[145] S. Hebib, E.R. Farrell, Can. Geotech. J. 40 (2003) 107.

[146] B.B.K. Huat, S. Maail, T.A. Mohammed, Am. J. Appl. Sci. 2 (2005) 1113.

[147] M.S. Forbes, R.J. Raison, J.O. Skjemstad, Sci. Total Environ. 370 (2006) 190.

[148] F. Karaosmanoglu, A. Isigigur-Ergundenler, A. Sever, Energ Fuel 14 (2000) 336.

[149] N. Mahinpey, P. Murugan, T. Mani, R. Raina, Energ Fuel 23 (2009) 2736.

[150] D. Özçimen, F. Karaosmanoglu, Renewable Energy 29 (2004) 779.

[151] M.E. Sánchez, E. Lindao, D. Margaleff, O. Martínez, A. Morán, J. Anal. Appl. Pyrolysis 85 (2009) 142.

[152] S. Karagoz, T. Bhaskar, A. Muto, Y. Sakata, Fuel 84 (2005) 875.

[153] L. Haumaier, W. Zech, Org. Geochem. 23 (1995) 191.

[154] C.I. Czimczik, C.A. Masiello, Global Biogeochem. Cycles 21 (2007) 8.

[155] M.W.I. Schmidt, Nature 427 (2004) 305.

[156] K. Hammes, M.S. Torn, A.G. Lapenas, M.W.I. Schmidt, Biogeosciences 5 (2008) 1339.

[157] M.W.I. Schmidt, J.O. Skjemstad, E. Gehrt, I. Kogel-Knabner, Eur. J. Soil Sci. 50 (1999) 351.

[158] J.O. Skjemstad, P. Clarke, J.A. Taylor, J.M. Oades, S.G. McClure, Aust. J. Soil Res. 34 (1996) 251.

[159] A.V. McBeath, R.J. Smernik, Org. Geochem. 40 (2009) 1161.

[160] G. James, D.A. Sabatini, C.T. Chiou, D. Rutherford, A.C. Scott, H.K. Karapanagioti, Water Res. 39 (2005) 549.

[161] C.K. Ahn, D. Park, S.H. Woo, J.M. Park, J. Hazard. Mater. 164 (2009) 1130.

[162] P.A. Brown, S.A. Gill, S.J. Allen, Water Res. 34 (2000) 3907.

[163] C. Gabaldon, P. Marzal, J. Ferrer, A. Seco, Water Res. 30 (1996) 3050.

[164] A. Kongsuwan, P. Patnukao, P. Pavasant, J. Ind. Eng. Chem. 15 (2009) 465.

[165] Y.L. Lai, G. Annadurai, F.C. Huang, J.F. Lee, J. Chem.Technol. Biotechnol. 83 (2008) 788.

[166] A.G. Liu, R.D. Gonzalez, J. Colloid Interface Sci. 218 (1999) 225.

[167] A.G. Liu, R.D. Gonzalez, Langmuir 16 (2000) 3902.

[168] Y. Liu, Y. Li, X.P. Yan, Adv. Funct. Mater. 18 (2008) 1536.

[169] S.I. Lyubchik, A.I. Lyubchik, O.L. Galushko, L.P. Tikhonova, J. Vital, I.M. Fonseca, S.B. Lyubchik, Colloids Surf., A 242 (2004) 151.

[170] J.P. Ruparelia, S.P. Duttagupta, A.K. Chatterjee, S. Mukherji, Desalination 232 (2008) 145.

[171] K. Santhy, P. Selvapathy, Sep. Sci. Technol. 39 (2004) 3331.

[172] A. Schierz, H. Zanker, Environ. Pollut. 157 (2009) 1088.

[173] K.M. Spark, J.D. Wells, B.B. Johnson, Aust. J. Soil Res. 35 (1997) 89.

[174] A.M. Youssef, T. El-Nabarawy, S.E. Samra, Colloids Surf., A 235 (2004) 153.

[175] H.B. Bradl, J. Colloid Interface Sci. 277 (2004) 1.

[176] X.K. Wang, C.L. Chen, W.P. Hu, A.P. Ding, D. Xu, X. Zhou, Environ. Sci. Technol. 39 (2005) 2856.

[177] P. Warwick, E. Inam, N. Evans, Environ. Chem. 2 (2005) 119.

[178] P. Zhou, H. Yan, B.H. Gu, Chemosphere 58 (2005) 1327.

[179] H.P. Boehm, Carbon 40 (2002) 145.

[180] C.L. Mangun, K.R. Benak, J. Economy, K.L. Foster, Carbon 39 (2001) 1809.

[181] B.T. Nguyen, J. Lehmann, Org. Geochem. 40 (2009) 846.

[182] J. Zhang, H. Zou, Q. Qing, Y. Yang, Q. Li, Z. Liu, X. Guo, Z. Du, J. Phys. Chem. B 107 (2003) 3712.

[183] U. Zielke, K.J. Hüttinger, W.P. Hoffman, Carbon 34 (1996) 983.

[184] W.J. Bond, I.R. Phillips, Soil Sci. Soc. Am. J. 54 (1990) 722.

[185] D.M. Ditoro, J.D. Mahony, P.R. Kirchgraber, A.L. Obyrne, L.R. Pasquale, D.C. Piccirilli, Environ. Sci. Technol. 20 (1986) 55.

[186] S.C. Hodges, G.C. Johnson, Soil Sci. Soc. Am. J. 51 (1987) 323.

[187] D. Schweich, M. Sardin, J. Hydrology 50 (1981) 1.

[188] D. Schweich, M. Sardin, J.P. Gaudet, Soil Sci. Soc. Am. J. 47 (1983) 32.

[189] D.L. Sparks, Adv. Agron. 38 (1985) 231.

[190] A.J. Groszek, Thermochim. Acta 312 (1998) 133.

[191] W. Rudzinski, R. Charmas, W. Piasecki, A.J. Groszek, F. Thomas, F. Villieras, B. Prelot, J.M. Cases, Langmuir 15 (1999) 5921.

[192] O.R. Harvey, R.D. Rhue, J. Colloid Interface Sci. 322 (2008) 384.

[193] N.J. Kabengi, S.H. Daroub, R.D. Rhue, J. Colloid Interface Sci. 297 (2006) 86.

[194] N.J. Kabengi, R.D. Rhue, S.H. Daroub, Soil Sci. 171 (2006) 13.

[195] R.D. Rhue, C. Appel, N. Kabengi, Soil Sci. 167 (2002) 782.

[196] G. Steinberg, Chemtech 11 (1981) 730.

[197] A. Savitzky, M.J.E. Golay, Anal. Chem. 36 (2002) 1627.

[198] D.L. Eskew, I.P. Ting, Am. J. Bot. 65 (1978) 850.

[199] P. Felker, P.R. Clark, Plant and Soil 57 (1980) 177.

[200] G. Shearer, D.H. Kohl, R.A. Virginia, B.A. Bryan, J.L. Skeeters, E.T. Nilsen, M.R. Sharifi, P.W. Rundel, Oecologia 56 (1983) 365.

[201] K. Hammes, R.J. Smernik, J.O. Skjemstad, A. Herzog, U.F. Vogt, M.W.I. Schmidt, Org. Geochem. 37 (2006) 1629.

[202] F. Braadbaart, J.J. Boon, H. Veld, P. David, P.F. van Bergen, J. Archaeol. Sci. 31 (2004) 821.

[203] J. Scheirs, G. Camino, W. Tumiatti, Eur. Poly. J. 37 (2001) 933.

[204] H. Yang, R. Yan, H. Chen, D.H. Lee, C. Zheng, Fuel 86 (2007) 1781.

[205] A. Watanabe, S. Morita, Y. Ozaki, Biomacromolecules 7 (2006) 3164.

[206] Y. Marechal, H. Chanzy, J. Mol. Struct. 523 (2000) 183.

[207] M. Wada, J. Polym. Sci., Part B-Polym. Phys. 40 (2002) 1095.

[208] M. Wada, T. Kondo, T. Okano, Polym. J. 35 (2003) 155.

[209] B. Stuart, Infrared Spectroscopy: Fundamentals and Applications. John Wiley & Sons, Chichester, Sussex, 2004.

[210] F. Shafizadeh, A.G.W. Bradbury, J. Appl. Polym. Sci. 23 (1979) 1431.

[211] P. Hanzlik, J. Jehlicka, Z. Weishauptova, O. Sebek, Plant Soil Environ. 50 (2004) 257.

[212] J.S. Johnson Jr, C.G. Westmoreland, F.H. Sweeton, K.A. Kraus, E.W. Hagaman, W.P. Eatherly, H.R. Child, J. Chromatogr. A 354 (1986) 231.

[213] G.G.S. Holmgren, M.W. Meyer, R.L. Chaney, R.B. Daniels, J. Environ. Qual. 22 (1993) 335.

[214] B. Liang, J. Lehmann, D. Solomon, J. Kinyangi, J. Grossman, B. O'Neill, J.O. Skjemstad, J. Thies, F.J. Luizao, J. Petersen, E.G. Neves, Soil Sci. Soc. Am. J. 70 (2006) 1719.

[215] L.M. McDonald, V.P. Evangelou, M.A. Chappell, D. Hillel, in: D. Hillel (Eds.), Encyclopedia of Soils in the Environment; Elsevier, Oxford, 2005, p 180.

[216] R. Spaccini, J.S.C. Mbagwu, P. Conte, A. Piccolo, Geoderma 132 (2006) 9.

[217] R.A. Brown, A.K. Kercher, T.H. Nguyen, D.C. Nagle, W.P. Ball, Org. Geochem. 37 (2006) 321.

[218] M. Kaiser, R.H. Ellerbrock, H.H. Gerke, Soil Sci. Soc. Am. J. 72 (2008) 1278.

[219] C.A. Coles, R.N. Yong, Eng. Geol. 85 (2006) 26.

[220] R. Baccar, J. Bouzid, M. Feki, A. Montiel, J. Hazard. Mater. 162 (2009) 1522.

[221] M.I. Kandah, J.-L. Meunier, J. Hazard. Mater. 146 (2007) 283.

[222] A.M. Puziy, O.I. Poddubnaya, A. Martinez-Alonso, F. Suarez-Garcia, J.M.D. Tascon, Carbon 43 (2005) 2857.

[223] R.L. Frost, M.L. Weier, Thermochim. Acta 406 (2003) 221.

[224] J.I. Hedges, D.C. Mann, Geochim. Cosmochim. Acta 43 (1979) 1803.

[225] M.A. Goñi, J.I. Hedges, Geochim. Cosmochim. Acta 56 (1992) 4025.

[226] S. Opsahl, R. Benner, Geochim. Cosmochim. Acta 59 (1995) 4889.

[227] J.J. Boon, I. Pastorova, R.E. Botto, P.W. Arisz, Biomass Bioenergy 7 (1994) 25.

[228] J. Piskorz, D.S. Radlein, D.S. Scott, S. Czernik, J. Anal. Appl. Pyrolysis 16 (1989) 127.

[229] N. Shimada, H. Kawamoto, S. Saka, J. Anal. Appl. Pyrolysis 81 (2008) 80.

[230] M.J. Antal, Jr., G. Varhegyi, Ind. Eng. Chem. Res. 34 (1995) 703.

[231] F. Fraysse, O.S. Pokrovsky, J. Schott, J.-D. Meunier, Chem. Geol. 258 (2009) 197.

[232] J.D. Ritchie, E.M. Perdue, Geochim. Cosmochim. Acta 67 (2003) 85.

[233] J.L. Beltrán, N. Sanli, G. Fonrodona, D. Barrón, G. Özkan, J. Barbosa, Anal. Chim. Acta 484 (2003) 253.

[234] F.Z. Erdemgil, S. Sanli, N. Sanli, G. Özkan, J. Barbosa, J. Guiteras, J.L. Beltrán, Talanta 72 (2007) 489.

[235] O. Maman, F. Marseille, B. Guillet, J.-R. Disnar, P. Morin, J. Chromatogr. A 755 (1996) 89.

[236] L. Pulido-Novicio, T. Hata, Y. Kurimoto, S. Doi, S. Ishihara, Y. Imamura, J. Wood Sci. 47 (2001) 48.

[237] J. Pastor-Villegas, C. Valenzuela-Calahorro, A. Bernalte-Garcia, V. Gomez-Serrano, Carbon 31 (1993) 1061.

[238] N.C. Carpita, Annu. Rev. Plant Physiol. Plant Mol. Biol. 47 (1996) 445.

[239] H.Y. Lu, K.B. Liu, Estuarine, Coastal Shelf Sci. 58 (2003) 587.

[240] N. Kutaish, P. Aggarwal, D. Dollimore, Thermochim. Acta 297 (1997) 131.

[241] E.R. Nightingale, J. Phys. Chem. 63 (1959) 1381.

[242] T.D. Duong, K.L. Nguyen, M. Hoang, J. Colloid Interface Sci. 303 (2006) 69.

[243] S.A. Dastgheib, D.A. Rockstraw, Carbon 40 (2002) 1843.

[244] C.J. Gabelich, T.D. Tran, I.H. Suffet, Environ. Sci. Technol. 36 (2002) 3010.

[245] C.A. Rice-Evans, N.J. Miller, G. Paganga, Free Radic. Biol. Med. 20 (1996) 933.

[246] F. Natella, M. Nardini, M. Di Felice, C. Scaccini, J. Agric. Food Chem. 47 (1999) 1453.

[247] P. Marzal, A. Seco, C. Gabaldón, J. Ferrer, J. Chem. Technol. Biotechnol. 66 (1996) 279.

[248] R. Qadeer, N. Khalid, Sep. Sci.Technol. 40 (2005) 845.

[249] G.P. Rao, C. Lu, F. Su, Sep. Purif. Technol. 58 (2007) 224.

[250] Ö. Yavuz, Y. Altunkaynak, F. Güzel, Water Res. 37 (2003) 948.

[251] S. Lantenois, B. Prélot, J.-M. Douillard, K. Szczodrowski, M.-C. Charbonnel, Appl. Surf. Sci. 253 (2007) 5807.

[252] Y. Marcus, Biophys. Chem. 51 (1994) 111.

[253] Z. Gao, T.J. Bandosz, Z. Zhao, M. Han, J. Qiu, J. Hazard. Mater. 167 (2009) 357.

[254] Y.H. Li, S.G. Wang, Z.K. Luan, J. Ding, C.L. Xu, D.H. Wu, Carbon 41 (2003) 1057.

[255] X. Huang, N. Gao, Q. Zhang, J. Environ. Sci. 19 (2007) 1287.

[256] Y.F. Jia, K.M. Thomas, Langmuir 16 (1999) 1114.

APPENDIX 1

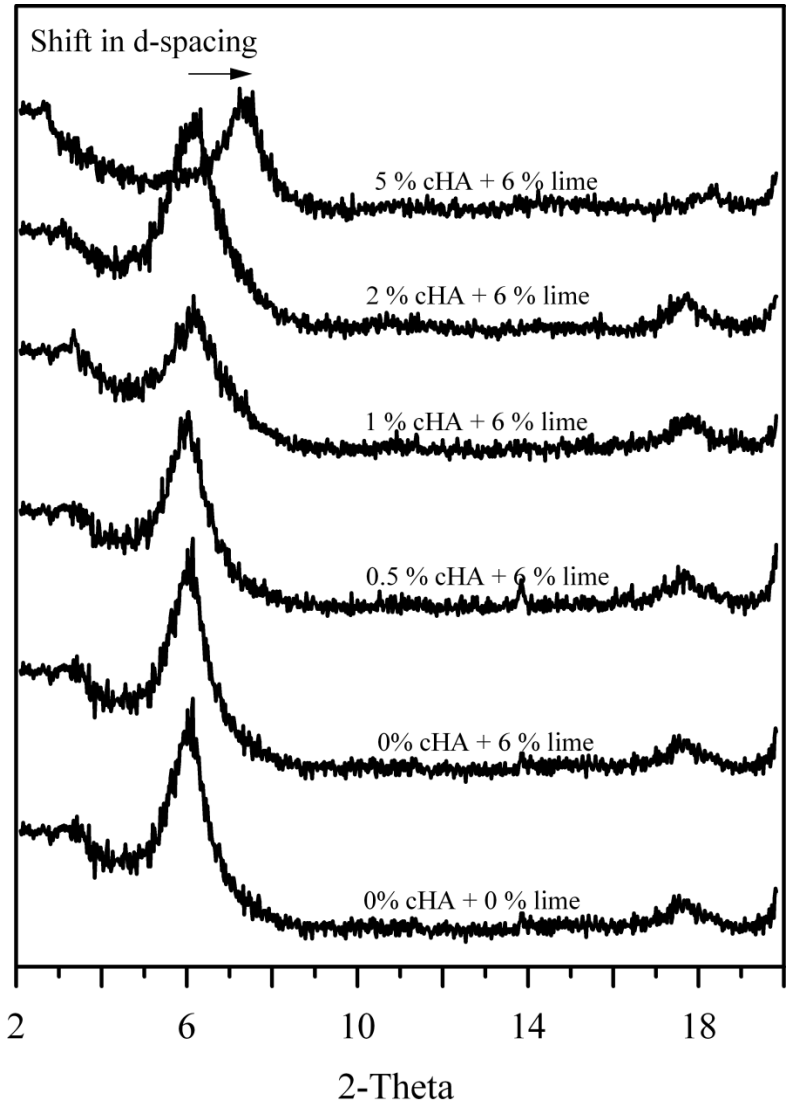

A1. Change in clay structure induced by high organic matter content.

APPENDIX 2

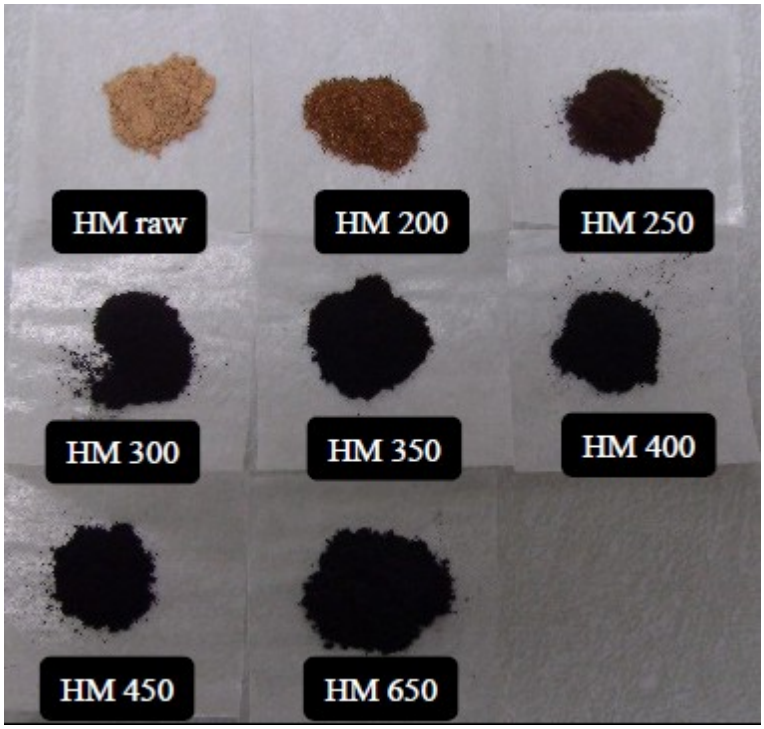

A2. Photograph of honey mesquite (HM) biochars produced at temperatures between 200 and 650 ^{o}C.

APPENDIX 3

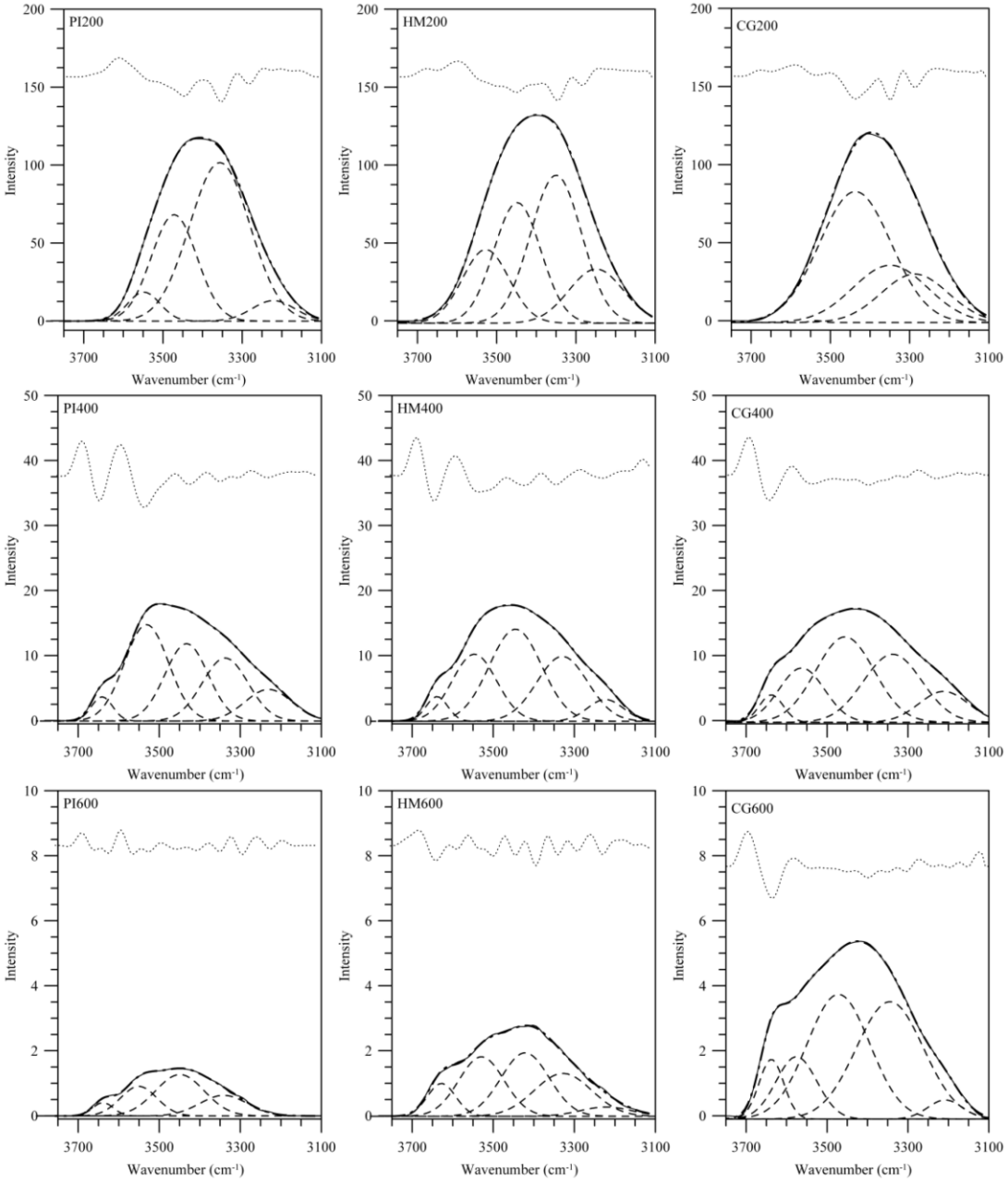

A3a. Deconvoluted peaks (broken lines) of OH-stretch infrared spectra (solid lines) for loblolly pine (PI), honey mequite (HM) and cord grass (CG) biochars formed at 200, 400, and 600 ^{o}C. Deconvolution based on 2nd derivative spectra (dotted lines) and assumption of Gaussian peak shape.

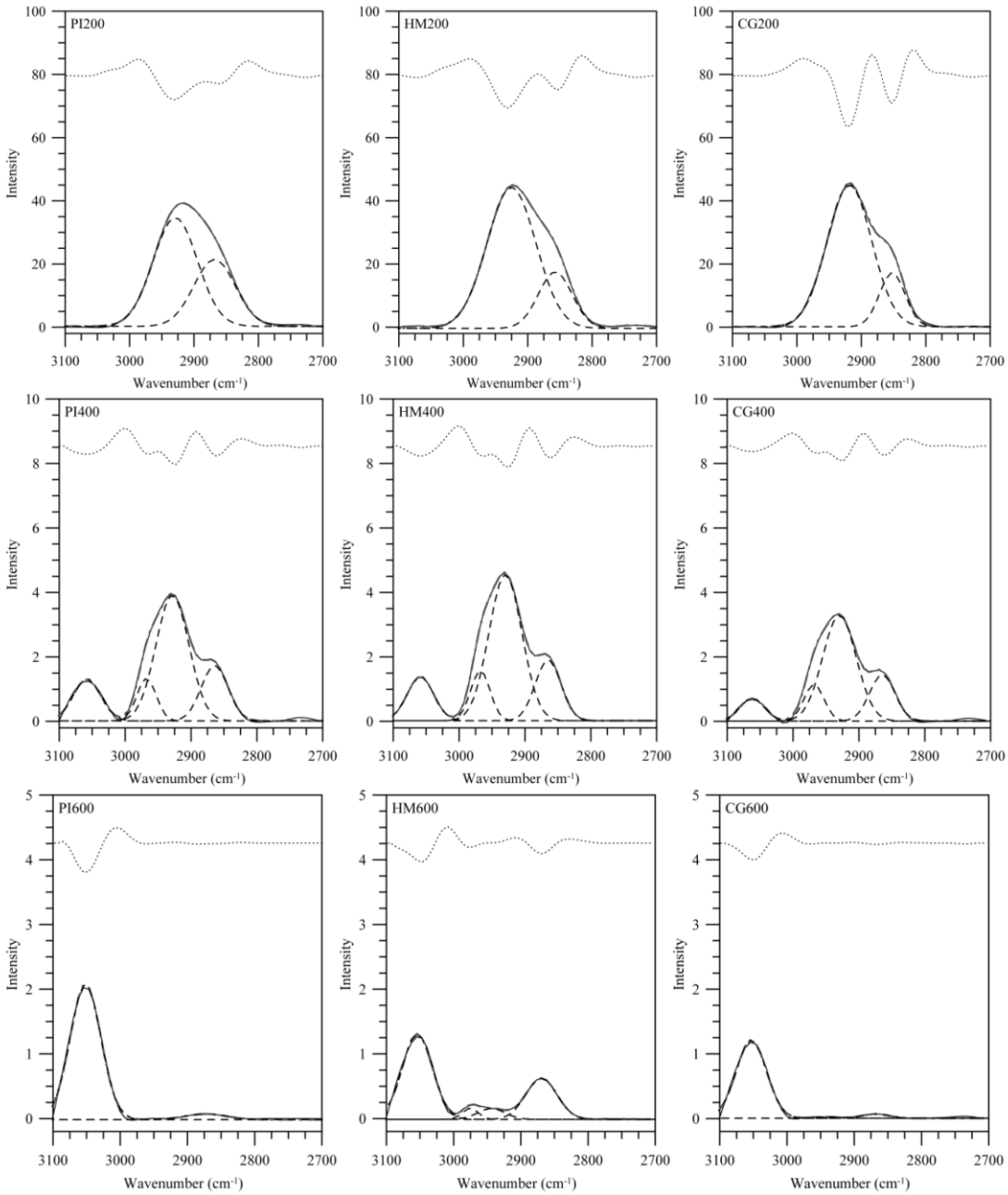

A3b. Deconvoluted peaks (broken lines) of CH-stretch infrared spectra (solid lines) for loblolly pine (PI), honey mequite (HM) and cord grass (CG) biochars formed at 200, 400, and 600 ^{o}C. Deconvolution based on 2nd derivative spectra (dotted lines) and assumption of Gaussian peak shape.

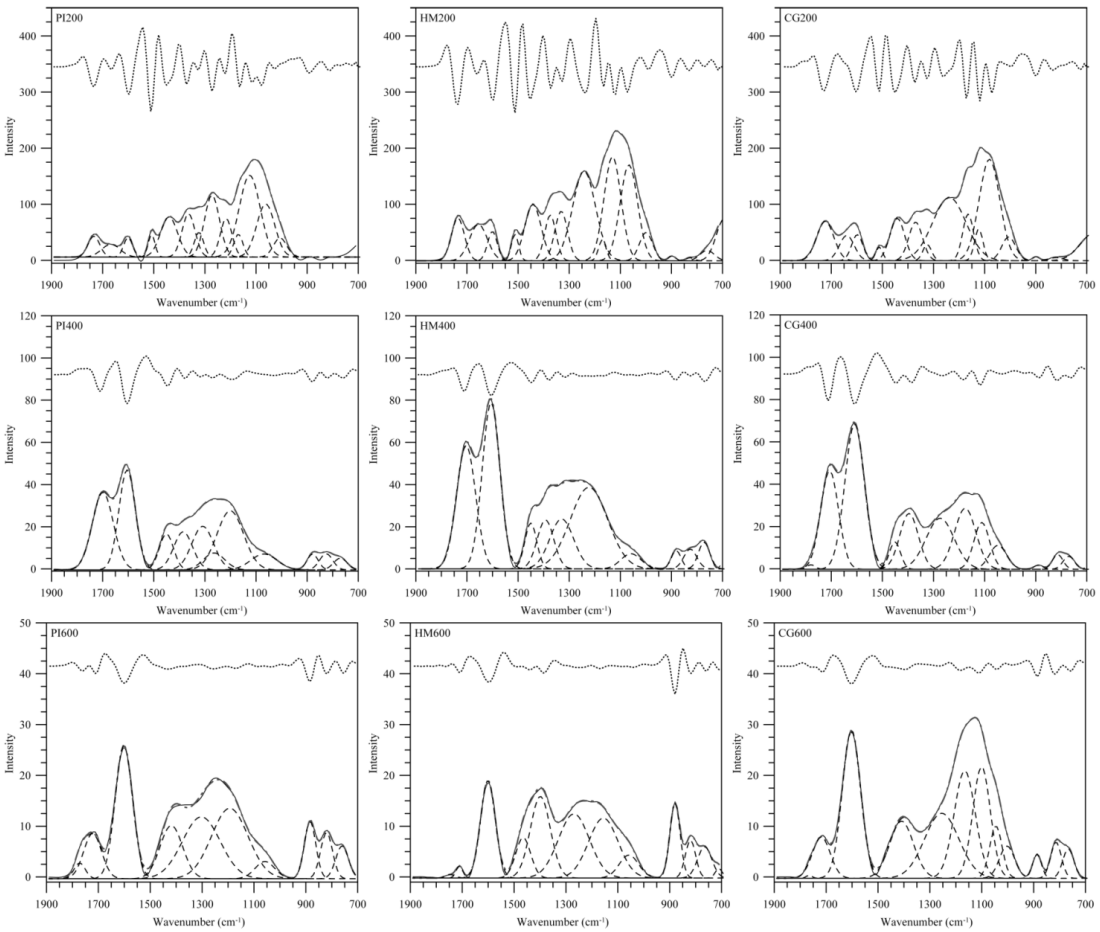

A3c. Deconvoluted peaks (broken lines) of the fingerprint infrared spectra (solid lines) for loblolly pine (PI), honey mequite (HM) and cord grass (CG) biochars formed at 200, 400, and 600 ^{o}C. Deconvolution based on 2nd derivative spectra (dotted lines) and assumption of Gaussian peak shape.

APPENDIX 4

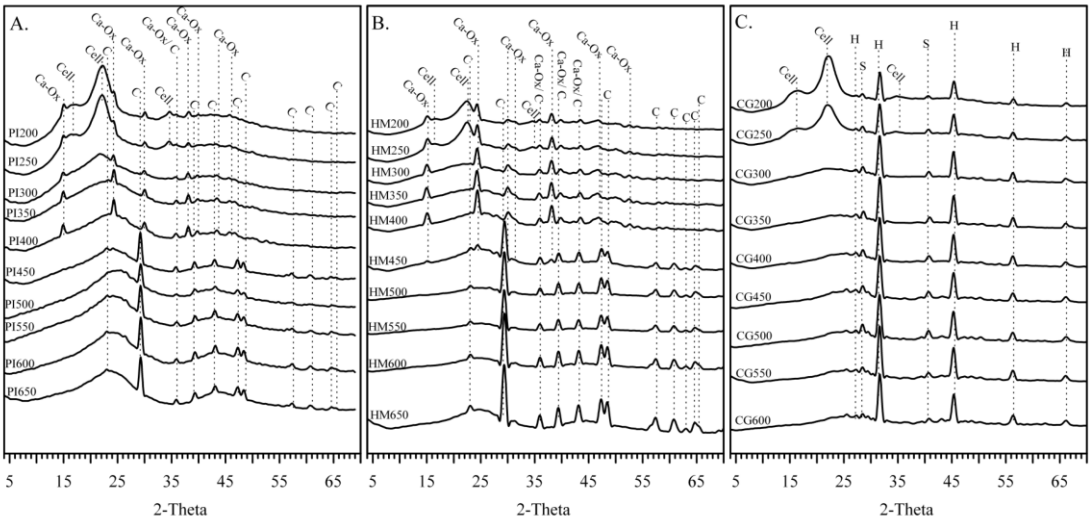

A4. X-ray diffraction analysis of plant-derived biochars. Ca-Ox- calcium oxalate; Cell- cellulose; C- calcite; H- halite/NaCl; S- sylvite/KCl.

APPENDIX 5

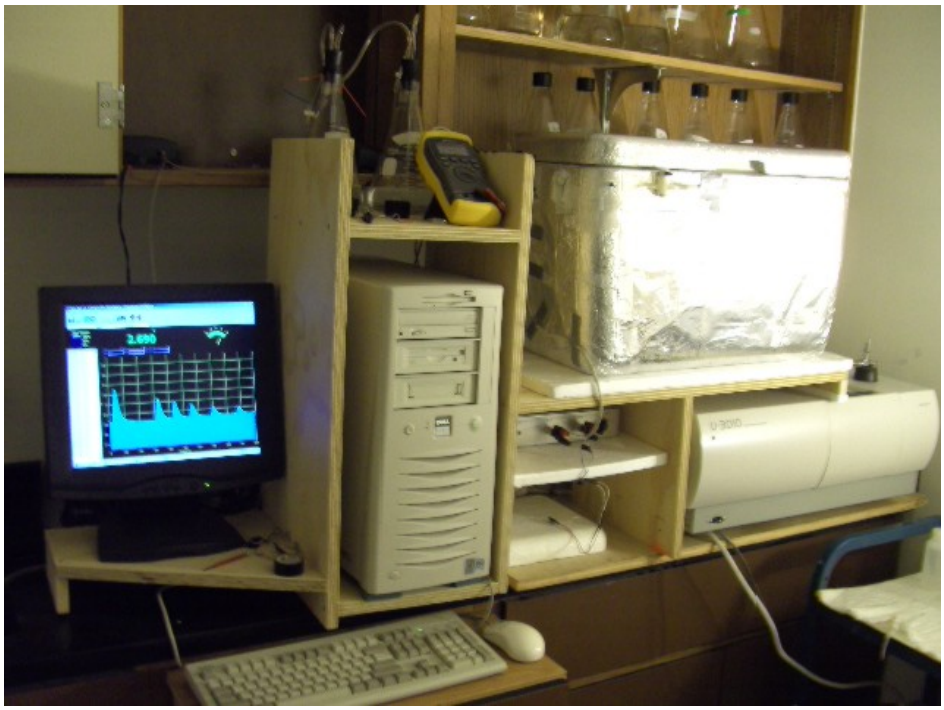

A5a. Photograph of the flow adsorption micro-calorimeter.

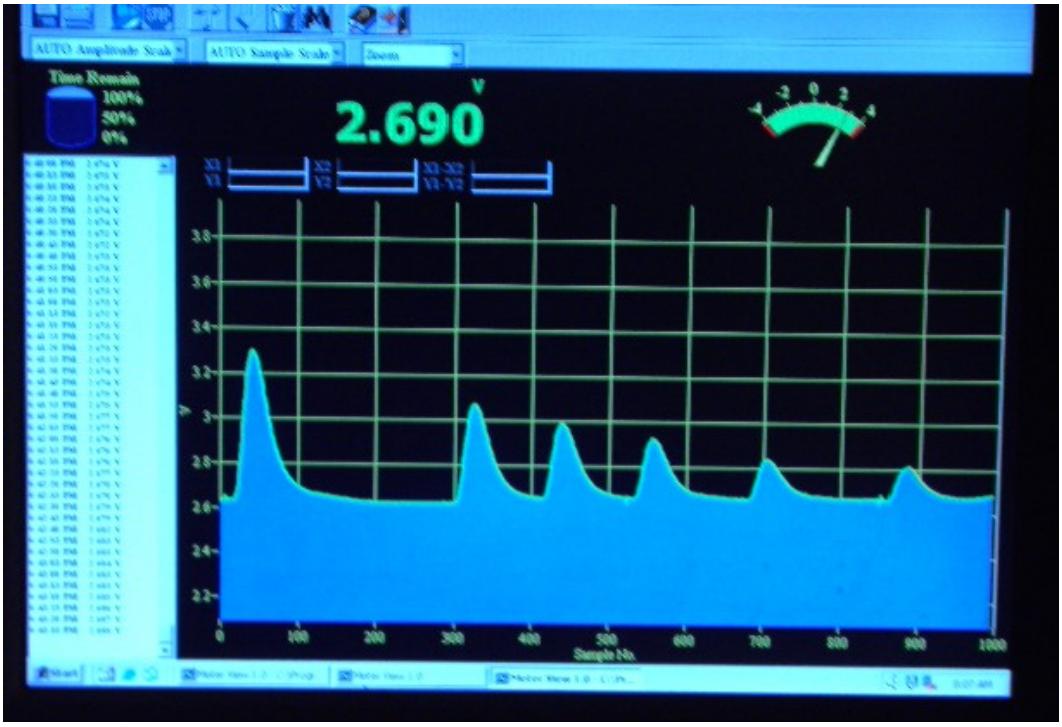

A5b. Screenshot of calorimetric response for calibration heat pulses of different amounts of energy input.

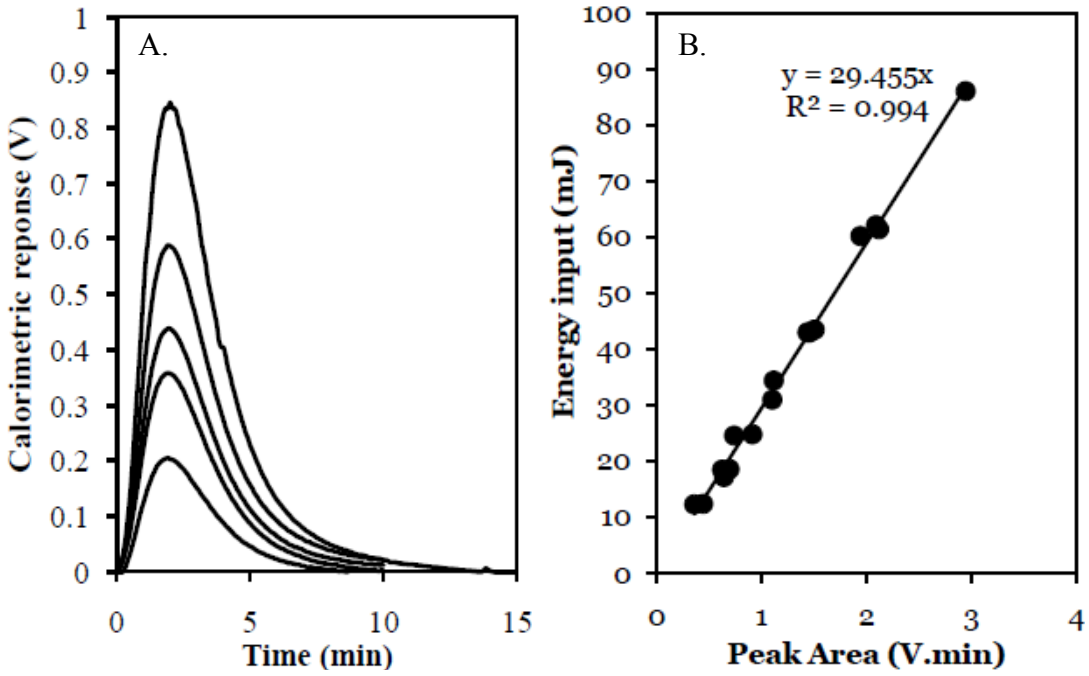

A5c. (A) Calorimetric response and (B) calibration curve for calibration heat pulses.

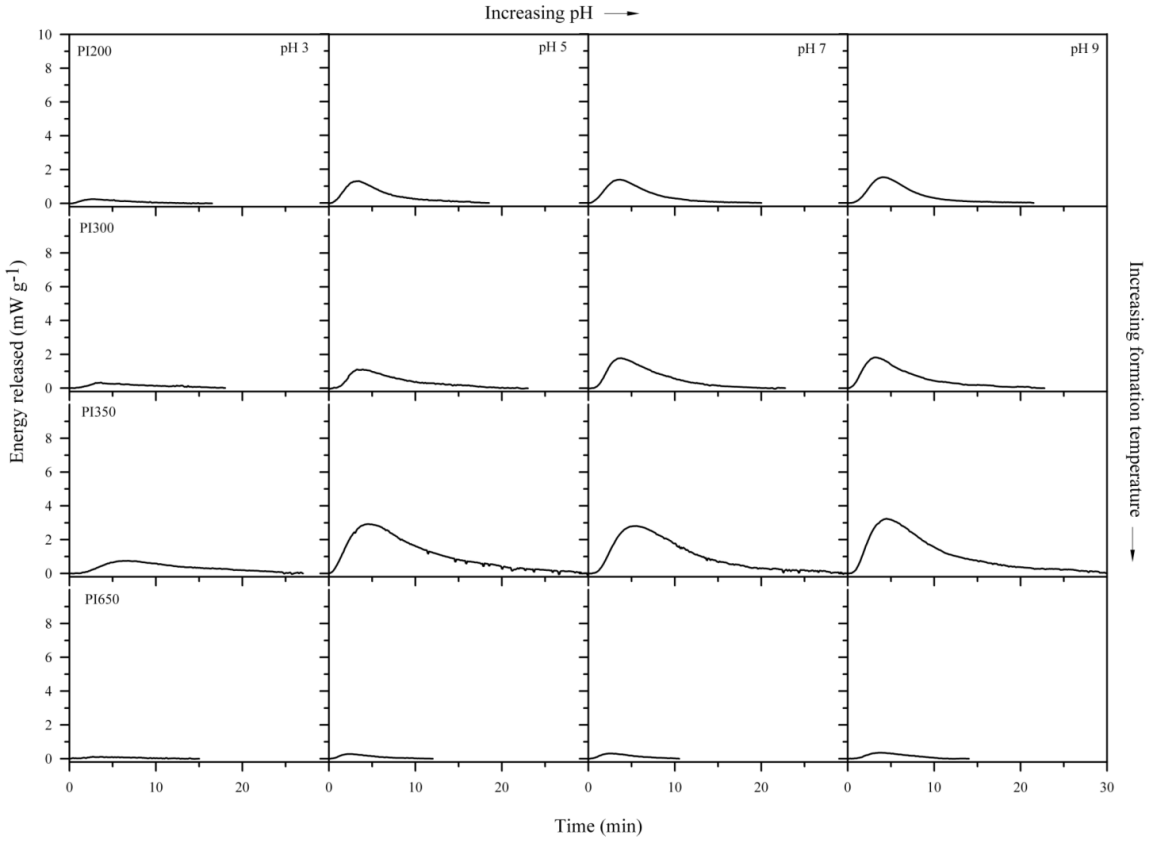

A5d. Heat signals for K^+/Na^+ ion exchange on loblolly pine biochars.

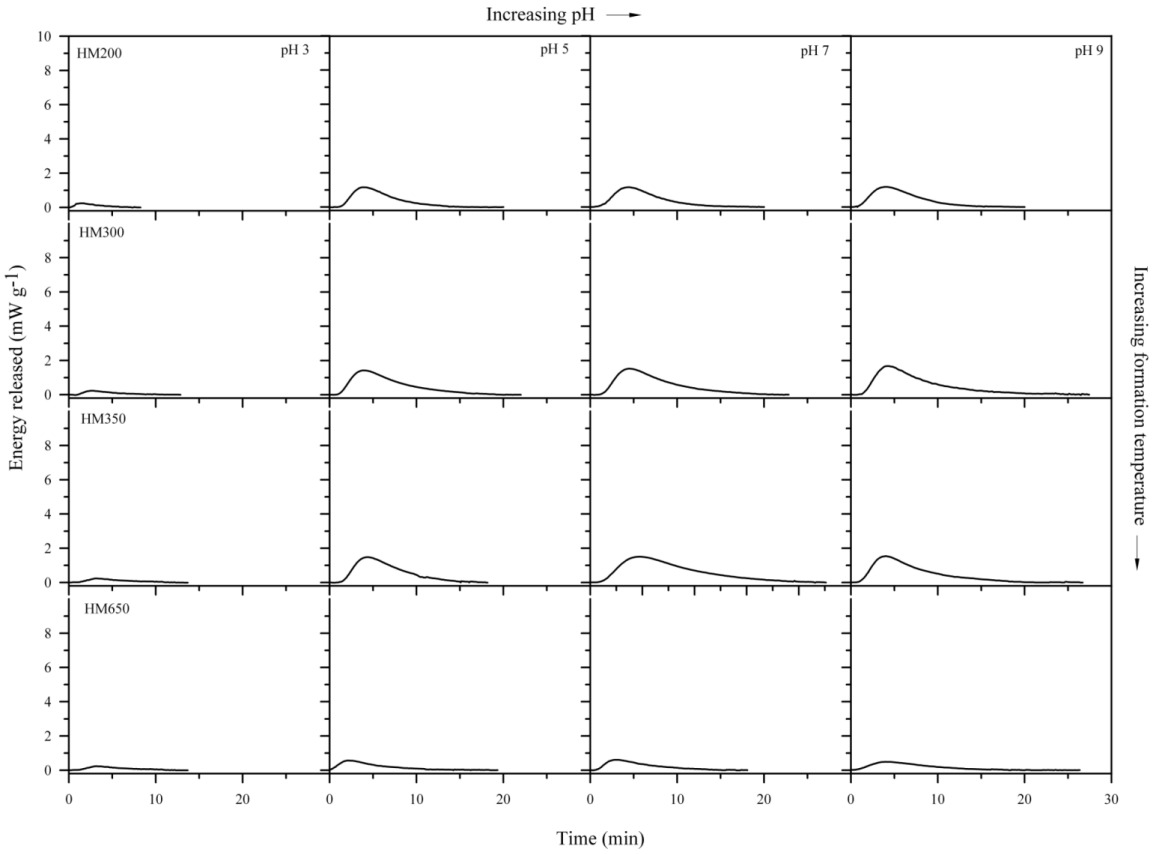

A5e. Heat signals for K^+/Na^+ ion exchange on honey mesquite biochars.

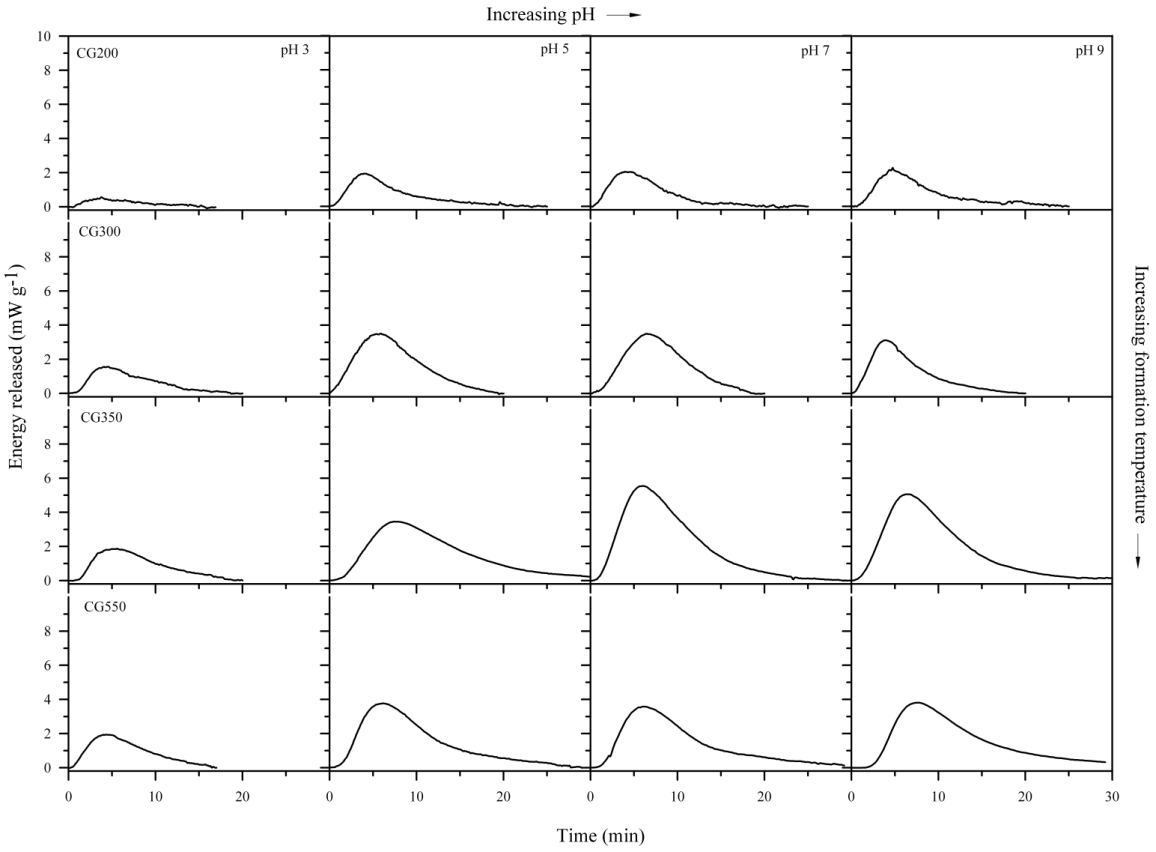

A5f. Heat signals for K^+/Na^+ ion exchange on cord grass biochars.

VITA

Name: Omar R. Harvey

Address: Water Management and Hydrological Science
3408 TAMU
College Station, TX 77843-3408
C/O Bruce Herbert

Email Address: orharvey@hotmail.com

Education: B.S., Agronomy, University of the West Indies, 2001
M.S., Soil and Water Sciences, University of Florida, 2004
Ph.D., Water Management and Hydrological Science, Texas A & M University, 2010